Development of a Beam Profile Monitor/Time of Flight setup for HISPEC/DESPEC for FAIR

Inaugural-Dissertation zur Erlangung des Doktorgrades der Mathematisch-Naturwissenschaftlichen Fakultät der Universität zu Köln

vorgelegt von
Michael Pfeiffer
aus Simmerath

Köln 2013

Berichterstatter:	Prof. Dr. J. Jolie Prof. Dr. P. Reiter
Tag der mündlichen Prüfung:	18.10.2013

Für Caro

Manchmal wollt ich fast verzagen und ich glaubt ich trüg es nie.
Und dann hab ich's doch getragen. Frag mich nur nicht, wie.

HEINRICH HEINE

Kurzzusammenfassung

Die *Helmholtz Gesellschaft für Schwerionenforschung GmbH* wird in den kommenden Jahren um die *Facility for Antiproton and Ion Research* erweitert. Im Rahmen dieser Erweiterung haben sich verschiedene internationale Kollaborationen entwickelt, um die dann zur Verfügung stehenden, neuen Beschleunigeranlagen effektiv zu nutzen. Die Kollaboration *Nuclear Structure, Astrophysics and Reactions*, kurz NUSTAR , beschäftigt sich mit der Nutzung hoch-energetischer, radioaktiver Ionenstrahlen für kernphysikalische Messungen.

Im Rahmen solcher Messungen ist es möglich, solche Ionen auf Energien von 5 bis 10 MeV/u abzubremsen, um Reaktionskanäle zu öffnen. Das Problem beim Abbremsen ist eine zusätzliche Streuung der Energie sowie der Flugrichtung, als auch eine weitere Fragmentierung des originären Ionenstrahls. Um dennoch eine Selektion der gewünschten Ionen zu ermöglichen, bedarf es eines zusätzlichen Detektors unmittelbar nach dem Abbremsen und vor der zu untersuchenden Probe. Im Rahmen der vorliegenden Arbeit wurde solch ein Detektorsystem entwickelt und getestet.

Eine Anforderung an ein solches System ist eine größtmögliche Transparenz, damit der zu untersuchende Ionenstrahl nicht mehr wechselwirkt als nötig oder gar gestoppt wird. Als Lösung wurde ein Design auf Basis einer Emissionsfolie gewählt. Dabei werden Elektronen aus einer dünnen Folie emittiert, sobald Ionen diese passieren. Diese sogenannten Sekundärelektronen werden durch einen elektrostatischen Aufbau beschleunigt und auf den eigentlichen Detektorkopf gelenkt und dort ortssensitiv registriert. So können die Ionen indirekt nachgewiesen werden. Mittels zwei solcher Einheiten kann die Flugbahn eines einzelnen Ions rekonstruiert werden und zusätzlich über die Flugzeit von andersartigen Ionen separiert werden.

Ein erster Prototyp wurde gebaut und dabei kontinuierlich weiterentwickelt. Mittels diverser Messungen mit radioaktiven Quellen wurde er auf seine Effizienz, Orts- und Zeitauflösung hin untersucht. Die so gewonnenen Erkenntnisse flossen in die Entwicklung eines zweiten Prototyps ein. Dabei wurde im Hinblick auf die zukünftige Verwendung das Augenmerk auf ein möglichst kompaktes, integriertes Design bei gleichzeitiger Verbesserung der Detektoreigenschaften gelegt.

Um den zweiten Prototyp zu untersuchen, wurde ein spezielles Strahlrohr zum Test von Detektoren und zur Simulation von abgebremsten Ionenstrahlen am Kölner FN Tandembeschleuniger errichtet. Dieser Messplatz steht der Kollaboration zur Verfügung und wurde schon erfolgreich benutzt.

Abstract

The *Helmholtz Gesellschaft für Schwerionenforschung GmbH* will be expanded by the *Facility for Antiproton and Ion Research* in upcoming years. Different, international collaborations have been formed in order to effectively use the accelerator facilities, which will become available. The collaboration *Nuclear Structure, Astrophysics and Reactions* deals with the usage of high energetic, radioactive ion beams for nuclear physics experiments.

During such experiments it is possible to slow down these ions to energies of 5 to 10 MeV/u to open certain reaction channels. A problem with the slowing down is the introduction of additional energy and spatial straggling as well as a further fragmentation of the original ion beam. To be able to nevertheless select the desired ion, an additional detector is needed directly after the slowing down and before the target. Within the framework of this thesis, such a detector system has been developed and tested.

One demand to such a system is a largest possible transparency, not to degrade or even stop the ion beam, which is to be examined. As a solution a design on the basis of an emissive foil has been chosen. Thereby electrons will be emitted out of a thin foil if passed by an ion. These so-called secondary electrons are then accelerated and confined by an electrostatic top-assembly towards the proper detector head where they are position sensitively registered. In this way the ions can be detected indirectly. Using two of such units, the flight path of a single ion can be reconstructed and discriminated against other kinds of ions, additionally.

A first prototype was built and continuously developed further. By measurements with radioactive sources its efficiency, spatial and timing resolution was tested. The insights gained therefrom were used to develop a second prototype. With regards to the future use, an as compact as possible, integrated design has been focused on.

To investigate the second prototype, a dedicated beamline for detector tests and the simulation of slowed down beams was built at the Cologne FN tandem accelerator. This testbed is open to the collaboration and has already been used successfully.

Contents

1. Introduction

1.1. The emergence of radioactive ion beam facilities

In recent decades several techniques to produce beams of radioactive ions, so called RIBs, have evolved. Thus it became possible to probe the structure of nuclei far off the valley of stability.

These techniques are mostly based on projectile fission, spallation or fragmentation induced by high energetic stable ion beams and are of challenging technical demands, since one often needs to separate the desired ion from a vast amount of produced ones. The ratios between both are often very poor and thus high effort is needed in terms of detection and accelerator techniques.

Therefore only few, mostly large international laboratories are capable to deliver such beams. A common drawback of all facilities is a rather low production rate, which is the reason why the term *exotic beams* was established. When it comes to the production itself, one can determine different approaches to certain regions in the nuclear chart.

ISOL facilities The abbreviation ISOL stands for **I**sotope **S**eparator **O**n-**L**ine. In general one uses a high energetic (typically in the order of $\approx 1-2\,\mathrm{GeV}$) proton beam impinging on a large volume target made of a material with a high Z value (often Uranium). Thereby a spallation, fission and fragmentation of the target material is induced. Due to the extreme temperature of up to 2000 °C radioactive ions diffuse out of the material and are extracted [Jon93]. For most nuclear structure studies they are then collected in a trap, which is tuned in a way that only desired ions are caught. Afterwards they are bred to a higher charge state and finally re-accelerated to the experimental setup [Hab98].

One major disadvantage of this technique is the rather long time span until the ions are delivered to the experimental setup, including evaporation, trapping, breeding and re-acceleration of the ions. Because of shorter lifetimes one can not use ions too far away from the valley of stability, e.g. close to the neutron drip line. On the other hand, the production rate is fairly high compared to other techniques and the typical beam energies of $\approx 1-10\,\mathrm{MeV/u}$ benefit most nuclear structure studies.

Prominent facilities are the REX-ISOLDE laboratory situated at CERN [1] in Geneve or SPIRAL [2] at GANIL [3] in Caen [Hab98, Vil03].

[1] **C**onseil **E**uropéen pour la **R**echerche **N**ucléaire
[2] **S**ystème de **P**roduction d'**I**ons **R**adioactifs **A**ccélérés en **L**igne
[3] **G**rand **A**ccélérateur **N**ational d'**I**ons **L**ourds

FRS facilities So called **FR**agment **S**eparators (or rarely **F**ast **R**ecoil **S**eparators) take advantage of high energetic heavy ion beams and an in-flight RIB separation. Hence the name *in-flight separator* is quite common. Most common are energies up to $\approx 1\,\mathrm{GeV}$. The primary beam with a high total kinetic energy (TKE) bombards a cooled target made of a low Z material (mostly Beryllium or Lithium), resulting mostly in fragmentation of the primary ions. The other mechanics contribute as well. For instance for neutron rich ions, in-flight fission plays an important role. The ions eject from the target with a high TKE , mostly in the order of some hundreds of MeV. This secondary beam, a beam cocktail consisting of all kinds of ions, is sent through a set of properly tuned dipole magnets. Two dipole magnets perform an A/Q selection, followed by an achromatic degrader. For light to mid-heavy ions, q equals Z in most cases, that an A/Z selection is performed. The thickness of the degrader is important to the energy loss of the residual ions and therefore Z separation. Afterwards a second set of dipoles, a so called secondary ion beam consisting mostly of the desired specimen and energy is provided to the experimenter [Mü92, Gei92, Gei95].

A major advantage of this approach is the prompt separation at relativistic energies and therewith no need for a re-acceleration of the RIB. Thus fast decaying ions off the valley of stability (e.g. up to the neutron drip-line) become available. However, the price is a radioactive ion beam with a high TKE, which in general produces a vast amount of background: firstly by additional kinds of ions, which cannot be cut off the cocktail beam and secondly by radiation. One normally needs a specialised setup of auxiliary detector systems to select proper gates or triggers in order to handle such experiments.

Global leading facilities of this kind can be found at GSI [4] *Helmholtzzentrum für Schwerionenforschung GmbH* or NSCL [5] at *Michigan State University*.

To conclude, the ISOL technique uses a high Z-value target, from which it collects and re-accelerates the evaporating ions to the desired energy, while the FRS technique uses a high Z-value primary beam in a way that one can transfer its high momentum to the fragmentation products. The advantage of the first one is a low energetic RIB at the price of a higher, minimum half-life of the ions. The advantage of the latter is the availability of shortest lived exotic ions at the price of a rather high energetic RIB , way above the nucleus Coulomb Barrier.

Beside these two major and most prominent approaches one can find different other ones. For instance the LOHENGRIN spectrometer at Institut Laue-Langevin, which uses fission induced by neutrons and a set of a large dipole magnet and an electrostatic deflector to separate only for A/Q [Arm76, Fio93]. Another approach is the future ARIEL facility at TRIUMF in Canada, which uses photon induced fission [Kos08a].

[4] previously "**G**esellschaft für **S**chwer**I**onenforschung"
[5] **N**ational **S**uperconductiong **C**yclotron **L**aboratory

As mentioned before, a major difficulty of all facilities is a rather low production rate, which calls for improvements. By the beginning of the 2010s nearly all facilities worldwide announced or already started planning to do so [Lin04]. Those improvements will result in higher production rates, more brilliant beams and more parallel experiments at the same time. In table 1.1 the major changes of leading facilities are summarised. Of course, such improvements go along with a high demand for the development of new instrumentation and experimental methods to fully exploit their possibilities.

Table 1.1.: Overview over current improvements of leading RIB facilities [Gal03, Gal10, Lax03, Lin08, Sak08, Win08].

ISOL facilities			**FRS facilities**		
Facility	**First systems**	**Next generation**	**Facility**	**First systems**	**Next generation**
GANIL	SPIRAL	SPIRAL-2	GSI	FRS	SuperFRS
TRIUMF	ISAC-1	ISAC-2 (operational)	RIKEN	RIPS	BigRIPS (operational)
CERN	REX-ISOLDE	HIE-ISOLDE	NSCL	A1900	FRIB

1.2. From GSI to FAIR

The current GSI accelerator complex will be upgraded to the new **F**acility for **A**ntiproton and **I**on **R**esearch (FAIR) in the upcoming years. Thus the GSI with its unique UNILAC linear accelerator and the adjacent SIS 18 heavy ion synchrotron will function as an injector for the new SIS 100/300 synchrotron of FAIR. In this context, a new in-flight separator will be built. The so called SuperFRS will separate radioactive isotopes on a nanosecond scale (i.e. the time of flight through the separator) up to uranium at relativistic energies. The superconducting magnets will have a large angular acceptance and thus the separator will be the most powerful system of its kind when it comes to major beam parameters, including beam current and brilliance. The primary beam will deliver maximum 10^{12} ions/s at 1.5 AGeV for nearly all elements up to uranium. The primary beam luminosity will be increased by a factor of $100-1000$ compared to current GSI beams [Gei03, Win08].

The RIB will be divided into three different experimental areas which are combined in the NUSTAR[6] collaboration. For nuclear structure studies the so called Low Energy Branch (LEB) will be of major importance. The term *low energy* refers to a typical beam energy of $\approx 100-300$MeV/u [FAI12]. A sub-collaboration involved in the instrumentation and future physics campaigns of the LEB have been formed. The

[6] **N**uclear **St**ructure, **A**strophysics and **R**eactions

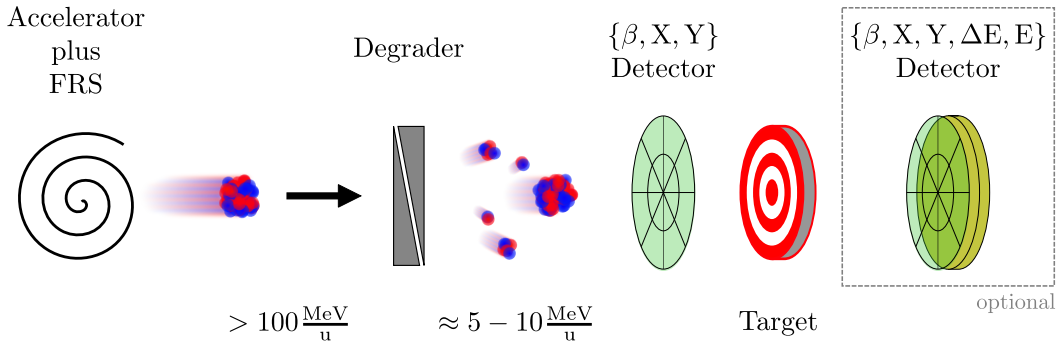

Figure 1.1.: A conceptual drawing of a slowed down beam setup, as being planned for FAIR.

name HISPEC/DESPEC [7] is chosen with respect to the two major approaches on how to investigate the nuclear structure [Rub06, Pod06, Pod08].

The campaign aims at a high combination of the detection of different information carriers from the reactions. This will become inevitable when it comes to experiments where one expects only several counts per hour or even less, to ensure a maximum of accuracy and efficiency in distinguishing wanted events from unwanted. Therefore several new instruments are being developed within the collaboration to ensure a maximum possible interoperability between the systems and setups with a maximum possible efficiency. Arising from these new systems, new experimental methods evolved, as well.

1.3. The Slowed Down Beam Method

One idea for a new experimental method for FAIR is a slowed down beam setup for the low energy branch of the SuperFRS. As the name suggests, one radically slows down a relativistic RIB to a few MeV/u. Thereby a complete new field of research with extremely short lived radioactive, low energetic ions will become accessible. Nowadays high beam energies are mostly tolerated out of necessity, which results in so-called fast beam measurements. Due to the excess of the Coulomb Barrier energy one gets a high background contribution from nuclear interactions. Especially while studying higher Spin states in the nuclei via Coulomb excitation, one would favour lower beam energies due to the relatively longer interaction time between projectile and target nuclei [Gla01].

The basic principle of such a planned setup can be seen in figure 1.1. A RIB will arrive at the focal plane of the SuperFRS and be slowed down harshly by simply putting a double wedge shaped degrader in its way before it reaches the target. The thickness of the degrader has to be adjusted concerning to the desired decrease in energy. Energies before the degrader will be in the order of $\approx 100 - 300$ MeV/u and afterwards $\approx 5 - 10$ MeV/u. Beside slowing down the primary RIB, such a process

[7] **H**igh-resolution **I**n-flight **SPEC**troscopy/**DE**cay **SPEC**troscopy

will lead to a vast amount of secondary fragmentation products. Furthermore, the ions will undergo a spread in space and energy (see 2.1).

It is crucial to supply the experimenter with information on whether a slowed down ion of interest from the primary RIB hits the target or not, i.e. whether a secondary fragmentation ion is introduced by the degrader. This information has to be gathered somewhere in between the degrader and the target while keeping an interaction with the beam at a minimum. Thus a detector should be as transparent as possible concerning the ions. Hence a calorimetric detection is not possible. In fact, it should deliver a precise **T**ime **O**f **F**light (TOF) measurement and function as a position (X and Y) sensitive **B**eam **P**rofile **M**onitor (BPM) for each passing ion. Thus it delivers a gate for the experiment and can correct for the spatial spread. The valuable TOF information will allow the determination of the β factor, given by the ratio of the ions speed v and the speed of light c:

$$\beta = \frac{v}{c}$$

All this has to be measured with highest accuracy and on an event by event basis for every single ion. Thereby a complete tracking is possible.

A possible second system behind the target will gather the same information in addition to a $\Delta E - E$ telescope. Both systems combined will make it possible to reproduce the whole kinematics of every ion in between the degrader and the beam stop, including their kinematics before and after a reaction in the secondary target. A prototype of the second detector system was built and tested [Tay09]. Currently it is being upgraded to its full capacity. Of course, such a second system is optional and only of interest if the energy of the slowed down RIB is high enough or the target thickness is thin enough to be pinched through, i.e. for a stopped beam setup this detector would be of no use.

However, all this information will be of highest importance to the experimenters to filter out and normalise (e.g. correct for Doppler shifting and hit pattern of the target) the events they aimed for. The summarised demands to such a detector system are:

- A large active area to address the divergence of the slowed down beam
- It should be kept compact in order to fit between the degrader and the target
- The amount of material obstructing the beam has to be kept at a minimum
- The timing resolution should be in the order of some few hundreds of picoseconds
- Its spatial resolution should be in the order of roughly one millimetre

Especially the latter two points are important with regard to an energy and spatial straggling, introduced by the slowing down of the ions. The aim of this thesis was to develop a detector system which is capable to fulfil these requirements.

2. Considerations on slowed down radioactive beams

To justify the development of a specialised detector system for a certain method, one should first study the feasibility of such a system. In this case of identifying slowed down radioactive ions only by means of the TOF , the minimum requirements to the detector should be investigated. Therefore a deeper understanding of the underlying, physical processes of slowing down ions is needed, which will be discussed in this section. Afterwards a typical example case is simulated with this theoretical background, from which tentative detector specifications can be deduced.

2.1. Theoretical aspects

The major issues concerning the interaction of relativistic high Z ions with matter are [Sch98]:

- Projectile excitation, ionisation and charge states
- Stopping power (including several corrections)
- Energy-loss straggling
- Angular straggling

One major parameter concerning the calculation of the above mentioned effects is the so-called Sommerfeld parameter, which functions as an index whether a classical or a quantum mechanical perturbation calculus is applicable [And94]

$$\eta = \alpha \frac{Z_p}{\beta} = \begin{cases} \gg 1, & \text{classical treatment} \\ \ll 1, & \text{perturbation treatment} \end{cases}$$

where α is the fine-structure constant and Z_p is the atomic number of the projectile. Even nowadays the SIS synchrotron at GSI delivers mostly ions with an ionisation grade of $> 90\%$ at high energies, i.e. large β values. Hence, the perturbation treatment is of major interest for the calculation of slowed down RIBs at FAIR .

The following sections will briefly summarise the theoretical treatment of the above mentioned issues.

2.1.1. Projectile Excitation, Ionisation and Charge States

For a simplified calculation of the first order perturbation cross section for projectile excitation, ionisation and the charge state distribution, the sum of the classical (i.e. non-relativistic) and relativistic contributions is sufficient [Anh79].

$$\sigma_{total} = \sigma_{classical} + \sigma_{relativistic}$$

The impact factors of the contributions are proportional to the Lorentz factor

$$\gamma = \frac{1}{\sqrt{1-\left(\frac{v}{c}\right)^2}}$$

and thus increase with a rising velocity of the ions, known as *relativistic rise*. For GSI like beam energies, a consequence of this effect is the so-called Lorentz boost which describes a conical convolution of the preferred direction of emittance of the gamma radiation, oriented in the direction of flight.

2.1.2. Stopping Power

Concerning the more complicated calculation of the stopping power at relativistic energies, several corrections are necessary. All are based on the well known relativistic treatment of the classical Bloch based Bethe formula defining the stopping power as the loss of energy per unit path length [Bet32]

$$\begin{aligned} -dE/dx &= \frac{4\pi Z_p^2 e^4 N}{mc^2\beta^2} \cdot \left(\ln\frac{2mc^2\beta^2}{I} + \ln\gamma^2 - \beta^2\right) \\ &= \frac{4\pi Z_p^2 e^4 N}{mc^2\beta^2} \cdot L_{\text{Bethe}} \end{aligned}$$

N defines the number of electrons per unit volume of the target material, I the target atoms ionisation potential and L_{Bethe} is introduced as stopping number. In general, there are six corrections being applied over the last decades, which will be summarised briefly [Sch98]:

Barkas effect

Addresses a reduction of the effective collision energy for positive ions by a factor of $1/\beta^2$ and is thus only of concern for lower velocities.

Shell corrections

Takes into account the relative difference between projectile velocities v_p and orbital velocities of bound target electrons v_t and thus the less effective energy transfer when $v_p \lesssim v_t$. It decreases to zero with rising γ and contributes by a factor of $1/\beta^2$.

Density effect

Due to the Lorentz boost, induced by the relativistic rise, polarisation effects can occur. These in turn result in electromagnetic screening effects, making the energy transfer less effective for higher density target materials at higher velocities, i.e. larger impact factors with more dense target materials and higher velocities. Its positive contribution by a factor of 1/2 increases with rising γ.

Bloch correction

For small impact parameters the Coulomb field based scattering angles become small and result in small momentum transfers. Thus its scattering amplitudes have more impact than the use of a first order Born approximation predicts. In addition a first order perturbation is sufficient for larger distant collisions, due to the independence of the projectiles charge magnitude. It corrects negatively with a larger impact at lower values for γ and gets energy-independent at higher energies.

Mott correction

When it comes to large momentum exchanges between the projectile and target electrons, large scattering angles can occur, influencing the cross section. Still, the calculation of the cross sections it is sufficient to treat the bound electrons as free electrons with respect to Z_p and γ. The correction limits to zero for small Z_p and small β. It is positive for positive projectile charges and vice versa and gets energy-independent at higher energies, as well.

Lindhard-Sørensen correction

The last major correction takes into account the tremendous impact of the nuclear charge distribution for very high energetic, heavy projectile ions, while being slowed down. The differential cross section for a point charge for different scattering angles is constant in first order. If the nuclear charge distribution is convolved with the point-like charge distribution, the cross section manifests a diffraction like shape with extrema. The cause of the difference between those two cross sections is called Lindhard-Sørensen effect for finite size nuclei.

Figure 2.1 show the contributions of the above mentioned corrections to the stopping power for varying $\gamma - 1$. Thus only the density, Bloch, Mott and Lindhard-Sørensen (LS) corrections apply for high γ. Hence, the Bethe formula is extended to

$$-dE/dx = \frac{4\pi Z_p^2 e^4 N}{mc^2\beta^2} \times \left(L_{\text{Bethe}} + \Delta L_{\text{Bloch}} + \Delta L_{\text{Mott}} + \Delta L_{\text{LS}} - \gamma/2\right)$$

for relativistic heavy ions.

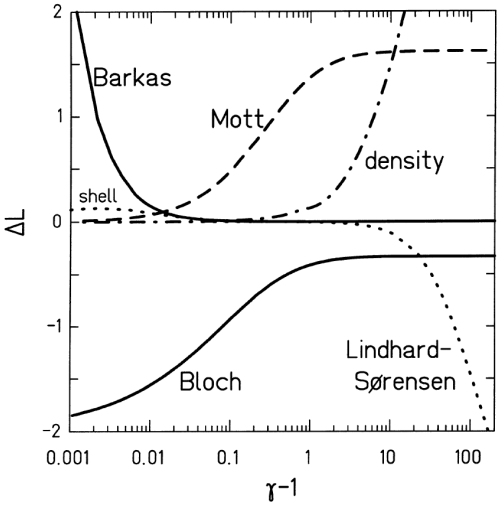

Figure 2.1.: The contribution ΔL of each correction term to L_{Bethe} over $\gamma - 1$ for lead ions hitting an aluminium target, taken from [Sch98].

2.1.3. Energy-loss Straggling

The third issue one has to consider for a complete treatment of the interaction of such ions with matter is the energy-loss straggling. Close collision with electrons of the target material and the projectile charge distribution account for the major impact of this effect. It can be calculated by

$$\Omega^2 = 4\pi Z_p^2 e^4 N \cdot \Delta x \cdot \gamma^2 \cdot X$$

where Δx is the thickness of the target material and X the so called straggling parameter [Lin96]. For $\eta \gg 1$ cases, i.e. classical treatment like Rutherford scattering, $X = 1$ applies. For intermediate energies of $\gamma \simeq 2$, it increases up to $X \simeq 3$ for very heavy ions. For higher energies and larger Z_p, the LS effect reduces X. The higher Z_p, the lower is the value of γ, where X starts decreasing. Thus for highly relativistic, very heavy ions being slowed down, $X < 1$ and therewith the straggling of the final ion energy gets fairly small.

2.1.4. Angular Straggling

At last one has to consider the angular straggling of the decelerated ions. Again, for $\eta \gg 1$ cases, a classical Rutherford Scattering is applicable. For other cases multiple Coulomb scattering takes effect, which has been found to be described by the semi-empirical formula [Hig75, Lyn91, Sch98]

$$\sigma^2 = \frac{Z_p^2 \cdot 190\,\mathrm{MeV}^2}{\left(p\beta c\right)^2} \frac{\Delta x}{L_{\mathrm{rad}}} \cdot \left[1 + 0.1 \log\left(\frac{\Delta x}{L_{\mathrm{rad}}}\right)\right] \mathrm{rad}^2$$

with p being the momentum of the projectile and L_{rad} the radiation length of the target. The latter depends logarithmical on the atomic number of the target material and is directly proportional to its mass number. Thus the angular straggling rises with thicker and more dense targets in first order.

Now that all major issues concerning the interaction of relativistic high Z ions with matter are mathematically described, one can simulate the deceleration of such ion beams. This can be done by the well established software LISE++ developed at the Michigan State University [Tar08], which is in principal a graphical user-front-end for various underlying codes calculating the above mentioned interactions for self-built ion optical geometries and experimental setups.

2.2. Simulation of slowed down ^{96}Kr as case example

As an example, unstable ^{96}Kr was chosen as a typical nucleus of interest [Alb12]. The simulation was done with a 250 MeV/u primary beam with a current of 0.01 pnA, which equals roughly $6.25 \cdot 10^7$ primary particles. The degrader thickness was chosen to be 3630.6774 μg/cm^2 of aluminium in order to get a mean value of 10 MeV/u for the slowed down ions. Another assumption is a point-like beam spot of the primary ions.

For this case, table 2.1 summarises the simulated parameters of the 40 most prominent ions after the slowing down process for a 1σ proximity of the yield distribution. As one can clearly see, the yield of slowed down ^{96}Kr ions is around three orders of magnitude larger than for secondary fragmentation ions. Thus with 77.65% the bulk of the primary RIB will survive, including a quite low energy spread of only 1.645 MeV FWHM[1]. The other 39 most prominent secondary particles have a much larger energy and angular distribution. Both the energy distribution and the angular distribution of all ions are plotted in figure 2.2.

If one gates with a TOF window according to this energy window, most of the triggered events will correspond to the desired ions. Not wanted secondary fragmentation ions matching these conditions will be either isobaric ions with the same mass and energy or ions of different mass with a matching energy in order to pass such gate conditions. Anyhow, both cases have a small probability in comparison to the desired events. The timing window corresponding to 1σ of the Gaussian distribution of the slowed down ^{96}Kr ions is 6.8942 ± 0.24593 ns for a TOF distance of 30 cm. All secondary fragmentation isotopes, whose 1σ TOF range overlaps with this window, are shown in table 2.2. If one takes into account the full 1σ ion amount of each secondary fragment and thus ignores the partial overlapping, one can estimate an upper limit for their amount. For the discussed case, the summed up overlapping

[1] **F**ull-**W**idth-**H**alf-**M**aximum, meaning the width of the distribution at half its amplitude

contaminants account for less then 1.77% of the gated events, which is in the order of statistical fluctuations. Thus, if the overall timing resolution of the highly transparent TOF detector sitting between degrader and target is in the order of below $2 \cdot 0.24593 = 0.49186$ ns, the method is applicable for experiments of this kind.

Other calculations showed similar results for other relativistic, heavy ions [Bou08, Naq11b]. In 2007 a real proof-of-concept measurement with promising results has been performed at the FRS focal plane at GSI . A ^{64}Ni primary beam with 250 MeV/u was slowed down to round about 13 MeV/u with a 3.95 μg/cm^2 aluminium degrader [Naq11a].

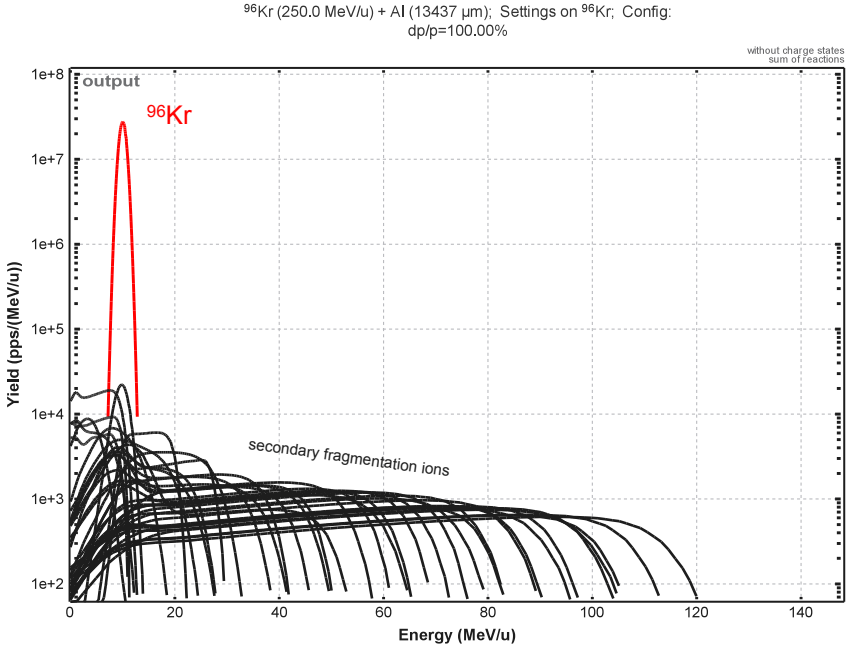

(a) Fragmentation yields versus the energy distribution.

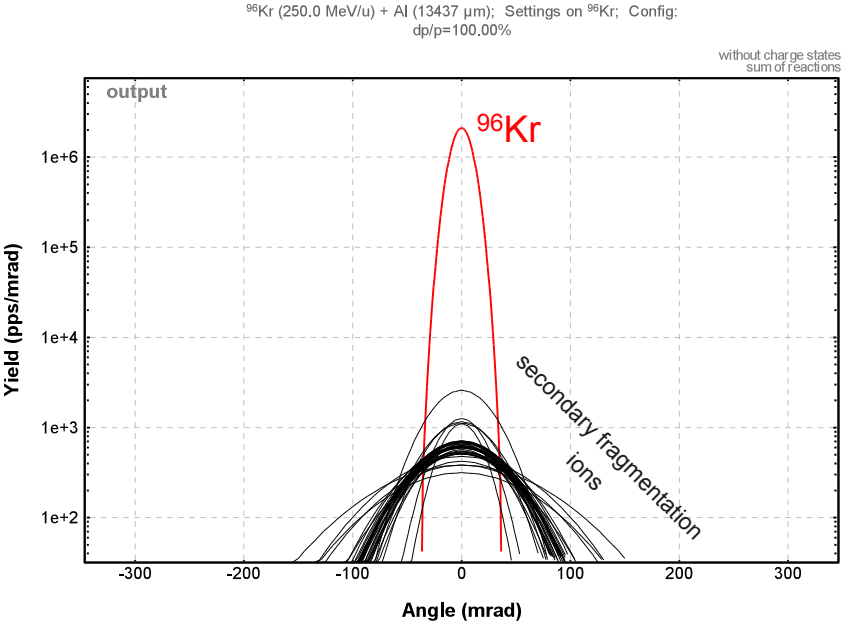

(b) Fragmentation yields versus the angular distribution.

Figure 2.2.: Simulated fragmentation yields for all ions after the slowing down process, once in depence of the energy (a) and once of the emittance angle (b). In both figures the curves account for 1σ of each distribution. The simulation was performed with the LISE++ program package.

Table 2.1.: Simulated parameters for the 40 most prominent ions after the slowing down process of ^{96}Kr. The simulation was performed with the LISE++ program package.

N	Slowed Down Ion	Mean Energy [MeV]	Maximum Energy [MeV]	Energy FWHM [MeV]	Angular Spread FWHM [mrad]	Yield [counts] for 1 σ	Percentage of initial ^{96}Kr ions
1	^{96}Kr (beam)	10.01	10.01	1.645	21.66	4.85E+007	77.65%
2	^{95}Kr	5.258	7.5	10.01	63.73	1.76E+005	0.28%
3	^{94}Kr	5.274	8.044	10.01	70.2	8.24E+004	0.13%
4	^{91}Br	9.568	9.782	3.216	64.21	7.92E+004	0.13%
5	^{68}Zn	11.22	9.915	13.99	134.1	6.81E+004	0.11%
6	^{69}Zn	17.9	17.72	18.89	96.98	6.80E+004	0.11%
7	^{65}Cu	16.48	8.445	25.39	102.8	6.62E+004	0.11%
8	^{63}Ni	18.19	11.81	9.202	87.29	6.61E+004	0.11%
9	^{60}Co	31.65	9.169	55.46	88.33	6.61E+004	0.11%
10	^{72}Ga	8.246	7.906	9.405	162.5	6.61E+004	0.11%
11	^{66}Cu	18.98	8.206	8.945	89.82	6.60E+004	0.11%
12	^{92}Br	14.64	16.8	10.67	47.97	6.42E+004	0.10%
13	^{57}Fe	38.46	54.11	59.38	89	6.42E+004	0.10%
14	^{62}Ni	22.49	8.896	38.47	95.17	6.37E+004	0.10%
15	^{55}Mn	45.69	62.89	65.19	87.51	6.32E+004	0.10%
16	^{58}Fe	41.9	57.4	58.88	82.82	6.27E+004	0.10%
17	^{61}Co	37.68	51.67	54.1	81.66	6.05E+004	0.10%
18	^{52}Cr	49.19	68.05	70.78	92.07	6.03E+004	0.10%
19	^{59}Co	32.03	39.92	40.17	94.83	6.02E+004	0.10%
20	^{64}Ni	33.01	45.51	48.72	79.9	5.80E+004	0.09%
21	^{54}Mn	42.48	59.7	64.95	91	5.80E+004	0.09%
22	^{50}V	56.45	79.48	87.96	91.46	5.77E+004	0.09%
23	^{90}Br	4.232	1.136	7.743	86.32	5.74E+004	0.09%
24	^{53}Cr	52.78	74.28	82.24	86.66	5.68E+004	0.09%
25	^{67}Cu	25.94	12.88	37.71	80.49	5.57E+004	0.09%
26	^{73}Ga	12.9	8.675	15.26	94.9	5.53E+004	0.09%
27	^{70}Zn	22.81	28.23	29.38	82.68	5.49E+004	0.09%
28	^{64}Cu	11.88	9.21	16.09	132.8	5.42E+004	0.09%
29	^{47}Ti	58.5	80.83	82.05	95.01	5.43E+004	0.09%
30	^{56}Mn	49.06	68.98	76.52	82.13	5.32E+004	0.09%
31	^{49}V	52.48	73.09	76.42	95.29	5.27E+004	0.08%
32	^{45}Sc	66.43	92.69	96.68	96.39	5.21E+004	0.08%
33	^{48}Ti	62.19	87.11	92.88	91.24	5.20E+004	0.08%
34	^{56}Fe	34.58	45.63	50.18	96.13	5.15E+004	0.08%
35	^{93}Kr	4.933	7.473	9.417	73.89	5.00E+004	0.08%
36	^{61}Ni	19.73	10.79	32.39	109.6	4.92E+004	0.08%
37	^{76}Ge	3.562	3.434	5.898	144.7	4.85E+004	0.08%
38	^{93}Br	18.67	25	18.34	41.08	4.81E+004	0.08%
39	^{51}V	58.83	82.13	86.96	86.81	4.80E+004	0.08%
40	^{59}Fe	45.07	63.36	70.66	79.03	4.78E+004	0.08%

Table 2.2.: Simulated parameters for all secondary fragmentation products, whose 1σ TOF range overlaps with the one of ^{96}Kr ions. The simulation was performed with the LISE++ program package.

N	Slowed Down Ion	TOF [ns] for 30cm	1σ TOF range [ns]	TKE [MeV]	1σ TKE range [MeV]	Yield [counts] for 1 σ	
1	^{96}Kr (beam)	6.8942	0.24593	959.12	57.036	4.85E+007	
2	^{91}Br	7.0922	0.50208	868.34	119.28	7.92E+004	
3	^{68}Zn	6.9689	1.4276	754.93	300	6.81E+004	
4	^{65}Cu	6.0329	1.5818	1057.1	527.15	6.62E+004	
5	^{63}Ni	6.1639	2.0552	1127.6	687.78	6.62E+004	
6	^{72}Ga	8.0904	1.6302	587.65	229.34	6.61E+004	
7	^{66}Cu	5.7535	1.661	1242.4	674.36	6.60E+004	
8	^{92}Br	5.7969	0.57593	1344.2	262.48	6.42E+004	
9	^{73}Ga	6.5072	1.3561	936.65	378.78	5.53E+004	
10	^{64}Cu	6.9271	1.6203	749.11	336.15	5.42E+004	
11	^{86}Se	7.587	0.81694	730.44	155.26	4.70E+004	
12	^{77}Ge	7.4397	1.3853	731.39	265.49	4.45E+004	
13	^{87}Se	5.9163	0.70709	1236.3	291.9	3.75E+004	
14	^{71}Zn	6.6013	2.3341	1155	736.34	3.71E+004	
15	^{82}As	6.2296	0.87786	1067.2	296.92	3.27E+004	1.77% of
16	^{60}Ni	7.6062	2.2756	648.72	360.01	2.80E+004	^{96}Kr yield
17	^{57}Co	6.3103	2.0273	946.34	559.73	2.05E+004	
18	^{59}Ni	8.8534	2.3782	443.01	223.66	1.21E+004	
19	^{56}Co	8.0635	2.7445	585.5	360.57	7.83E+003	
20	^{97}Kr	6.2001	0.56437	1229.4	219.37	2.40E+003	
21	^{55}Co	8.4531	2.3617	462.28	241.61	2.17E+003	
22	^{50}Mn	5.7138	1.8519	1026.8	613.79	1.82E+003	
23	^{52}Fe	6.0823	1.3923	788.67	348.26	1.06E+003	
24	^{49}Mn	5.8836	1.6872	877.55	473.24	3.30E+002	
25	^{51}Fe	10.524	3.5982	311.32	191.66	1.28E+002	
26	^{48}Mn	6.3707	1.6158	688.19	332.72	7.06E+001	
27	^{98}Kr	5.9237	0.83041	1413.4	391.5	4.80E+000	
28	^{45}Cr	8.0031	3.3892	591.48	428.83	5.60E-003	
29	^{47}Mn	9.3129	2.79	337.02	186.6	2.00E-003	
30	^{44}Cr	7.3024	2.3241	537.78	314.4	3.25E-004	

3. Instrumentation

In this chapter the basic design idea of the detector and its major components are presented. Besides, each component will be discussed theoretically.

3.1. Basic Detector Design

As mentioned in section 1.3, the detector has to be as compact as possible while having a maximum possible active area and keeping the absolute amount of material obstructing the beam at a minimum. There are basically two systems which fulfil these demands, namely gas filled detectors (like Multi-Wire-Proportional-Chambers or Time-Projection-Chambers [Cha70, Mar78]) and so-called thin foil detectors.

The former do not match the desired parameters, especially concerning the timing resolution, which is typically in the order of several tens to hundreds of nanoseconds for such systems. Therefore the only option left is a thin foil based detector design. A thin conversion foil is placed in the beam and set to a certain voltage. When the ion beam pinches through the foil, **S**econdary **E**lectrons (SE) are emitted. While the ions will advance on their trajectory, the electrons are accelerated and confined out of the trajectory of the ions by electrostatic or magnetic fields towards an electron detector. In most thin foil detectors, this electron detector is based on a **M**icro **C**hannel **P**late (MCP). The SE are multiplied in the MCP emerging in an electron shower, which gives a fast timing signal before they are detected by an anode.

Early attempts of such detection concepts have been made with small sized detectors only used for timing purposes [Gab75, Wei79]. First systems with integrated position sensitivity have, for example, been developed at the *Laboratory Nazionali di Legnaro* in Italy and at GANIL in France [Mon05, Odl96]. Both used electric and magnetic fields for the definition of the SE trajectories, while the latter used an additional electrostatic field to further focus the trajectories. However, both systems have in common that the emissive foil is tilted by 45° with respect to the beam axis. The desired detector output is a $1:1$ projection of the hit pattern of a plane orthogonal to the beam axis, i.e. a not tilted foil. Taking the not tilted component of the foil as X-axis and the tilted one as Y-axis, one will only get a $1:1$ projection for the X-axis, while the projection of the Y-axis will always be decreased by a factor of $\sqrt{2}$. Furthermore, the coils being used to introduce the magnetic field need a rather large space. Beside the mechanical problems arising, such space will not be available at the future FAIR setup, as mentioned in section 1.3.

In order to avoid such problem, the solution being investigated in this thesis is in principle based on the design of STARZECKI ET AL [Sta82], where a not tilted foil is

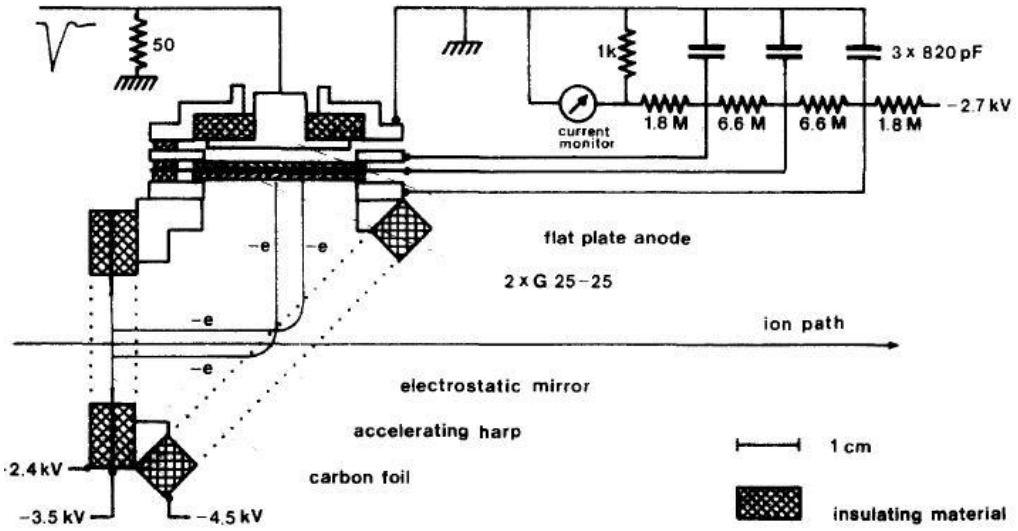

Figure 3.1.: A schematic drawing of the original time zero detector design of STARZECKI ET AL, taken from [Sta82].

used and the SE are confined with an electrostatic field. Similar designs followed quite fast [Kav85]. The electrostatic field is induced by harp wires, which define a triangular shaped, field free drift region, as shown schematically in figure 3.1. The SE are reflected by 90° towards the MCP, which is then read out by an anode. The price for the achieved 1 : 1 projection is the additional material of the wires obstructing the beam. By choosing proper potentials and wire distance to diameter ratios, the influence on the passing ion can be minimised.

As an enhancement of the original design, the detector being developed in the framework of this thesis is equipped with a position sensitive **D**ual **D**elay **L**ine (DDL) anode. Additionally, the active area has to be enlarged with respect to the divergent slowed down RIB. The size of the foil has to be at least the size of the detector head, which is in turn limited by the size of the MCP available. In the beginning of the research and development (R&D) of the detector, this was a roughly 80x100 cm^2 Hamamatsu[1] F-Type MCP.

[1]Hamamatsu Photonics Deutschland GmbH, Arzbergerstr. 10, D-82211 Herrsching am Ammersee, Germany

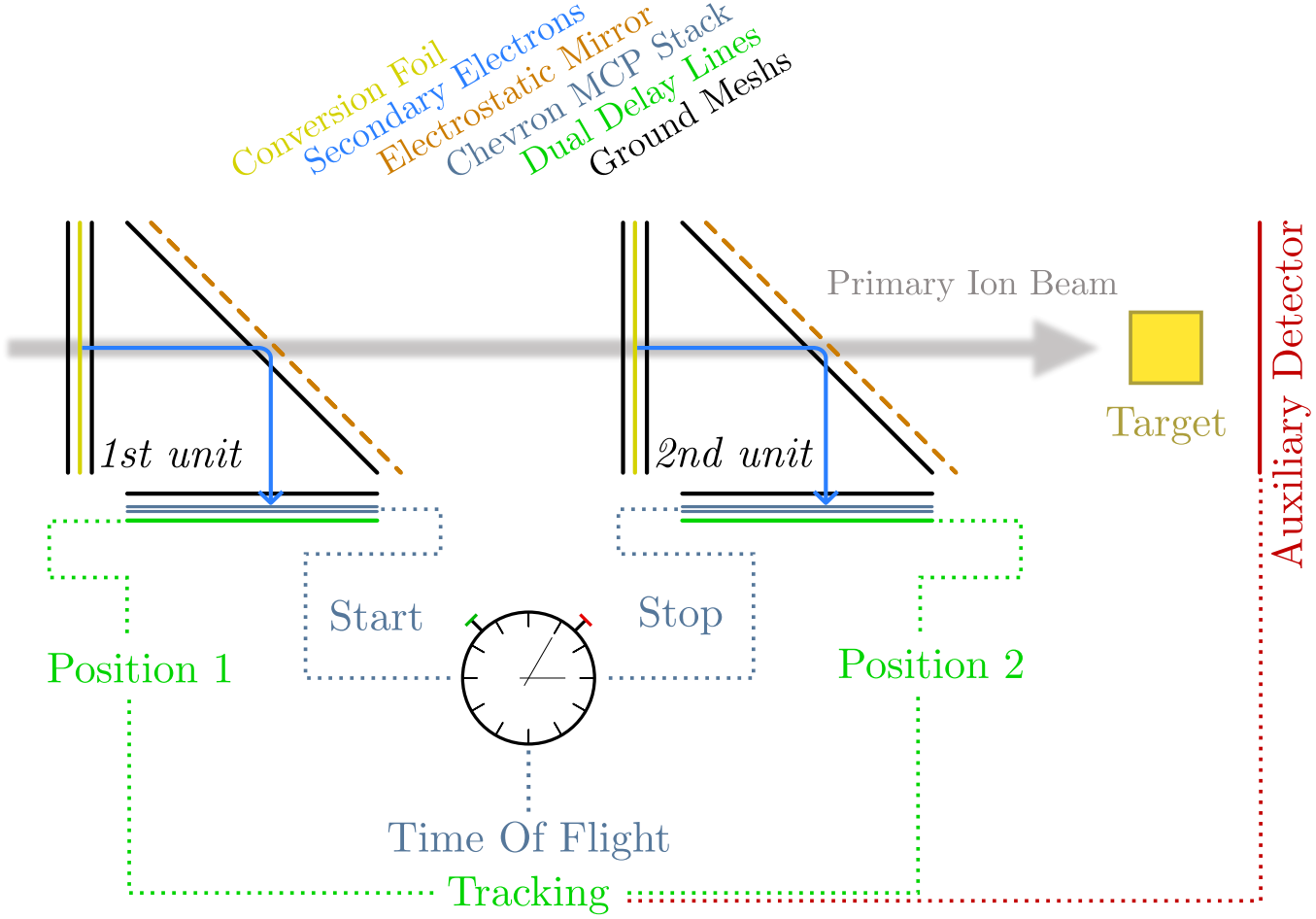

Figure 3.2.: A schematic drawing of the basic detector components and signal ways for a fully mounted setup for beam tracking and included TOF measurement. Note that the schematics of a single unit represent the second prototype, as described in section 4.2.

In principle one can divide one unit into three functional groups, which make each unit quite modular in terms of maintenance, namely a

- *Conversion Module*
  produces the secondary electrons and accelerates them towards the
- *Reflecting Module*,
  which deflects the electrons by 90° towards the
- *Detector Head*
  where the electrons are multiplied and registered.

If two such units are placed alongside the primary beam axis, one is able to reconstruct the trajectories and TOF of all passing ions on an event-by-event basis. The first unit gives initial signals for both the two dimensional positions of the passing ion in a plane perpendicular to the beam axis (i.e. the conversion foil) and the timing. The second unit provides the final signals of those parameters. Knowing the distance between the two units one can project the trajectory with both position information and measure the TOF and therewith the velocity of each ion, as shown in figure 3.2.

3.2. Conversion Module

3.2.1. Theoretical aspects of SE emission

The first widely accepted and most credible theoretic model of ion induced SE emission has been proposed by STERNGLASS [Ste57]. His model is based on two independent parts. First the formation of SE within the material, i.e. the thin foil, and secondly the emittance from the foil surface afterwards. More modern theories expand this model by a transportation part between formation and emittance [Kos89]. However, all approaches result in the total yield of SE , whereas for this case only the forward-emitted ones, i.e. in direction of beam, are of concern. Since one wants to detect the passing ions on an event-by-event basis, one would like to have high yields to increase the detection probability.

The amount of introduced SE n within the material at depth x is directly proportional to its energy loss per unit path-length dE/dx. Now one needs to differentiate two cases, large and close distance collisions between the ion and an atomic electron of the foil material. Due to a high energy exchange and therewith perturbation of the atom, the latter case will result in only few, but high energetic electrons, so-called δ-electrons. Those will most probably introduce tertiary electrons in the foil. On the other hand, a distant, low energy exchange collision will directly result in SE with a mean energy loss $\overline{E}$ of the ion. KOSCHAR ET AL extended the Sternglass-theorem by a term $(1-\alpha)$, addressing the high velocity limit which says that at higher ion velocities the contributions of both cases to the total energy loss equilibrate to $\alpha = 0.5$. Thus one can express n for both cases [Kos89] as

$$
\begin{aligned}
n_{\mathrm{dist}}(x)dx &= (1-\alpha)\,\frac{1}{\overline{E}}\,\frac{dE}{dx}\bigg|_x dx \\
\text{and} & \\
n_{\delta}(x)dx &= \alpha\,\frac{1}{\overline{E}}\,\frac{dE}{dx}\bigg|_x f(x,L_{\delta})dx
\end{aligned}
$$

with $f(x,L_{\delta}) = 1-\exp(-x/L_{\delta})$ being a function concerning the energy transport by δ-electrons in light foil materials. Since these can introduce tertiary electrons further away from the initial collision point, they account for a diffuse dissipation of the energy loss. L_{δ} is a typical transportation length in this context, but not to be confused with the mean free path L_{SE} of SE with energy $\overline{E}$. The total amount of SE is simply given by

$$n_{\mathrm{total}} = n_{\mathrm{dist}} + n_{\delta}$$

Going back to the original Sternglass-theorem, one then has to consider the emittance of the SE from the surface of the foil. The basic probability that a SE within the foil can emit is defined as [Ste57]

$$P(x) = \tau A \cdot \exp(-x/L_{\mathrm{SE}})$$

whereas τ is the surface transmission coefficient and A corresponds to the initial angular distribution of the SE. Both coefficients are, in a first order, properties of the foil material only. Following the enhanced model of KOSCHAR ET AL [Kos89], the total SE yield for a given foil thickness d is given by

$$\Delta_{\mathrm{total}} = \int_0^d n_{\mathrm{total}}(x)\cdot P(x)dx$$

Taking Bohrs approximate expression for dE/dx [Boh48], the yield of SE for a given material of the foil (τ and A as specific parameters) is only dependent on the initial velocity and the effective charge of the ion passing the foil. Especially the latter is equal to the projectile charge Z_p for bare, heavy ions.

3.2.2. Utilised foil materials

During the whole R&D phase of the detector, three different kinds of foils have been used. They all have a size of 80x100 cm^2 with respect to the active area of the detector head, as mentioned in section 3.1.

Polycarbonate + Aluminium Coating The very first foil being used was bought from Goodfellow GmbH[2]. The thickness of the polycarbonate was 0.24 $\mathrm{mg/cm}^2$ (2 µm), which was used as a backing material for a 0.0081 $\mathrm{mg/cm}^2$ (0.03 µm) evaporation of aluminium. The ratio of metallic coating to backing material is roughly 1 : 30 at a total thickness of 0.2481 $\mathrm{mg/cm}^2$. This type was found to be

[2] Goodfellow GmbH, Postfach 13 43, D-61213 Bad Nauheim, Germany

sufficiently robust concerning the handling, which was especially useful in the early phase of R&D when one had to vent the vacuum chamber more often or change basic parts of the setup. The big disadvantage is its comparably huge thickness, which accounts for additional straggling of the ions. Additionally, the pro rata amount of the SE emitting metal coating is very small. The foil itself was glued on a metal frame for electric contact, in order to apply the negative potential, as one can see in figure A.1.

Mylar + Gold Coating The second foil being used was delivered by the target laboratory of GANIL. It was a compound of 0.126 mg/cm^2 (0.9 µm) thick Mylar[3] with a 0.058 mg/cm^2 (0.03 µm) gold coating. The coating to backing ratio increases to roughly 1 : 2 at a reduced overall thickness of circa 0.184 mg/cm^2. It combines nearly the stability of the polycarbonate backing with less material obstructing the ion beam at a relatively and absolutely larger amount of SE emitting metal coating. The backing Mylar was glued on a frame shaped printed circuit board while the gold coating was evaporated afterwards, as shown in figure 4.2(a).

Self sustaining carbon The foil of choice for the final usage was pure, self sustaining carbon. It was drawn on thin metallic frames by the target laboratory of GSI. Its major advantage is that one can achieve a very small thickness and that the whole material accounts for the production of SE without the need of a backing material and thus the material obstructing the ion beam can be decreased to an absolute minimum. The only drawback is its stability decreasing heavily with decreasing thickness and increasing size, making them not suitable for an early R&D phase. The chance of breaking during evaporation or mounting is tremendous, while being very sensitive to vibrations, as well.

A systematical study of the SE yield Δ_{total} for carbon foils of different thicknesses being bombarded with 3.9 MeV/u sulphur ions of different charge state has been conducted, helping to choose the appropriate thickness for the foil [Kos89]. The results as seen in figure 3.3 indicate a saturation of Δ_{total} at roughly 40 µg/cm^2 for all combinations, which seems to be a good trade off between the handling of the foil and Δ_{total}.

For light hydrogen ions of 1.2 MeV/u a saturation of Δ_{total} is reached at even 0.01 mg/cm^2 thickness of the carbon foil, although the amplitude of Δ_{total} is only a fraction of the one for heavier ions [Kro88].

Thus the thickness of the foils delivered by GSI was chosen to be between 0.03 mg/cm^2 (0.133 µm) and 0.04 mg/cm^2 (0.178 µm) with respect to a maximum Δ_{total} for heavy ions in the 5 – 10 MeV/u regime.

[3] Mylar is a registered trademark for Bi-axially-oriented Polyethylene terephthalate (BoPET)

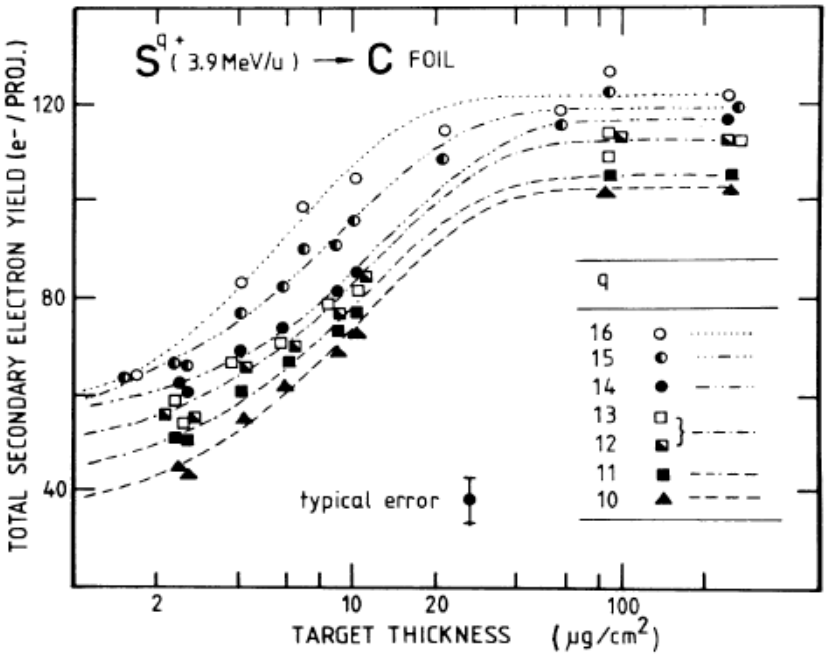

Figure 3.3.: SE yields for carbon foils of different thickness bombarded with 3.9 MeV/u sulphur ions of different charge states, taken from [Kos89].

3.3. Reflecting Module

3.3.1. Theoretical approaches on the transportation of SE

The two major tasks of the reflecting module are to provide a field free inner drift region of the SE and to confine their trajectory by 90° perpendicular to the beam axis. This is done by a set of wires or meshes, which in addition to the conversion module obstruct the ion beam. Of course, such a field cannot be fully homogeneous. Thus one should choose a wiring or mesh with an open area ratio, which is as large as possible, but as small as necessary in order to maintain an electrostatic field fulfilling the before mentioned tasks. Using foils instead of a wiring would indeed create a homogeneous field (if one neglects the side effects), but due to the electrostatic forces these need to have a certain thickness similar to the firstly used plastic foils mentioned in section 3.2.2. Since one would need a minimum of four foils, the overall amount of material obstructing the ion beam path would not be acceptable. Hence a solution with wires or meshes has to be chosen.

A disadvantage of this solution is the inhomogeneous field close to the wires, where cushion effects will appear. As a result, the electrons will not have the same TOF from foil to MCP over the whole active area, assuming they are all emitted exactly perpendicular to the conversion foil. For an ideal homogeneous field without material where SE can scatter, the distances travelled are the same, whether the SE are emit-

ted in a corner or in the middle of the conversion foil. Since the small, close by field disturbances introduced by the wires are constant, one could correct for these effects theoretically, assuming a pure injective imaging. The only effect left influencing the TOF of the SE would be the initial energy distribution of the SE . This is an intrinsic problem and cannot be overcome, but minimised by choosing a high accelerating field gradient to extract and direct the SE towards the reflecting module.

Independent of this problem, there is one superposing effect influencing the SE trajectories and TOF either one considers an ideal, material-free field or a wire-induced field. As touched in section 3.2.1 by the parameter A, the SE have an initial angular and energy distribution. Hence, even if a set of SE is emitted at precisely the same spot on the conversion foil and neglecting their energy distribution, they would enter the electrostatic mirror at different spots and thus have a varying flight path with varying TOF , as indicated in figure 3.4.

Early attempts to describe the flight path consider the field and the SE initial energy to be homogeneous and the angular dispersion to be negligible, all in first order. Assuming this idealisation and a deflection of the SE by 90°, the parabola inside the reflecting mirror can be described by means of the foil and mirror potential gradients, ΔV_{foil} and ΔV_{mirror} [Sta82]

$$y = \frac{d}{2} \cdot \frac{\Delta V_{\text{foil}}}{\Delta V_{\text{mirror}}}$$

for the parabola amplitude and

$$x = 2d \cdot \frac{\Delta V_{\text{foil}}}{\Delta V_{\text{mirror}}}$$

for the shift alongside the mirror plane, with d being the distance between outer reflecting and inner shielding wiring of the reflecting module, as indicated in 3.4. In conclusion, the shift of the SE flight path along the ion beam axis from the entering point of the reflecting module to the exiting point can be written as

$$L_{\text{shift}} = \sqrt{2}d \cdot \frac{\Delta V_{\text{foil}}}{\Delta V_{\text{mirror}}}$$

These isochronous conditions apply to an idealised electrostatic system. Determining the timing resolution of the detector head without and with electrostatic mirror clearly shows a decrease in resolution for the latter [Sta82]. Especially for heavy ions the initial energetic distribution of the SE is not negligible in a realistic treatment, even when applying a high accelerating potential ΔV_{foil} of $3-4\,\text{keV}$ to minimise the effect [Šar96].

Thus, to get closer towards the desired isochronous flight path conditions, one has to probe the flight paths for a set of SE emitted from exactly the same point of the foil but having a distributed initial velocity $v_0(1 \pm \delta)$ with V_0 being the mean velocity. In a first order assumption the inner drift region is to be field free and the potential gradients of the foil and the mirror are to be homogeneous. Thereby one can divide the flightpath into three different regions: the path between foil and entrance of

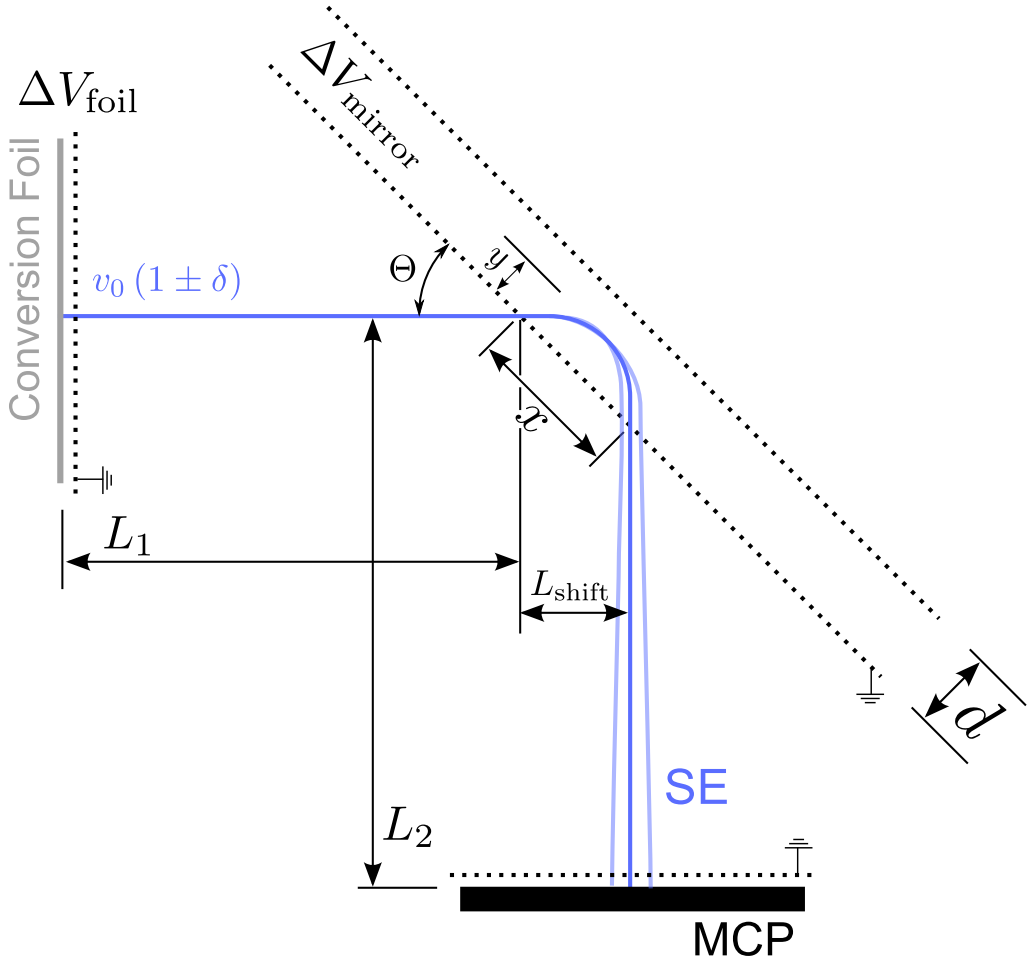

Figure 3.4.: Schematic flight paths of SE emitting from one point of the foil at a small angular distribution. The dotted lines represent the electrostatic wiring, whereas the inner triangular structure is at ground potential and thus defines the field free drift region. This figure is based on [Sta82, Nan05].

the mirror L_1, the path inside the mirror and the path from the mirror exit to the detector head L_2, as indicated partly in figure 3.4. L_1 is an exactly defined path for the complete set of SE, even though they will arrive at the mirror entrance at different times due to their energetic distribution. This will in turn lead to a different strength of deflection once they are inside the reflecting module and thus the set of SE will be spatially distributed concerning its exit point of the reflecting module. In addition to the limit in timing distribution the spatial resolution of the system is limited by this, as well.

Taking into account the above mentioned assumptions, one can express the TOF of the set of SE as a function of the geometry, the potentials and the initial energy [Nan05]

$$T = T_0 \left(\mp \frac{L_1 + L_2 - L_{\text{shift}}}{v_0} \pm \frac{2 m_e v_0 d \sin\Theta}{e \Delta V_{\text{mirror}}} \right) \delta$$

with m_e being the electron mass, e the elementary charge and the other variables as indicated in figure 3.4. Assuming $\Theta = 45°$ as justified by the assumptions, one can track down the isochronous conditions of the system by clearing out the braced term, which is given for

$$\frac{d}{L_1 + L_2} = 0.236 \cdot \frac{\Delta V_{\text{mirror}}}{\Delta V_{\text{foil}}}$$

These conditions are not achievable in reality, due to the finite components of the system and therewith field disturbances. Yet one can set the geometries and potentials as close as possible to reach the above mentioned condition. Such a calculation has been performed to estimate the dimensions for the mechanical design of a second detector prototype, as described in section 4.2.

3.3.2. Utilised wiring materials

Similar to the different foils used during the whole R&D phase of the detector, there have been different kind of wires and meshes investigated for the design of the electrostatic assembly. Beside having a high open area ratio, the wiring should have a certain physical strength. Due to an electric field gradient of $\Delta V_{\text{mirror}} \backsimeq [5 \ldots 7]\,\text{kV/cm}$ one needs to mount the wiring at a high physical tension, in order to avoid a possible curvature, especially with respect to the large area of the reflecting unit of minimum $\sqrt{200} \cdot 8\,\text{cm}^2$, which is defined by the overall active area mentioned in section 3.1 and the 45° tilt of the reflecting module. Furthermore, they should withstand this tension without losing their stiffness over time. Thus only certain kinds of available wires and meshes are suitable.

Phosphor Bronze Alloy Wires with a diameter of 0.125 mm have at first been used for the inner drift region. As described in section 4.1, one helical winding at ground potential was employed. The pitch was 0.7 mm, leading to an open area ratio of 80%.

Nickel Mesh A+B For the backside (in direction of the beam looking downstream) of the reflecting module, which is set to a certain voltage, a 99.9% nickel mesh (A) was first used. A very first mesh with a wire diameter of 0.041 mm at a pitch of 0.34 mm was lithographically made, having a thickness of 0.025 mm. From a mechanical point of view, this is favourable due to its tensile strength and the torsional stiffness. Unfortunately, this technique only allows meshes of the mentioned parameters, which equals only an 80% open area ratio.

A second mesh (B) of the same material, but of woven manufacturing, with 0.015 mm wire diameter at a pitch of 0.44 mm with a nearly 93% open area ratio was used alternatively to the lithographic nickel mesh.

Tungsten Mesh A+B Since the highly open nickel mesh could not be delivered anymore, there was need of a suitable replacement. Tungsten mesh was found to be available at similar open area ratios plus having the additional advantage of a higher tensile strength of up to 1920 MPa compared to nickel (up to 660 MPa [Goo13]. A tungsten mesh (A) of $0.0017'' \approxeq 0.0432$ mm wire diameter and a pitch of $0.0316'' \approxeq 0.80264$ mm, having a 90% open area ratio was used first. It is manufactured by Cleveland Wire Cloth & Manufacturing Company[4].

Later on, a similar woven tungsten mesh (B) with $0.0010'' \approxeq 0.0254$ mm wire diameter and a $0.024'' \approxeq 0.6096$ mm was chosen to be the finally used type of mesh, especially due to the combination of high open area ratio of 92% and the material. It is manufactured by Unique Wire Weaving[5].

Stainless Steel Mesh Another material being used was a 316 stainless steel mesh by TWP Incorporated[6]. It has a 0.03 mm wire diameter at 0.46 mm pitch, resulting in an 88% open area ratio. Even though it is not as good as tungsten mesh concerning the handling or construction and the open area ratio, it is relatively inexpensive and thus well suited for early prototyping and testing.

3.4. Detector Head

The detector head itself basically consists of two components. On the one hand, the MCP stack to multiply the SE and, on the other hand, the DDL, which functions as a position sensitive readout of the MCP. This construction itself is shielded by a grounded mesh towards the electrostatic top-assembly, contributing to the inner field free drift region.

[4]Cleveland Wire Cloth & Manufacturing Company, 3573 E. 78th St., Cleveland, OH, 44105-1596 USA
[5]Unique Wire Weaving Company, 762 Ramsey Ave, Hillside, NJ, 07205 USA
[6]TWP Inc., 2831 Tenth Street, Berkeley, CA, 94710 USA

3.4.1. MCP

General remarks

An MCP is in principal an up to a few millimetre thick, planar array of photo multiplier tubes functioning as a high gain, secondary emission current amplifier. It consists of millions of parallel, hollow semi-conducting cylinders made out of glass. Each of the cylinders is an individual secondary electron emitter (not to be confused with the SE from the conversion module). The front and back surface of an MCP is metallised and a bias voltage in the order of few kilo Volts introduces an accelerating field within the channels. If a particle or photon hits the channel wall, it will knock out electrons which are accelerated. These electrons will then knock out further electrons when hitting the channel wall and so forth. To increase the possibility of electrons hitting the channel wall, all channels have a certain bias angle to the surface normal. Since it is running in a saturation mode, as described below, it is not suitable for calorimetric measurements.

The most common material is high resistance lead silicate glass, which has the negative effect of being very hygroscopic and quite brittle. Especially the latter limits the size of an MCP. Since it is moreover rather expensive, other materials like anodic aluminium oxide, silicon or polymethylmethacrylate[7] are under investigation [Dro06]. For the production, hollow fibres are filled with size-matched ceramic fibres. Several of those are stacked to hexagonal packages, which are melted together under pressure. These hexagonal blocks are used to build an MCP blank of the desired shape. This block is then cut into thin slices and the inner ceramic fibre is being etched away, while the lead silicate glass is left over with according channels [Was71]. After the metallisation, typical resistances range from some tenth to some hundreds of mega Ohms, depending on the exact configuration of the MCP.

This basic MCP is metallised on both sides, while the inner cylindrical hollows remain uncoated. Depending on the application, the coating can vary. For the detection of UV-photons in the range of $200-2000$ Å caesium iodide (CsI), copper iodide (CuI) or magnesium fluoride (MgF_2) are common materials. For soft X-rays in the order of $0.2-9$ keV potassium bromide (KBr) is the coating of choice. Most used coatings are sensitive to the detection of electrons and are made of magnesium oxide (MgO), silver (Ag), copper (Cu), nickel (Ni) or nickel chromium (NiCr) [Bur05].

Yield and stacking

Concerning the characterisation, the length to diameter ratio of the channels $\alpha = L/d$ is a major parameter. It is a distinguished measure for the overall gain of electrons $G = \delta^n$, which is basically defined as a function of the gain per amplification stage δ, i.e. collision with the channel walls, and the amount of stages n. In detail, the gain has found to be [Wiz79]:

[7] better known under the registered trademark Lucite

$$G = \left(\frac{AV}{2\alpha\sqrt{V_0}} \right)^{\frac{4V_o\alpha^2}{V}}$$

with V_0 being the initial energy of a released electron, typically in the order of few electron volts, and $A = \delta/\sqrt{V_c} \simeq 0.2$ being a proportionality constant. V_c is the collision energy of the electrons (with $q_e = 1$), making $V = V_c - V_0$ the applied bias voltage. G itself develops a maximum, since δ increases with increasing V up to a point, where the decreasing in n overcompensates this trend. A similar trend is given with increasing α, i.e. the higher the ratio, the higher the gain. After reaching a peak value, the gain will decrease, again due to the decreasing n. Typically, α ranges roughly between 40 and 80.

If the gain is high enough, space charge densities will take effect at the back side of an MCP, forcing a dynamic equilibrium and therewith a saturation of the gain [Sch66]. If the space charge distribution is too high, V_c decreases due to screening effects of the electrons interacting with the space charge, and so does δ, which results in a decrease of the space charge. On the other hand, if the space charge density is too low, V_c increases together with δ, resulting in an increase of the space charge. This dynamic equilibrium and saturation causes the pulse height distribution of the MCP, which plots the number of counts as a function of the output pulse height.

While the pulse height distribution is more or less a falling exponential for an unsaturated single MCP, it becomes a fairly Gaussian shape for a saturated one. The same is true for a stack of N single MCP, as described later. However, a falling exponential part in the lower pulse height regime still remains. Figure 3.5 shows typical pulse height distributions for various configurations. The pulse height distribution and its FWHM of the Gaussian fit, known as the pulse height resolution expressed in percentage with respect to the mean, is a typical measure for the performance rating of a MCP. In order to drive the MCP in a stable mode, the bias voltage as only variable parameter during operation has to be chosen in a way, that the MCP saturates within the dynamic range. For higher values of α, the mean of the pulse height distribution is lower than for smaller α values, i.e. the signal to noise ratio increases with decreasing α values.

Another effect limiting the performance is the so called ion feedback. For high charge densities, the probability of an interaction between an electron and a residual gas molecule increases. These molecules are typically absorbed by the channel walls, wherefrom they can be emitted. The interactions result in positive ions, which traverse in the opposite direction of the electrons alongside the channel gaining energy and hitting the channel walls. This results in ghost signals after the true signal. That is the main reason beside the high voltages, why an MCP should not be operated at pressures above roughly $5 \cdot 10^{-6}$ mbar. An additional solution is the curving of the channel in a way that the positive ions will hit the wall before gaining enough energy to induce additional electrons [Eva65].

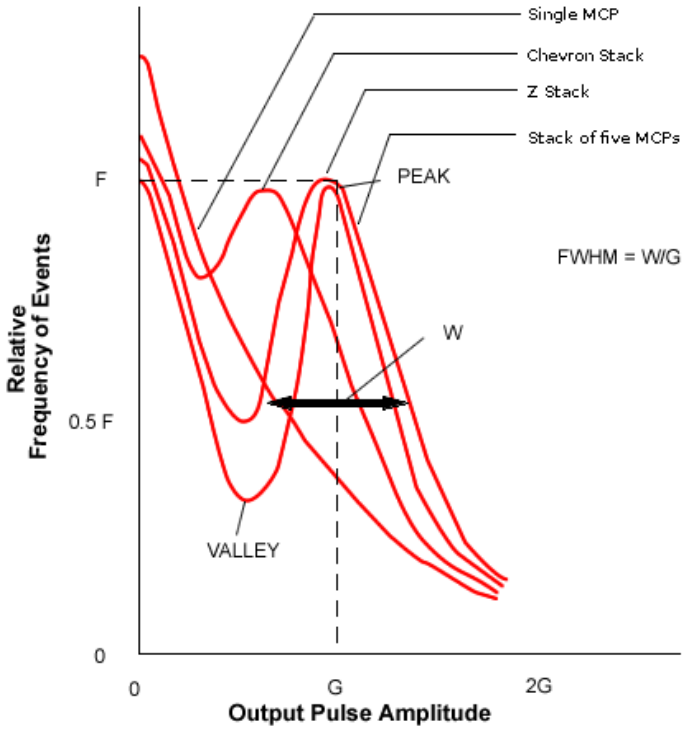

Figure 3.5.: Schematics of the pulse height distribution for different MCP stacks, taken from [Pho13]. Note that the curve of the single MCP represents a non saturated MCP.

Figure 3.6.: Schematics of different MCP stacks. Note the alternating bias angle of each MCP.

A drawback of this solution is that the curving of the channels in a desired strength is mechanically hard to achieve for an only circa one millimetre thick MCP. An effective and simple solution is a stacking of two or three single MCPs [Col73]. In both cases the stacking should be done in a way that the bias angle of the straight channels of one MCP is contrary to the other MCP. For a stack of two, one speaks about a so-called *Chevron Stack* and for a stack of three, one speaks about a *Z stack* with respect to the alternating bias angles, as one can see schematically in figure 3.6.

Of course, the stacking enhances the overall gain compared to a single MCP. The mean of the Gaussian pulse height distribution shifts to higher pulse shapes for Z Stacks then for Chevron Stacks, i.e. the mean gain increases. On the other hand, the dark current and therewith noise of the system is increased as well. Therefore one should choose a good trade off between overall gain, signal to noise ratio and ion feedback suppression. Table 3.1 summarises typical rule of thumb parameters for standard MCP configurations. The probably most common configuration is a Chevron-Stack with a fairly high α value, since it comprises the optimum solution of all parameters. For convinience, the future discussion assumes the use of a Chevron Stack.

Table 3.1.: Typical parameters of standard purchase MCP configurations by [Bur05]. The pulse height is given in relative amplitudes with respect to a single MCP negative signal pulse.

Configuration	**L/D Ratio α**	**Maximum Voltage [V]**	**Gain**	**Pulse Height**
Single MCP	40:1	1000	$> 4 \cdot 10^3$	Neg. Exp.
	60:1	1200	$> 1 \cdot 10^4$	Neg. Exp.
Chevron Stack	40:1	2000	$> 4 \cdot 10^6$	$< 175\%$
	60:1	2400	$> 1 \cdot 10^7$	$< 100\%$
Z Stack	40:1	3000	$> 3 \cdot 10^7$	$< 120\%$
	60:1	3600	$> 2 \cdot 10^8$	$< 60\%$

Limiting aspects for the timing and spatial resolution

Concerning the gain and the pulse height resolution of a Chevron stack a high α value is important. Additionally the dynamic range, i.e. range of stable operation, increases. This effect is due to the lower overall resistance, which is introduced by higher channel densities, i.e. smaller channels with a higher α value. In principle, a high α value favours the timing, as well as the spatial resolution. Unfortunately, there are several drawbacks to this.

Firstly, the manufacturing process allows only channel diameters down to 4 µm for a small size MCP. The larger the active area gets, the larger the channel diameter has to be. The second issue is a too small resistance. The read out signal of the MCP

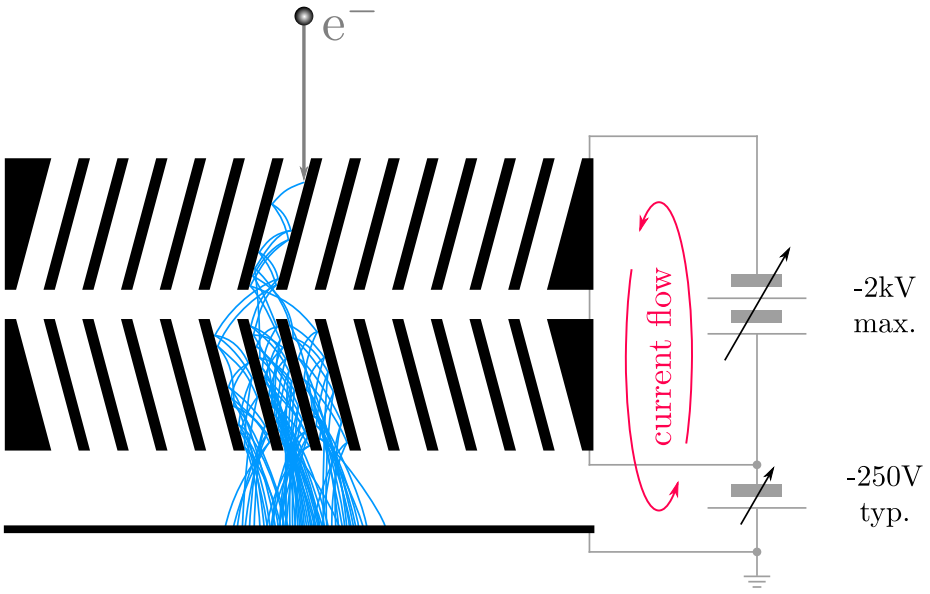

Figure 3.7.: Schematic electron cascade of a Chevron Stack MCP following after an incident single electron. Indicated in blue are the trajectories of multiple order electrons. A typical voltage supply (without signal decoupling) is indicated in light grey, as well as the current flow, which is indicated in red. As one can see, the avalanche spreads over several channels in the second MCP. Note that the incident electron must overcome at least the applied negative potential on the front side of the Chevron Stack.

when being hit is a current. The emitted electrons are captured by a readout anode placed behind the MCP and being returned by the voltage supply. If the resistance R is too low, the current flow becomes quite high and accounts for a Joules heating of the MCP by $P = V^2/R$, which in turn can change the overall response of it or in worst case lead to a destructive thermal runaway [Mri08]. Attempts to cool an MCP have been made, yet without remarkable results [Tre96]. A third shortcoming is a worse signal to noise ratio. Since the whole detector should be used as a stand alone unit in a slowed down beam setup as described in section 1.3, there are no additional triggers like a dE detector. Hence a certain signal to noise ratio and therewith a not too high α value is required in order to discriminate true events from noise.

Assuming an ideal position sensitive anode, the spatial resolution itself is in first order only dependent on the channel diameter as smallest possible entity. However, the avalanche of higher order electrons emit in a cone from the backside of the MCP. As seen in figure 3.7, this causes a broadening of the avalanche, especially if using a Chevron or Z Stack. Thus multiple channels fire, even if only one was hit in first instance. There are two solutions to narrow the avalanche spread.

One attempt is to minimise the gap between both MCPs. If the gap is large, more channels of the second MCP will be hit by the electron avalanche from the first MCP,

which will result in an overall higher gain for the price of a worse spatial resolution. If the gap is small, less channels will be hit in the second MCP and therewith the spatial resolution will increase at the price of a lower overall gain. One aspect not discussed so far is the impedance of a MCP. Of course, both MCPs in a Chevron stack should be impedance matched in order to achieve a homogeneous potential distribution along the channels. When the impedances differ, one can use an appropriate resistance to bypass the gap. If both MCP have the same impedance they can be put on top of each other, erasing the gap for the best possible solution for this issue.

Another attempt is to extend the backside metallisation of the MCP into the channel walls, so-called end spoiling. Thus higher order electrons can be absorbed instead of multiplied in the vicinity of the channel exit, minimising the opening angle of the electron spill geometrically. The gain is decreasing with a deeper coating of the channel exits [Rug72, Pri01, Wu08]. Another simulation showed that the electrons bypassing the spoiling can be deflected towards the channel centre, resulting in a narrowing of the electron spill and a thereby slightly improved spatial resolution [Hoe01].

The timing resolution is in first order dependent on the size of the MCP itself and again on the α value. Both influence the recovery of the MCP after it has fired. As said before, the major signal is a current flow, which is inherently fast, resulting in a short rise time of the rising edge of the signal. Assuming two equally mounted MCP of equal thickness and size, the timing signal varies only with different channel diameters, i.e. α values. Such a comparison has been made for 6 µm and 12 µm diameters [Mat85]. Two different representative pulses can be seen in figure 3.8. Table 3.2 shows that the mean transit time and the rise time increase with a decreasing α value while the fall times are of the same order. The transit time spread itself is the major intrinsic limit for the timing resolution of a MCP.

Table 3.2.: Signal parameters corresponding to figure 3.8.

	Channel Diameter	
	6 µm	12 µm
Rise Time [ps]	167	245
Fall Time [ps]	721	716
Transit Time [ps]	406	650
Transit Time Spread [ps]	67	81

In general one can say that the larger the active area of an MCP is, the larger the discussed times get. Especially since larger MCP can only be produced with lower α values, it is a challenging task to enlarge the detector head while keeping the timing resolution constant. Attempts to build a very large eight inch diameter MCP based photon detector investigate a segmentation of the anode or a well defined contacting of the MCP. Thus one can correct for the different physical transit lengths for different hit points on the MCP surface [LC13], e.g. it makes a difference in the

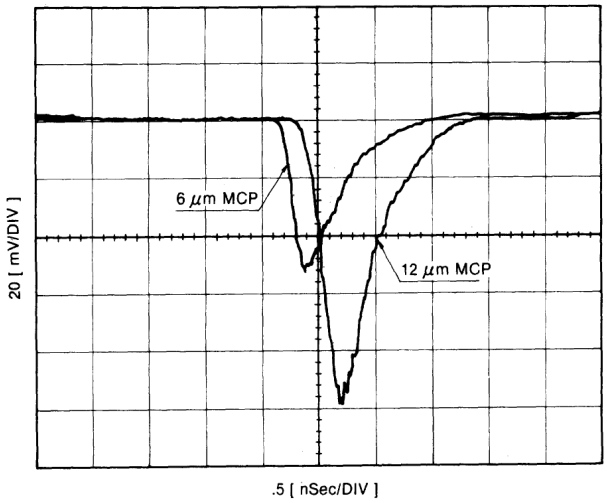

Figure 3.8.: Timing signals for equally thick and large MCPs with 6 μm and 12 μm channel diameters, taken from [Mat85]. The corresponding signal parameters can be seen in table 3.2.

recovery process if an MCP is hit centrally or near its outer border, especially with respect to the contacting point.

Life time of a MCP

The life time of an MCP is limited mainly due to electron scrubbing of the channel surfaces, which leads to a change in the channel walls' chemical composition [Pra93]. Therewith the secondary emission coefficient changes, resulting in a decrease of the gain. In principle, the degradation process is a function of accumulated counts [Wiz79]. A rule of thumb for a standard Chevron Stack is that the overall gain decreases tremendously after roughly one Coulomb of accumulated electrons have been spilt per channel. This means especially, that if a MCP is hit only centrally by heavy ions or a vast amount of electrons, the MCP will degrade very fast in the centre, while still being nearly fully functional close to the borders [Jag]. In one of the prototype units it has been observed that, if the MCP is degraded far enough, one still gets a timing signal, but the gain decreased in a way that no useful signal is measured by the DDL. Thus the tracking will not work, as one measures only a homogeneous hit pattern of the MCP, i.e. only the noise of the DDL without any superposing hit pattern signal.

Utilised MCP

At the time of the initial project phase, two different kinds of MCP were up for debate. A *Del Mar Photonics*[8] *Type 70*90* and a *Hamamatsu Type F2396-04*. Very first tests have been performed with the Del Mar MCP having an $70 \cdot 90\,\mathrm{mm}^2$ outer size with an active area of $66 \cdot 86\,\mathrm{mm}^2$. Its channel diameter of 15 µm at 0.8 mm thickness and 8 deg bias angle results in $\alpha \approx 53$. Unfortunately, this MCP did not perform as expected and thus a decision in favour of Hamamatsu was made, as anticipated in section 3.1.

The outer size is $96.9 \cdot 78.9\,\mathrm{mm}^2$ with an active area of $90 \cdot 72\,\mathrm{mm}^2$. A picture of a mounted chevron stack can be seen in appendix A.3(b). The channel diameter is rather large with 25 µm, though at 1 mm thickness and 8 deg bias angle its alpha value is at the lower limit with $\alpha \approx 40$. As discussed before, this is not necessarily the desired configuration concerning the performance. Beside, there were no other available MCP of comparable sizes with larger α values at the time of purchase. It showed to be a good idea for early prototyping to stay on the safe side when it came to the operation of the MCP. Early problems have been a comparably worse vacuum system, even if the degassing of the MCP is faster at higher channel diameters, for example.

3.4.2. DDL

Different approaches to position sensitive anodes

Since the MCP only functions as continuous current amplifier, the spatial information has to be obtained from the read out anode. For standard timing measurements one typically uses a coaxial anode, which is directly impedance matched to 50 Ω. Other advantages are the elimination of pulse reflections and ringing of the pulse [Gou75, Wiz79]. Unfortunately, the spatial information gets lost.

In order to retain the spatial information, the anode has to be segmented somehow that it can account for the local charge cloud distribution emitted from the MCP. In general, there are two ways to achieve this. One solution is the usage of anode patterns and the other approach is the usage delay line anodes. The basic functionality of the latter is based on the effect that the charge cloud from the MCP picked up by the anode needs a certain time to propagate from the hit point alongside a delay line to its signal pick-up. Taking the MCP timing signal as start and the anode signal as stop, the measured time corresponds to this hit point. Of course, the design is very crucial and different kinds were evolved, which will be discussed shortly.

Pixel anode A pixel anode is simply a planar metal anode plate divided into independent pixels of the desired size, as shown schematically in figure 3.9(a). A significant disadvantage is the accompanying number of read out channels and thus back-end electronics, i.e. one complete data acquisition channel per pixel. Since even nowadays this involves a huge financial and computational effort, it

[8] Del Mar Photonics Inc., 4119 Twilight Ridge, San Diego, CA, 92130 USA

never evolved. A new approach are electron bombardment CCD (ebCCD) chips with superior spatial resolution, which consist of an MCP with a directly back-thinned, optically glued CCD chip [Hai03]. Therewith one could do without the complete detector head (stand alone MCP plus read out anode) and use the ebCCD directly as such. Most ebCCD chips available are rather small and only sensitive to photons.

One could use a phosphor screen back-thinned to the MCP and detect the fluorescence directly with a standard CCD chip, eventually after being guided by some optical system. This would require a tremendous mechanical effort, especially since the fluorescence photons would trigger the MCP again. Furthermore, the timing resolution in the order of several micro seconds of such chips is not sufficient. As there are similar powerful anodes at lower complexity, such systems have never been used.

Cross strip anode In order to reduce the amount of channels, a multi-layer, so-called cross strip anode, can be used. A schematical drawing is seen in figure 3.9(b). It functions similar to a double sided silicon strip detector [Sel92], even though only the front side is active. A cross strip anode consists of two perpendicular layers of parallel strips, whereas the two layers and each strip are isolated and can be read out independently. The result is a row and column hit pattern. If a current is measured in a horizontal and a vertical strip, the crossing point of these strips is the pixel being hit. Unfortunately, only the front layer is fully visible to the charge cloud emitted by the MCP. The gap of the front layer strips has to be chosen in a way that the underlying, perpendicular strips are visible. Therewith the second layer is partly shielded by the front layer strips. Hence, a certain dead area is inevitable and a proper strip width to strip gap ratio must be chosen in order to gain a high sensitivity at a high spatial resolution.

The electronics must integrate the collected charge of each strip to determine the centroid of the charge cloud by $(\sum_n Q_n)/(\sum Q_n)$ with n being the strip number and Q the collected charge [Sie03].

Split strip anode In order to get similar results with only four channels, a single layer split strip anode can be used, as shown schematically in figure 3.9(c). It is based on various wedge-shaped design patterns [Mar81]. Its major advantage is that by a logical combination of the patterns, different spatial information can be obtained. If pattern $(A+D)$ and $(B+C)$ are combined the X axis can be read out (where the X axis equals the horizontal axis in figure 3.9), while a combination of $(A+B)$ and $(C+D)$ reads out the perpendicular Y axis. The centroids given by $(Q_A+Q_D)/\sum Q_{[A,B,C,D]}$ and $(Q_C+Q_D)/\sum Q_{[A,B,C,D]}$ result in a typical curve if plotted against each other, which in turn can be used to filter out true events [Edg89].

Single delay line or wedge anode While the early design of so called wedge and

strip anodes did not use a delay line [Mar81], this anode design combines both approaches of a pattern and a delay line anode. It is a single layer, planar anode. A typical one can be seen in figure 3.9(d). It has four contacts, where two belong to independent wedge patterns and the other two to each end of a zig-zag shaped delay line. For the vertical Y axis the centroid of the collected charges is given only by the two wedges W_1 and W_2. It is calculated by the before mentioned charge division $Q_1/(Q_1+Q_2)$. For the horizontal X axis, on the other hand, only the delay line is read out and the centroid is given by $(T+T_d)\cdot V_S/2$. Here, V_S is the signal propagation velocity within the delay line, T is the measured difference in arrival times on the two ends of the delay line and T_d is the overall travel time a signal needs from one end to another. The latter is a physically given constant and one of the two ends must be delayed by this value. Another option is the termination of one end of the delay line to avoid reflections and to read out only the other end. Thus one read out channel and the additional delay T_d are not needed for the price of a larger range for T and a practically worse precision [Lam87, Sie91].

Cross strip delay line anode This multi-layer anode is basically a cross strip anode, where each layer of strips is read out by a single delay line. The parallel strips are serial connected to the delay line, as one can see in figure 3.9(e). An advantage, besides the reduction of down to two read-out channels by terminating one end of each delay line, is the relatively high count-rate capability of such anodes [Val00]. Early designs used a multi-layer attempt without insulating material in between the conducting layers, i.e. a three dimensional construction of wires with a reflecting plate [Kel87]. Newer lithographic-based attempts try to minimise the dead area by a design with diamond shaped patterns in between the horizontal and vertical strip crossings [Jag02b].

Serpentine delay line anode This type of multilayer anode is a pure delay line design. As seen in figure 3.9(f), two single delay lines are placed perpendicular on each other, while each delay line is shaped like a serpentine. The read-out principle is similar as described before, i.e. two or four channels are read out. It shares the disadvantage of dead areas, like the cross strip anode. An advantage on the other hand is the possibility to easily match desired impedances and its mechanical robustness [Fri96].

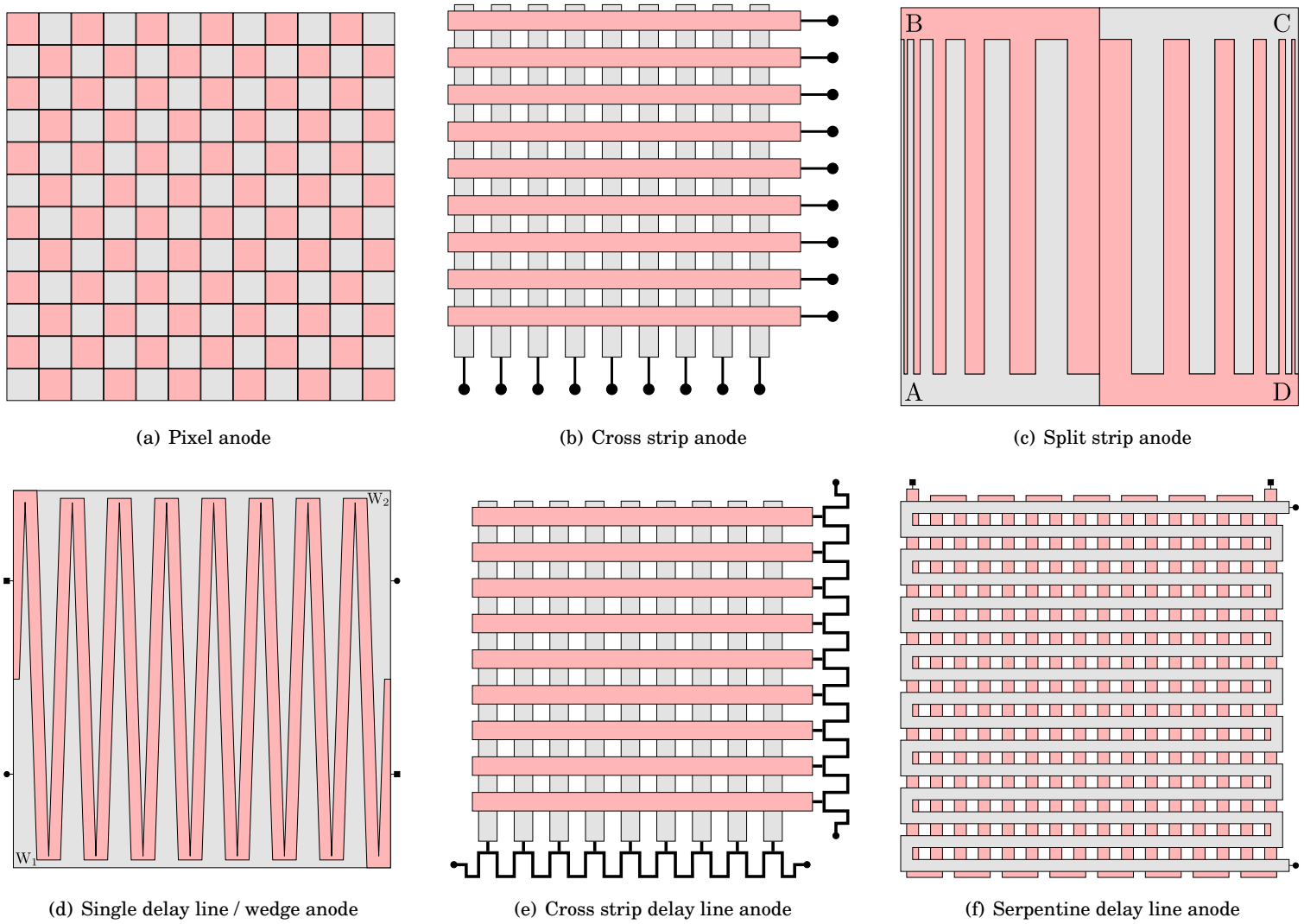

(a) Pixel anode (b) Cross strip anode (c) Split strip anode

(d) Single delay line / wedge anode (e) Cross strip delay line anode (f) Serpentine delay line anode

Figure 3.9.: Common position sensitive anodes. The upper row shows pattern anodes, while the lower row shows combinations of pattern and delay line anodes. Only figure 3.9(f) shows a pure delay line anode.

Helical dual delay line anode

One problem arising from pattern and monolithic planar anodes is their capacitance, which increases with increasing size and limits the resolution of the anode. Beside this, most of these designs need specialised lithographic manufacturing processes. To avoid this, a simple yet very powerful anode is the helical delay line anode. A metal plate is fixed in isolating braces at the corners. Around these a wire is wound from one corner to the other one alongside the plate, both for the X axis and the Y axis. Note that one pair of opposing braces should have a lower height than the other pair in order to separate both layers of windings from each other. In this way one gets two delay lines as seen in figure 3.10(a), where the red winding represents the x-axis delay line and the black one the y-axis delay line respectively.

One disadvantage of such a design is the capacitive coupling of the parallel wires which might lead to an induction of false signals. To avoid this effect, a second delay line per axis, wound midway between the turns of the existing delay line can be used. A schematical drawing can be seen in figure 3.10(b). Typical pitch distances are in the order of $0.5 - 1$ mm. For each dual delay line, one of the wires acts as reference and the other one as charge collection wire, being read out by a differential amplifier or a signal transformer. Thereby the charge collecting wire should have a more attractive potential than the reference one. The potentials of both pairs are chosen in a way that the charge cloud emitted from the MCP is split into equal parts among both delay lines, i.e. their collecting wire. If a current flow propagates along a collecting wire, it will induce a current only in the neighbouring reference wire and thereby registered by the differential amplifier. The central anode acts as reflecting plate, so that nearly all electrons from the charge cloud can be collected. It turned out to be useful to add a certain gap between the MCP and the DDL to allow the charge cloud to spread over several coils of each DDL and thus interpolating between them. In this way a more precise centroid for each axis can be obtained [Sob88, Wil89, Wil91].

Again, either both ends of each delay line can be read out or one has to read out only one end and terminate the other one to avoid reflections. Of course, the return path of each wire on the backside not facing the MCP is somehow a passive area enlarging the propagation time of the signal. If one wants to detect event by event, there should be no two events within the maximum propagation time (from one end to the other of each delay line) in the worst case. Typical values for helical dual delay lines in a desired size are in the order of below 100 ns, which would result roughly in a maximum possible rate of 10 MHz. Those rates will not be achieved even rudimentarily at modern RIB facilities and thus this effect can be neglected. This design has been developed even further to hexagonal, helical dual delay lines being suitable for multi-hit read out [Jag02a].

Used Materials

The first DDL used were built by the in house mechanical workshop of the IKP (*Institut für Kernphysik*). It was made from a 0.1 mm diameter copper wire, helical wound

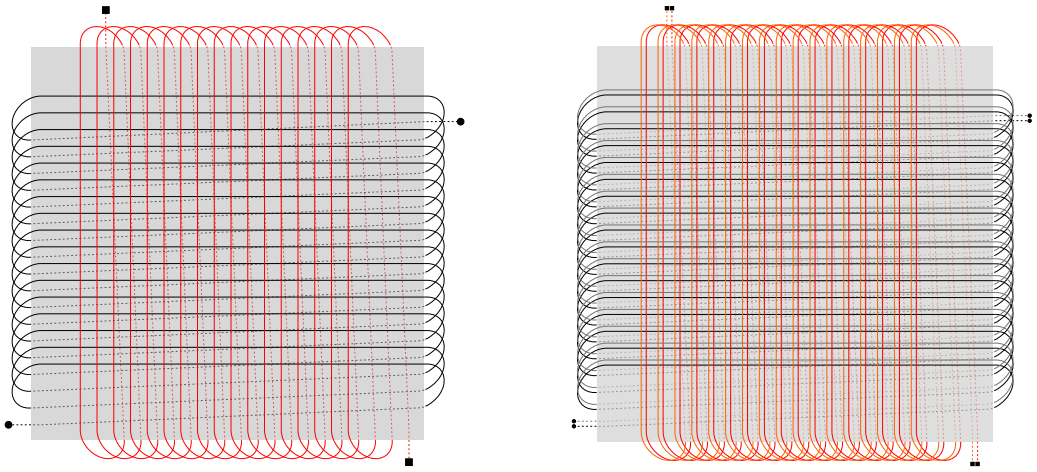

(a) Helical delay line anode.

(b) Helical dual delay line anode.

Figure 3.10.: The left figure shows the schematics of a helical, single delay line anode, while the right figure shows a helical dual delay line anode. For both version wires are wound around a reflecting plate. Note that for illustrating reasons there are no isolating braces drawn at the bends.

around a 1 mm thick stainless steel plate with a 0.5 mm centre to centre pitch. For the isolating braces grooved, round POM[9] bars were used. The distance between the reflecting plate and the inner wire layer was 1.5 mm and 2.5 mm for the outer wire layer. The impedance Z_{DDL} of each DDL was circa 130 Ω.

The area of the DDL was chosen to fit once the Del Mar Photonics MCP and once the Hamamatsu MCP. For the former the end to end signal propagation times are roughly 48 ns and 54 ns for an edge length of 67 mm and 86 mm respectively. For the larger, finally chosen Hamamatsu MCP the values are 60 ns and 68 ns for an edge length of 80 mm and 100 mm respectively. A second revision used gold coated copper wires and reflecting plates. Pictures of two revisions of a DDL can be seen in appendix A.4.

Ageing effects

After nearly one year of continuous operation the DDL of the second unit gave false results. In between both units a multi-hole mask was placed, which can be seen schematically in figure 3.11. Since the master trigger was a timing signal in both units, the mask should have appeared as hit pattern in both units as well. Of course, the projection is larger in the second unit than in the first one with respect to a point-like source in front of unit one. Therefore the typical schematics of the mask should become visible. For unit one this was the case, whereas for unit two some structure was missing, as can be seen in figure 3.12. After figuring out it to be a mechanical

[9] Polyoxymethylene

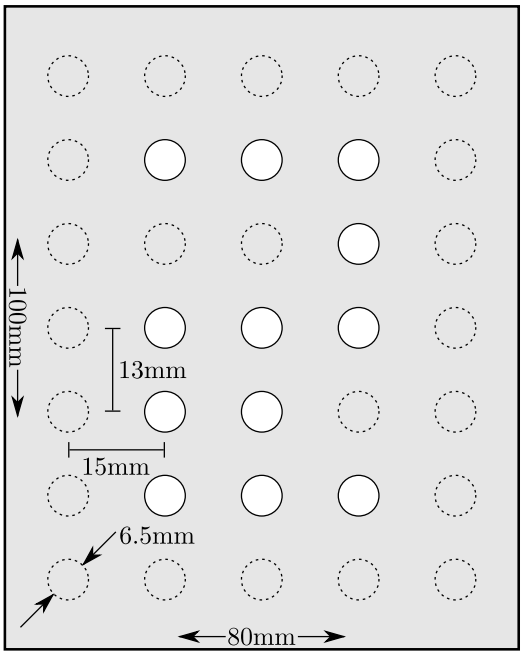

Figure 3.11.: Schematical drawing of a multi-hole mask used in various tests. The dotted circles are taped holes and only the white, inner circles are open holes. In this configuration the orientation of the measured projections could be clearly indicated. Depending on the purpose, the mask could be modified.

problem, the detector was dismantled and a defect on the DDL of the second unit was found. Visible to the naked eye a change in the surface texture of the wires and the reflecting plate could be observed, as seen in picture A.4(a).

Since the affected spot corresponded to the observed structure in the hit pattern, the only logical explanation was that some sputter-like or electron scrubbing effects took place. They must have changed the wire surface in a way that no electrons could be collected any more, but in the inner core of the wire the signal could still propagate. Otherwise the whole DDL should not have shown any hit pattern. The reflecting plate and the wires of the renewed DDL were coated with a thin gold layer, in order to reduce the chance of such an effect in future use. This final DDL can be seen in picture A.4(b). After nearly two years of operation, such a degrading effect could no longer be observed.

3.4.3. Complete detector head

Both the MCP and the DDL built the detector head. In order to keep the whole system fairly modular, each sub unit can be changed or modified individually. For this purpose a basic plate of a few millimetres thick aluminium has been equipped with small rods. The DDL, as well as the MCP stack are mounted in a printed circuit board (PCB) frame made of FR-4 grade glass-reinforced epoxy laminate. For the dis-

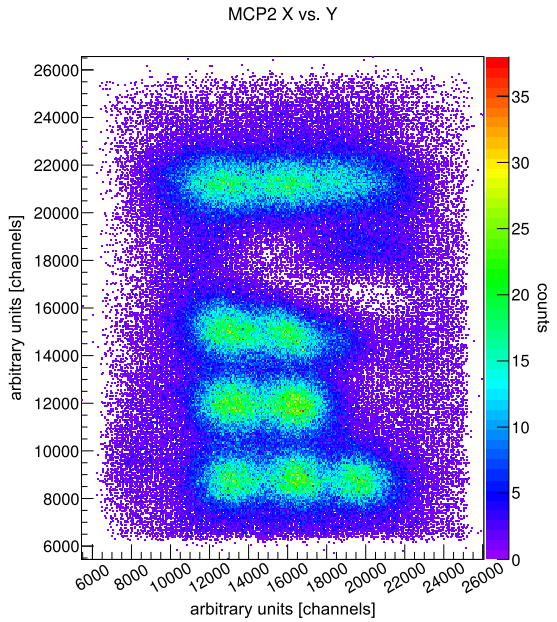

(a) Multi-hole mask hit pattern of the second unit with broken DDL.

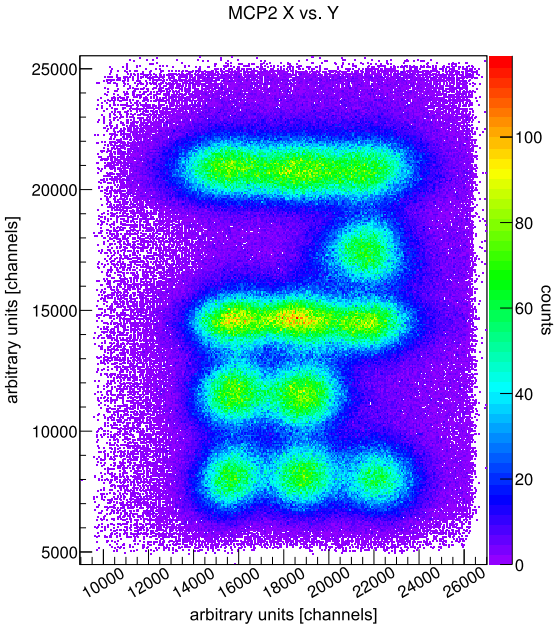

(b) Multi-hole mask hit pattern of the second unit with renewed DDL.

Figure 3.12.: Hit pattern of the second unit with a multi-hole mask in front of the conversion foil. Even though the absolute number of counts is higher in figure 3.12(b), one can clearly see the difference in the upper right area due to a broken DDL. The Z axis shows absolute counts, while the X and Y axis are labelled by arbitrary channel numbers.

tance between both MCP of the Chevron Stack a shim rectangle with a thickness of 0.57 mm was chosen.

The alignment and the mounting holes of the sub units are matched, thus they can be stacked upon the mounting rods. For isolation, a ceramic or POM clad is used in between the rods and the mounting holes of the sub units. In this way the distance between the MCP and the DDL can be varied. After first tests a distance of 6.285 mm between the backside of the MCP stack and the front side of the reflecting plate was chosen.

Afterwards the complete detector head was fixed with small arresting cylinders, fixed to the mounting rods by small M2 screws. A picture of the final detector head can be seen in appendix A.3(b).

3.5. DAQ-System

3.5.1. Basic system

The raw signals from both detector heads are read out by front end electronics, which are discussed in detail in section 4. Their output signals in turn are processed by data acquisition (DAQ) electronics. This DAQ is basically made up from standard NIM electronics and CAMAC based analog to digital converters (ADCs). The latter are read out by the CAMAC bus via a PC, which writes the raw data in a so called-list mode format.

As seen in figure 3.13, a minimum of five channels is used. One for the timing of both MCPs and one each for the X and Y axis of the DDL. The latter counted twice with respect to the two detector units. Hence for the read out of the DDL one end of each axis is terminated in order to reduce the amount of channels and therewith minimise the needed electronics. In a first stage, similar to a fast timing branch of a standard nuclear spectroscopy experiment, every channel is amplified by a fast timing amplifier (FTA) and afterwards the signal is shaped in a constant fraction discriminator (CFD). This is necessary since the read out of the DDL is done by means of timing measurements.

The advantage of a constant fraction over a leading edge discriminator (LED) is its ability to generate a more precise timing signal, while the LED will give a timing signal, which is dependent on the amplitude of the input signal. Assuming two signals having the same rise time, but differing amplitude, an LED will trigger if a set amplitude threshold is crossed. With respect to different amplitudes, this will lead to different trigger times and thus output signals, known as time walk. A CFD instead delays the input signal by a certain amount and subtracts a (constant) fraction of the undelayed signal from it, resulting in a bipolar pulse whose zero crossing is less dependent on the amplitude. If this constant fraction is chosen properly, the time walk and therewith the respectively improved resolution can be minimised [Ré11].

Afterwards the time differences of the occurrence of the signals are measured by time to amplitude converters (TACs). For the spatial information, the MCP signals are used as start signal for the corresponding DDL channels. The latter are used as

stop signals, after being delayed to fit the dynamic range of the TACs. For the timing, the MCP signal of unit one functions as start and the signal of unit two as stop after being delayed. If necessary, the signals can be split by FAN IN/OUT modules. As additional hardware trigger, a gating signal of an auxiliary detector system can be used as so-called external strobe for the TACs. This means that the TACs will keep the information from a certain amount of time on hold before a strobe signal might occur. If it occurs, the TACs will fire, if not, the kept information will be rejected.

Following the fast analog electronics, the TAC signals have to be digitised. The digitisers are then read out by a PC and the processed data is written in a list mode file. This implies a set of information per event, which are the measured values in addition to a global time stamp. Afterwards this time stamp can be used to sort and further process the data, like demanding coincidence conditions and so forth.

3.5.2. Utilised electronic modules

The front-end electronics and high voltage supplies are described in sections 4.2 and 4.1. For the basic DAQ system, the following electronic modules were used:

Fast Timing Amplifier In a first testing setup, fixed gain quad-channel FTAs model *Ortec A3G12* were used. Afterwards, two quad-channel FTAs model *Ortec 9309-4* with adjustable gain from zero to 10 and a rise time of lower than 1.5 ns were used. It provides two outputs per channel and thus reduces the number of required FAN IN/OUT channels [Ort13].

Constant Fraction Discriminator Again, two versions were used. For early testing single channel CFDs model *Ortec 584*[10] were used, which were replaced by two quad-channel 200 MHz CFDs model *Ortec 935*. Its major advantage is a low walk below 50 ps for a wide dynamic range. It is especially designed to handle ultra fast timing signals below 1 ns FWHM, as is the case for MCP signals. Its three output channels further reduce the amount of FAN IN/OUT channels [Ort13].

FAN IN/OUT The signals were split by either FAN IN/OUT modules model *Surface Concept Logic Fan*[11] with an output jitter below 14 ps [Sur13] or model *LeCroy 428F*. The former for the fast MCP signals and the latter for the DDL signals and the external strobe, if applicable.

Delays For the delay, analog cable delay boxes model *Phillips Scientific 792* were used. Sometimes they were complemented by specially produced and calibrated, single delay cables. The modules were mostly connected by LEMO-type cables with 2 ns delay.

[10] AMETEK GmbH, ORTEC Division, Rudolf-Diesel-Straße 16, 40670 Meerbusch
[11] Surface Concept GmbH, Am Sägewerk 23a, 55124 Mainz, Germany

Time to Amplitude Converters In addition to two TACs model *Tennelec TC 862*[12] during early testing, TACs model *Ortec 566* have been used. Both have a timing resolution of $0.01\,\% + 5\,\mathrm{ps}$ at comparable non-linearities [Ort13, Oxf]. In the latest version, only Ortec TACs are used, since Tennelec is out of business.

Analog to Digital Converters To digitise the TAC signals, a CAMAC crate was equipped with ADC modules *XiA DGF-4C*. The used revision F of these ADCs provides four channels per unit, each with 80 MHz sampling rate at 14 bit resolution. For each channel, the input gain can be matched as well [XiA13]. The digitised signals can be pre-processed by different filter algorithms in FPGA and DSP chips. Since all ADCs share a common clock and can be read out by USB and the common CAMAC bus, list mode data can be provided. It is crucial that all TAC signals occur simultaneously at the ADCs. Therefore the cables between TAC and ADC should be of equal length. Smaller differences can be adjusted by internal TAC delays.

Optionally, a Time-To-Digital converter model *SurfaceConcept TDC type 03-06-27* [Sur13] has been investigated within a master thesis. The aim was to substitute the TAC and ADC branch of the DAQ system in one module. Unfortunately, there were problems when reading out the common clock, which is essential for trustworthy list mode data. Meanwhile this problem seems to have been solved, so that a complete substitution might be possible in the near future. One drawback of the system could be a lower maximum count rate and a slightly worse timing resolution in comparison with the current system. Yet these issues requires further investigation, the system is very useful for on-line spectra and hit patterns of the detector, making it a powerful system for beam adjustment and tuning [Cap13].

3.5.3. Acquisition and analysis software

For the read out of the ADC modules via USB and CAMAC bus, as well as the writing of the list mode files, a modified MINIBALL code was developed [War]. The raw list mode data is pre-sorted and converted in a way that it can be analysed with the CERN ROOT framework [Bru97]. It is a powerful and widely used software package for the analysis and interpretation of scientific, especially high energy and nuclear physics data.

[12] Tennelec Inc. has become a division of Canberra Inc., a company by Areva Inc.

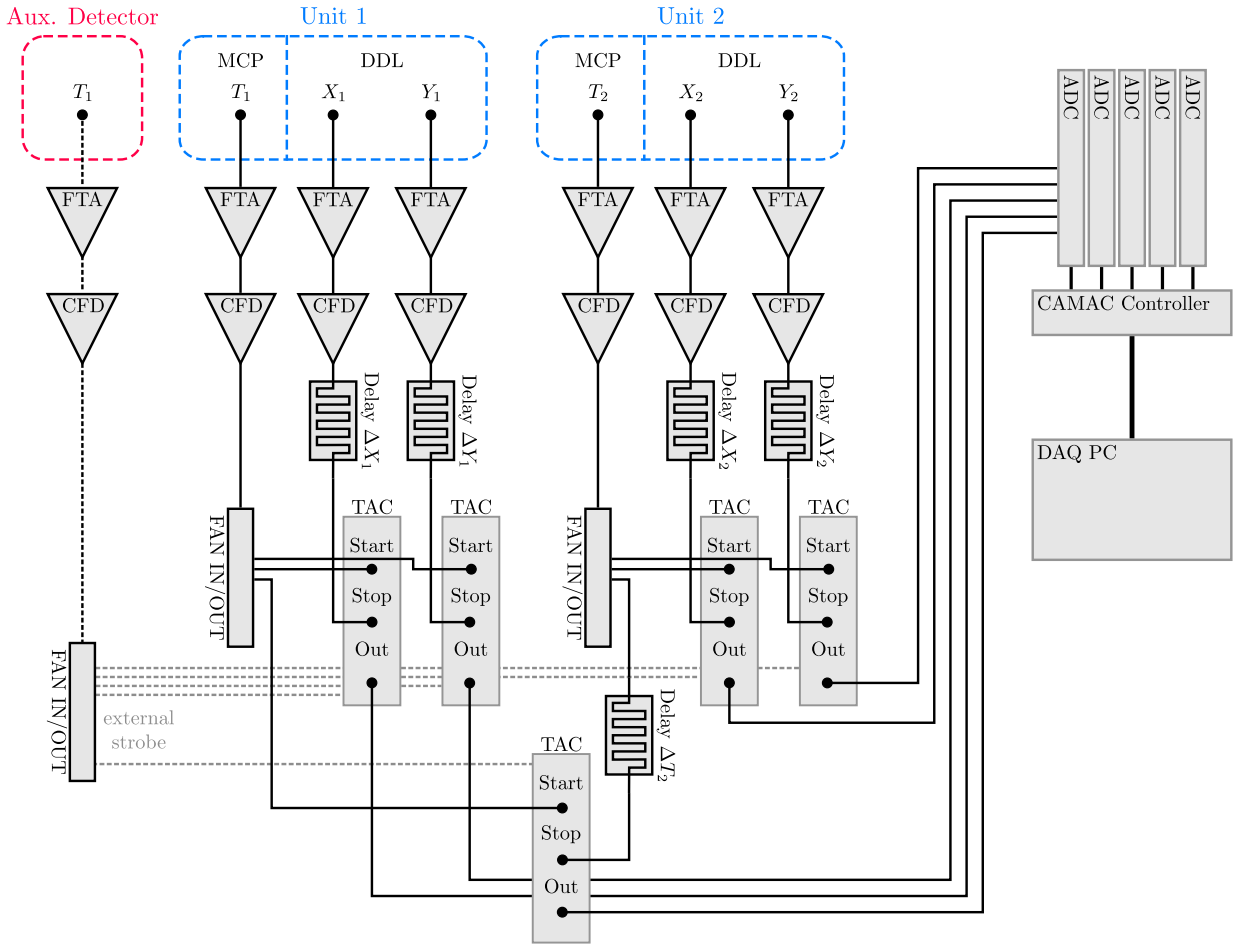

Figure 3.13.: Schematics of the basic common data acquisition system. An auxiliary detector can be used as a gate for the TACs at their *external strobe* input. The delays have to be adjusted to fit the dynamic range of the TACs. Important is a common cable length, i.e. delay between the TACs and the ADCs since the internal delay of each TAC is quite limited.

4. Prototypes

In the context of detector development, two major prototypes were built. A first version to test the basic functionality of such a system, from which a second, improved version evolved. The major differences between both system, besides an overall improved mechanical structure, are the different front-end electronics and a different design of the electrostatic top-assembly. Additionally, attention was turned to an overall design which allows a practical and time efficient maintenance during experiments in expensive beam times.

Furthermore, two testbeds were built. A basic testbed for testing mostly the first version with different kinds of radioactive sources and a second one, attached to the Cologne FN-Tandem accelerator, to mostly test the second version.

4.1. First version

4.1.1. Mechanical design

The first prototype was built similar to a start detector of the CORSET TOF spectrometer [Koz08]. Its major advantage is its monolithic top-assembly. It combines the conversion, reflecting and detector module via one triangular, helical ground winding, as shown in figure 4.1(a).

This kind of design makes the whole electrostatic top-assembly very compact and easy to handle. However, there are certain drawbacks. The conversion foil has to be of a minimum strength, since the electrostatic forces only point to one direction, i.e. the foil is attracted to the helical ground winding. Practical experience showed that only the plastic foils being used (as described in section 3.2.2) could withstand these forces. Even quite stable, self sustaining carbon foils of up to 0.15 mg/cm^2 (0.666 µm) thickness broke around the central spot of the foil, where the stability is probably the weakest.

Another drawback is the non homogeneous field introduced by the winding itself. Since a mesh has wires in both axes of its plane area, a winding consists only of parallel wires in one axis. This leads to a distortion in the electrostatic field, which results in a non homogeneous deflection of the passing SE . A more precise description can be found in section 5.3.2.

The whole setup is mounted on four small rods fixed on a base plate made of aluminium. Each single structure can be stacked with the help of these rods, i.e. the DDL package, the MCP sandwich-like package and the complete electrostatic top-assembly including reflecting and conversion module. The distances can be varied by washers and the whole stack is fixed by small screws, pressing the components

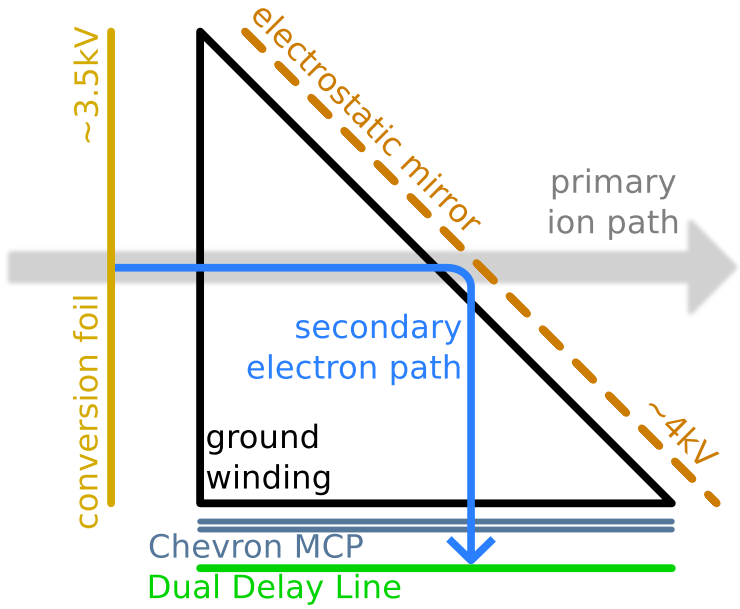

(a) First prototype.

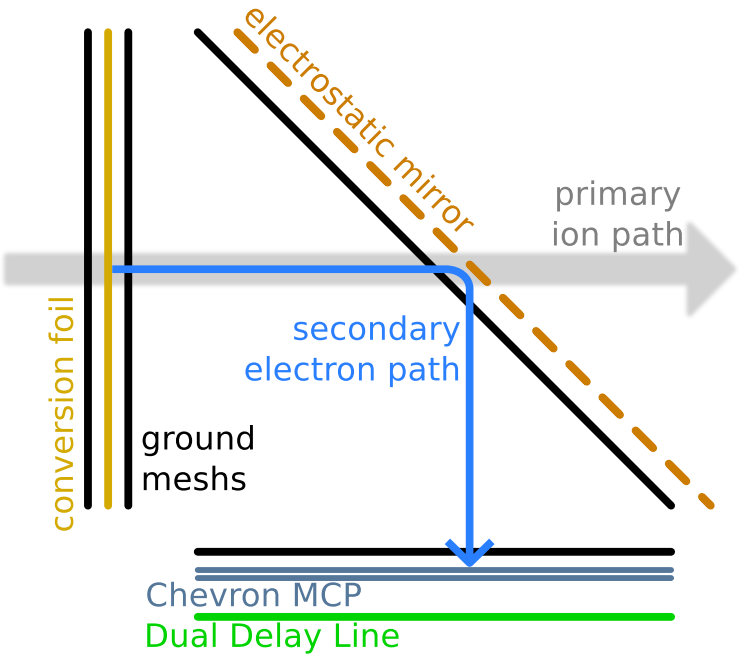

(b) Second prototype.

Figure 4.1.: Schematic sketches of the mechanical designs of the first and second prototype. The major difference is the de-coupling of the conversion, reflecting and detection module by the use of meshes instead of the helical ground winding, resulting in more homogeneous electrostatic fields. Note the additional mesh in front of the conversion foil to compensate for the electrostatic forces in figure 4.1(b).

slightly together. This stacking structure can be seen in picture 4.2, which shows a fully mounted first prototype. More detailed pictures of a stepwise dismantled unit can be seen in appendix A.3 and A.4. Essential parts of the mounting system and supply structure are electrical isolating and equipped with small venting holes, in order to allow for a faster pressure gradient during the evacuation of the chamber. A technical drawing of the first prototype can be found in appendix A.5, including a detail of a small mounting rod.

4.1.2. Front-end Electronics and HV supply

As described in section 3, one needs at least two charge sensitive, differential preamplifier for the DDL and one fast timing preamplifiers for the MCP read out. The whole detector is supplied by a high voltage divider, similar to the CORSET detector head [Koz08]. All devices were developed and build in house with the help of the electronics workshop [Pas]. The circuit diagrams can be seen in appendix A.6, A.7 and A.8.

The three preamplifiers can easily be exchanged by SMT[1] type plug-in connectors, both at the supplying motherboard and the detector side. Since the devices are mounted inside the vacuum, one has to be careful concerning the heat production of the electronics. Measurements with thermally glued PT-100 sensors under realistic load conditions at 150 mW showed 60°C for the active components, while the PCB reached 50°C. Both values are within the specifications of the used components. The final revision of the preamplifier had an intrinsic rise-time t_r and fall-time t_f of roughly 600 ps at 50 Ω matched outputs. A later and final used revision improved t_r and t_f to be 300 ps at the same output impedance. A fully equipped motherboard can be seen in picture 4.2(b).

The major advantage of such low impedance preamplifiers is the short time, in which the charge flows through them. Thus, the signal pile up and channel crosstalk is limited, resulting in a low sensitivity to parasitic signals. All this accounts for the very good timing resolution. However, a major drawback is the accompanying very poor signal to noise ratio, since the preamplifiers are highly sensitive on the return ground loop.

The high voltage divider was mounted on the same motherboard. In principle it consists of a well defined arrangement of different resistances. Since in the early phase of development only one dual HV power supply unit was available, the HV divider of each BPM/TOF unit was fed by only one variable voltage. Thus the ratio of the potentials between all components of one BPM/TOF unit were fixed in advance and only the absolute value could be modified. Since there was an urgent need to at least de-couple the HV supply of the electrostatic top-assembly from the detector head, a quad channel HV power supply was used. Therewith, a second revision of the HV dividers was built, being fed by two HV channels to separately control the electrostatic top-assembly and the detector head. However, all components share the

[1] **s**urface-**m**ount **t**echnology

same electric ground, which influences the signal to noise ratio of the preamplifiers a lot. Thus one has to take care to not get any resonances or oscillations on the ground loop. Experience shows that especially turbo-molecular pumps and USB controllers induce a lot of noise and thereby false signals if sharing the same ground loop with the detectors. The best solution is a complete galvanic isolation.

4.2. Second version

4.2.1. Mechanical design

From the experiences made with the first prototype, major changes in the mechanical design were introduced in the second prototype. Besides a different mounting concept, the helical ground winding was rejected in favour of a sandwich like structure of the three major modules (as described in chapter 3). In order to be able to use very thin, self-sustaining carbon foils of the desired size (see section 3.2.2), the conversion module is extended by an additional mesh in front of the conversion foil. Therewith the electrostatic forces are compensated, keeping the foil in equilibrium. The price is an additional mesh obstructing the primary ion beam path.

Another advantage is the more homogeneous accelerating field between the inner ground meshes and the conversion foil as well as the reflecting mesh respectively. In this way a better condition for a $1:1$ projection in both axes from the SE emittance spot on the foil to the MCP is achieved. A calculation according to section 3.3.1 has been performed in order to specify the dimensions of the distances. Figure 4.3(a) shows the resulting plot of this calculation. The accelerating potential is fixed at $\Delta V_{\text{foil}} = 3\,\text{kV}$ for a given thickness $d = 5\,\text{mm}$ of the reflecting module. The reflecting potential varies between $\Delta V_{\text{mirror}} = 2.5 - 3.5\,\text{kV}$, resulting in corresponding distances L_1 (conversion module and reflecting module) and L_2 (reflecting module and detector head). Unfortunately, the given values cannot be realised at the given dimensions of the modules. Thus the smallest possible values were chosen, which are $L_1 = 70\,\text{mm}$ and $L_2 = 67\,\text{mm}$. Optionally one can mount the system to distances of $L_1 = 85\,\text{mm}$ and $L_2 = 87\,\text{mm}$.

Thus the only possible solution is to increase the mesh distance of the reflecting module to $d = 35\,\text{mm}$. A result for such a calculation can be seen in figure 4.3(b). Though only $d = 5\,\text{mm}$ frames are available in order keep the detector as compact as possible. Thereby it can be scantily fitted within a ISO200 beam tube cross. Otherwise ISO250 dimensions had to be chosen. Furthermore, the spatial resolution of the first prototype with similar distances have been chosen to approximately fit the specifications if one neglects the effect of helical winding, as discussed in sections 5.2.2 and 5.3.2.

From a practical point of view, the modular sandwich structure is favourable in terms of maintenance. The setup allows for a quick and easy exchange of single modules. In most cases, only four little screws have to be loosened. Thus, the overall time to get the system running again during an expensive beam time is reduced to a minimum. Additionally, nearly all wiring is realised by easy plug-in connectors.

(a) Front view.

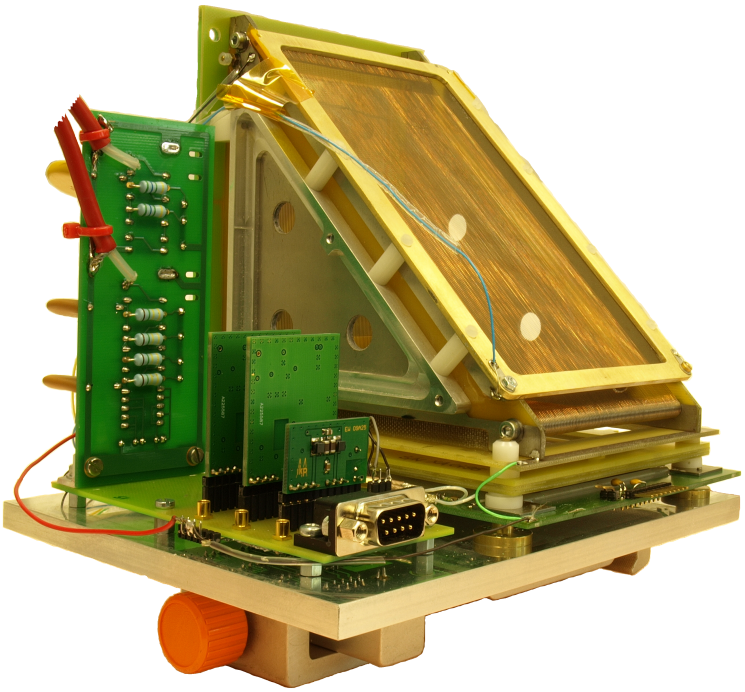

(b) Back view.

Figure 4.2.: Both pictures show a fully mounted unit of the first prototype. Picture 4.2(a) shows a front view in direction of the ion beam. One can figure out the stack-like mounting below the golden conversion foil. The back view 4.2(b) additionally shows a fully equipped motherboard of the front end electronics. One can clearly see the two channel HV divider, the two position and one timing preamplifiers.

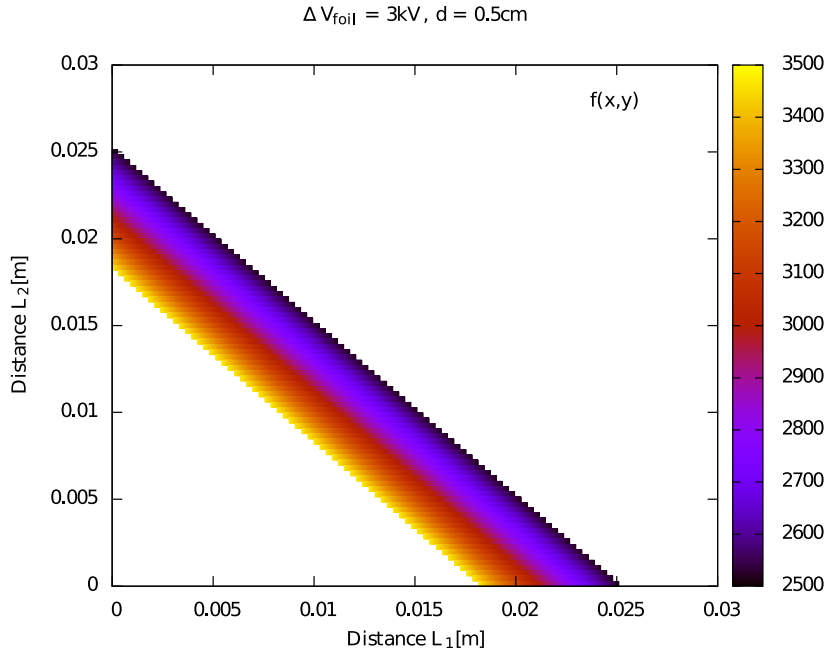

(a) Calculated distances for $d = 5$ mm.

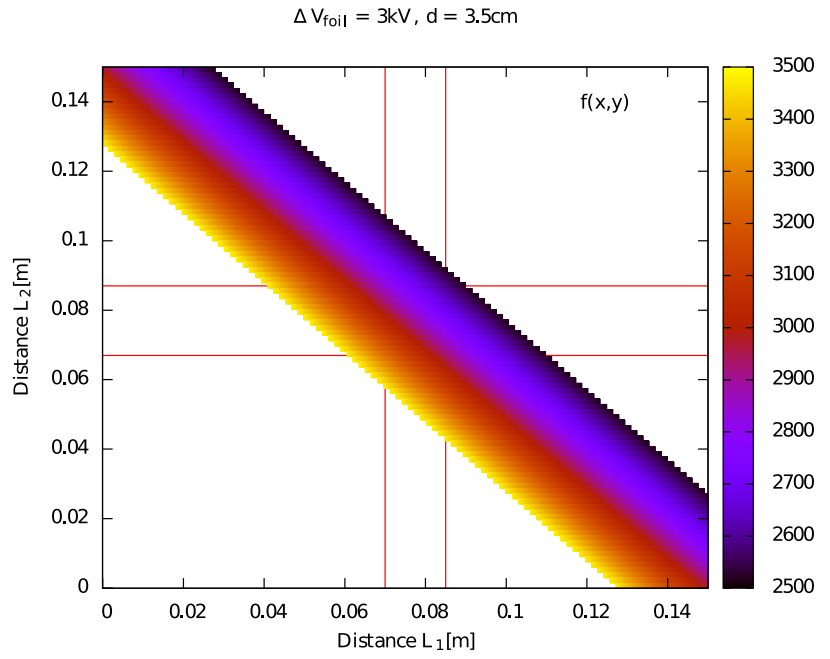

(b) Calculated distances for $d = 35$ mm.

Figure 4.3.: Theoretical calculation of the distances according to figure 3.4 for a fixed accelerating and a varying reflecting potential, which is marked by the Z axis. The possible distances of the prototype are marked by red lines in figure 4.3(b). Note the different scale of both figures.

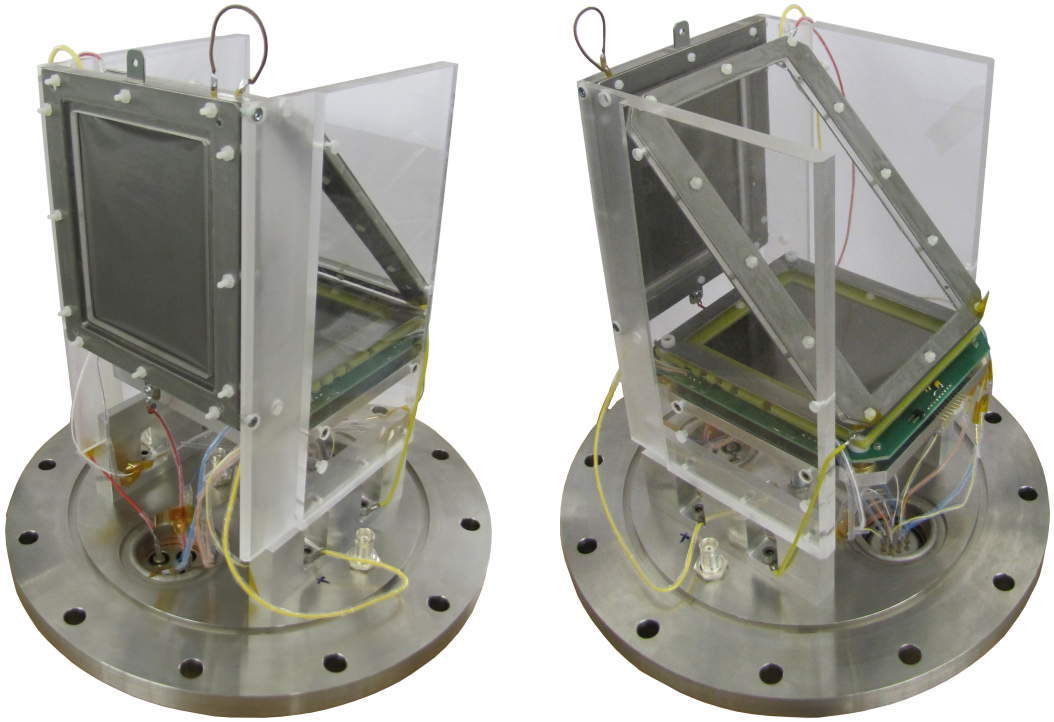

(a) Front view. (b) Back view.

Figure 4.4.: Both pictures show a fully mounted unit of the second prototype. Picture 4.4(a) is a view from the front in direction of beam. One can clearly see the additional mesh in front of the conversion foil. Note that all active electronics are not on the vacuum side in this version.

A fully mounted, single unit can be seen in figure 4.4. Figure A.10 shows technical drawings for different viewing angles.

4.2.2. Front-end Electronics and HV supply

The concept of directly attached, in-vacuum preamplifiers was refused. Instead, the signals were inductively de-coupled. For this purpose RF transformers type number TC3-1TGG2+ by MiniCircuits[2] were used. A wiring scheme can be seen in figure 4.5. The impedance of each line of the DDL is roughly 150 Ω, while the output of the preamplifier and the coaxial connections is 50 Ω. Thus the ratio $Z_{in}/Z_{out} = 3$ (with respect to figure 4.5) was chosen to be impedance matched for the front end electronics. The DDL itself is supplied with two positive potentials, one for the reference delay lines U_{ref} and one for the signal collection delay lines U_{sig}, as mentioned in section 3.4.2. Thereby $U_{holder} < U_{ref} < U_{sig}$ is essential since the multiplied SE spill emitting

[2] Mini-Circuits, Europe Dale House, Wharf Road Frimley Green, Camberley, Surrey GU16 6LF United Kingdom

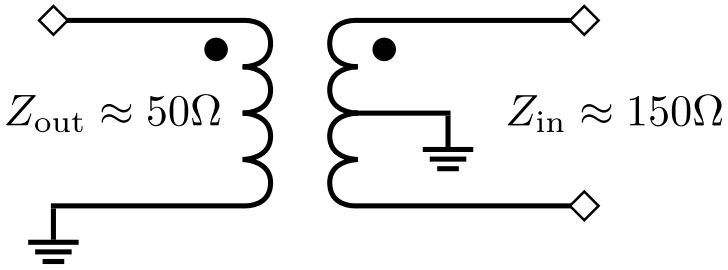

Figure 4.5.: Sketch of a transformer type TC3-1TGG2+ by Mini Circuits Inc., as used for the inductively de-coupling of the signals. This figure is based on [Pas11].

from the MCP should be collected mostly on the signal delay line, whereas U_{holder} is the potential of the reflecting plate. To reduce the amount of HV supplies, a small HV splitter box was built. Table 4.1 summarises the corresponding output potentials for a given, normally used input voltage of +350 V.

A complete schematical drawing of the DDL front-end electronics is shown in figure 4.6. One advantage of this wiring is the possibility to read out both ends of each DDL axis, i.e. X_1 and X_2 as well as Y_1 and Y_2 respectively. In the shown figure, one end of each axis is terminated with 50 Ω and the other is directly fed to the preamplifier. If enough channels in the back-end electronics are available, one can use both ends, for sure. Though in most cases, the financial effort is not worth the benefit. To secure the transformers a small capacitance is embedded and to secure the HV supply, a high resistance is integrated.

For practical reasons a connector and feed-through adaptor type FT12 by RoentDek[3] was used. It provides a 12 channel feed-through and all the above mentioned electronics included in one handy size connector plug. It furthermore provides a high voltage resistant transformer for the inductive signal de-coupling of the chevron stack MCP. Its working principle is basically the same as for the DDL. A detailed sketch of the front-end electronics can be seen in figure 4.7. As indicated, the FT12 features the possibility to apply a potential to the mesh in front of the MCP, the so called MCP grid. For most cases it is sufficient to terminate the MCP grid to ground potential, as shown in the figure. Yet in rare instances it can be useful to induce a small potential and use the MCP grid as ion optical element. Another option is the choice whether to pick up the timing signal from the front or back side of the MCP chevron stack. Experience showed that for this fast timing application it is mostly preferable to pick the signal from the back side, since the timing pulse has a slightly smaller rise-time.

Afterwards, all signals are fed to ultra fast, low noise current preamplifiers based on ZX60-33LN-S+ amplifiers by MiniCircuits. The required 6 V power supply is realised by the in house developed NIM power supplies. A major advantage of this solution is that all active components are out of the vacuum chamber, tremendously improving the overall vacuum performance in terms of pumping speed and minimum

[3] RoentDek Handels GmbH, Im Vogelshaag 8, 65779 Kelkheim, Germany

Table 4.1.: Output potentials of the HV splitter for the DDL.

Input	+350 V
U_{sig}	+250 V
U_{ref}	+200 V
U_{holder}	+165 V

reachable, absolute pressure. As mentioned before, during the design of the second prototype attention was turned to a practical maintenance during experiments. Thus the chosen solution is preferable. Another major advantage is a lower sensitivity to the ground return loop as well as an improved signal to noise ratio. The price is overall poorer signals, especially for the DDL. Due to the factor 3 impedance matched transformers the signals amplitude is roughly a third of the ones obtained with the first version preamplifier. Accordingly, the width of the signals is increased, as well. To decrease these effect as much as possible, the connecting cables between the in vacuum components and the feed-through have to be as short as possible.

For the second prototype two high voltage supplies type N1471 by Caen[4] were used, one for each BPM/TOF unit. Each module provides four channels with an output range of 5.5 kV at 300 μA each. They are fully programmable and remotely controllable. However, three of four channels are used for the conversion, reflecting module and the MCP. While these channel are on negative potential, the fourth channel provides positive potential for the DDL including the reflecting plate. To split and adjust the fourth channel to these three elements, a small voltage divider was build. A drawback is the fixed ratio of the potentials being applied. Fortunately, the influence on the spatial tracking performance is negligible.

[4] CAEN S.p.A.,Via Vetraia, 11 55049 - Viareggio (LU) - Italy

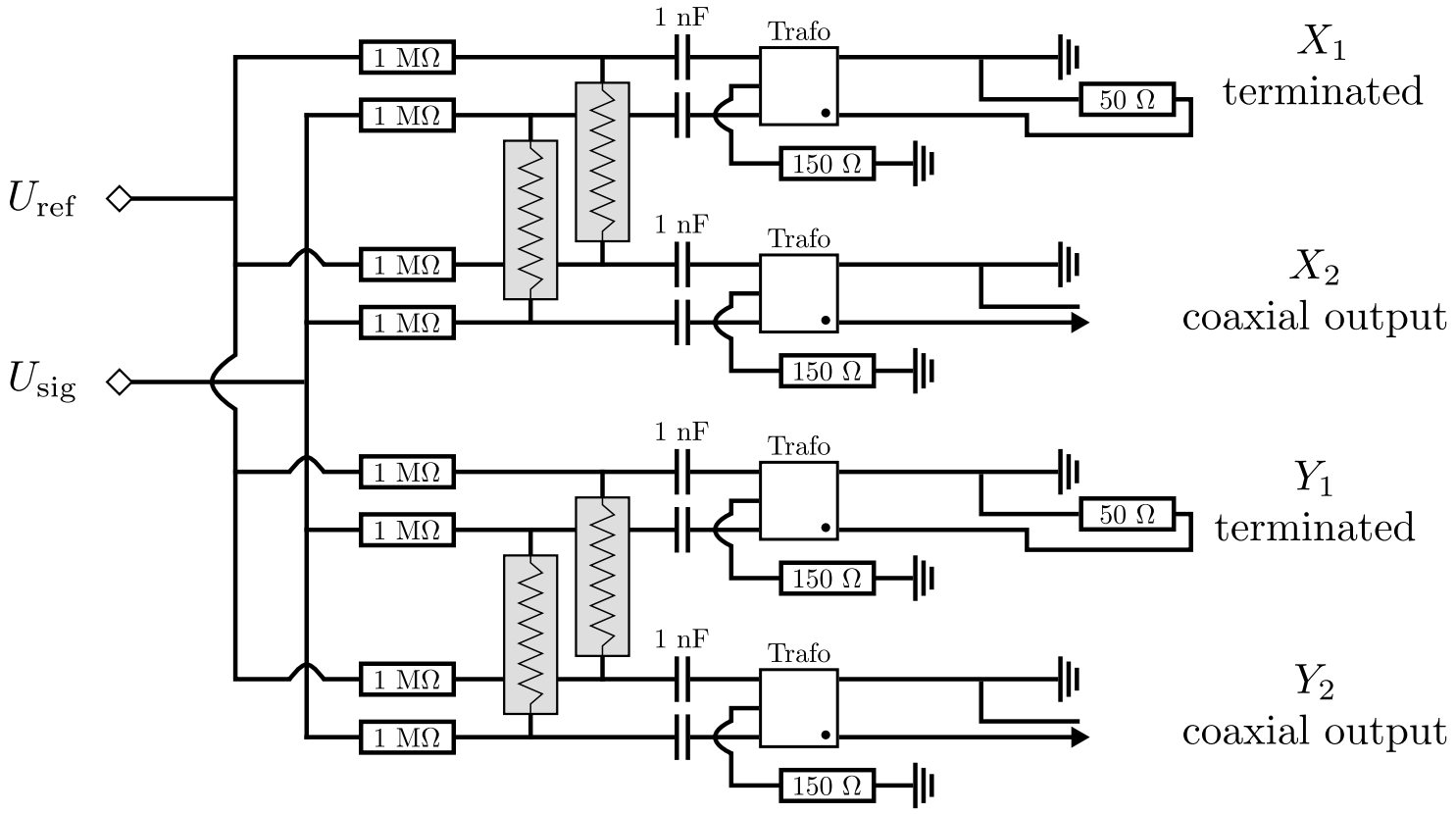

Figure 4.6.: Schematical drawing of the second version DDL front-end electronics. Note that the transformers, which are of the type shown in figure 4.5, as well as the collecting and reference delay lines for X and Y axes marked by the grey rectangles. This figure is based on [Pas11].

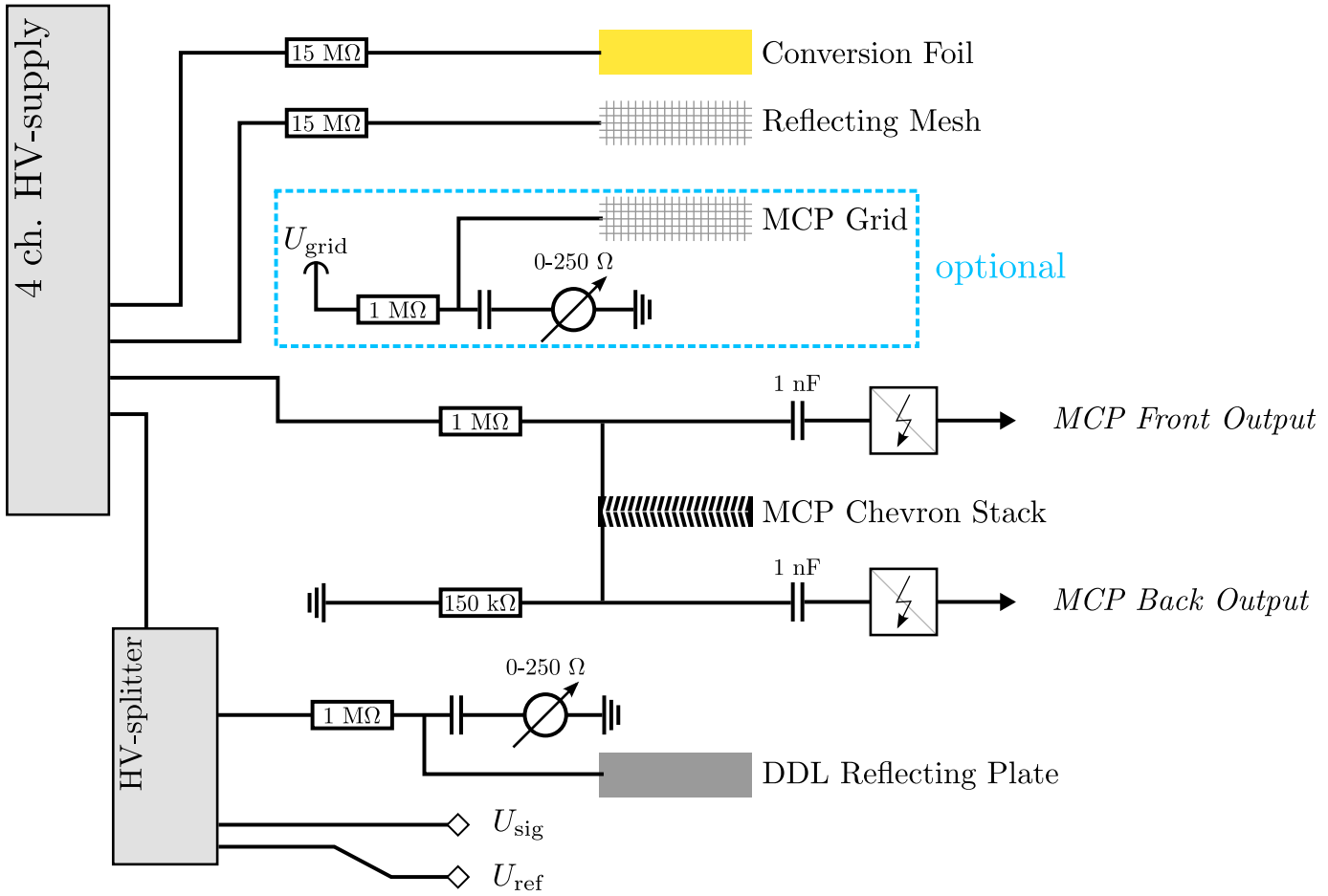

Figure 4.7.: Schematical drawing of the second version front-end electronics without the DDL. Note the option to apply a potential to the ground mesh in front of the MCP, the so called MCP grid. The other ground meshes are missing for clarity. This figure is based on [Pas11].

4.3. Testbeds

First tests have been performed with radioactive sources in a specialised testbed. A later series of tests has been performed at GSI . The detector development and prototyping started in a phase, in which the Cologne 10 MV Tandem Van-de-Graaf accelerator was shut down for a complete refurbishment of the accelerator laboratories. Thus the detector could be tested under real beam conditions only in a late development stage. Therefore a dedicated beamline for detector tests was set up. This section will give a short summary of these different testbeds and laboratories.

4.3.1. First dedicated laboratory

For very early tests a dedicated testbed was built. Its major component is a huge chamber with $40 \cdot 40 \cdot 60\,\mathrm{cm}^3$ inner dimensions. Two turbo-molecular pumps model TurboVac 361 by Oerlikon Leybold[5] were directly attached. However, to reach a vacuum of below $5 \cdot 10^{-6}\,\mathrm{mbar}$ it took roughly 72 hours. After a polishing of the inner wall of the large maintenance and access flange as well as replacing all sealing, the desired vacuum could be reached within 48 hours.

The chamber itself had various feed-throughs for a flexible rearrangement of components and sensors, e.g. PT-100 temperature sensors as mentioned in section 4.1. At the left, small front side a standard $4''$ HV beam tube as used at the in house accelerator was attached. Within the chamber, an optical bench was aligned with the beam tube in a way that the centre of the conversion foil (i.e. the active area) matched the centre of the beam tube. The single units were mounted on sledges, which allowed a very flexible handling of different distances and additional masks. In picture 4.2(b) one can see the aluminium base of the unit fixed on such a sledge.

The beam tube itself was used to hold various radioactive sources. Most common these were ^{241}Am and a triple Alpha source containing ^{239}Pu, ^{241}Am and ^{244}Cm. A special sledge, which could be moved alongside the beam tube was built to mount the sources. An integrated collimator focused the Alpha particles in direction of the detectors. A picture of this source-pod can be seen in figure A.2. Therewith accelerator beamlike conditions could be simulated. Since the count rate decreases with a larger distance and collimation of the source, a trade off between these parameters and the quality of the beam spot has to be made. For this purpose, a 1.4 MBq ^{241}Am source was bought especially for this testbed.

Later on the whole laboratory was moved to an acclimatised room, since temperature oscillations influenced the electronics and the vacuum likewise. Additionally, a small chamber for MCP storage purposes was attached to the vacuum system. This whole setup can be partly seen in picture 4.8.

[5] Oerlikon Leybold Vacuum GmbH, Bonner Strasse 498, 50968 Cologne, Germany

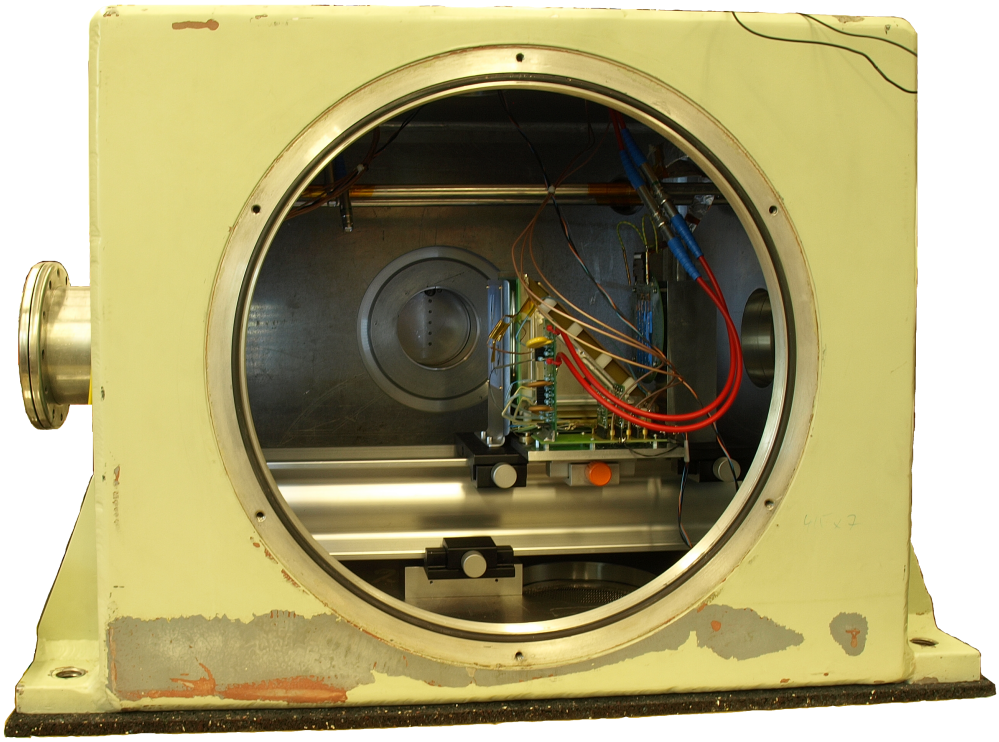

Figure 4.8.: This picture shows the large vacuum chamber of the first testbed. The access flange is opened and one can see the optical bench equipped with a single unit. In front of the unit a mask is placed. The whole chamber is placed on a damping mat. On the left side one sees a part of the attached beam-tube, which functions partly as holder for the source sledge.

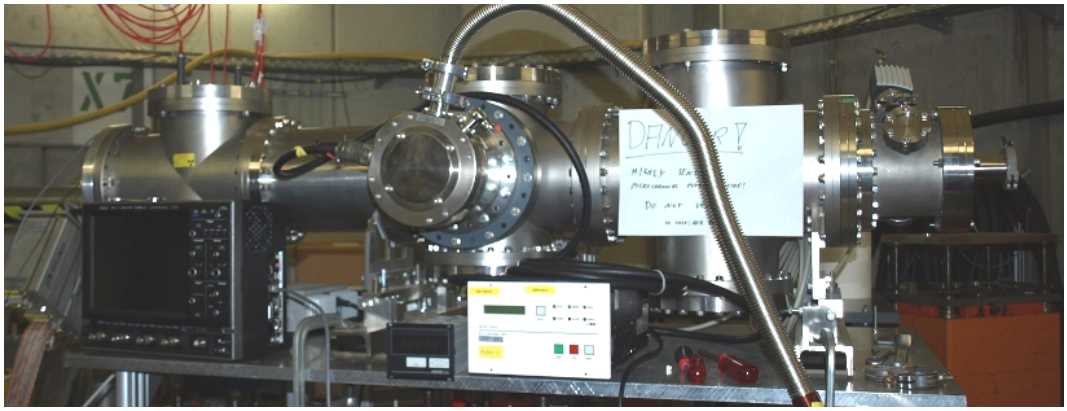

Figure 4.9.: A picture of the vacuum chamber of the X7 laboratory at GSI. The DSSSD was mounted at the very left of the tube shaped chamber and the single unit was mounted in the beam tube cross at the right side, marked with a A4 paper.

4.3.2. GSI X-7 laboratory

At the end of the development phase of the first prototype, measurements with an open ^{252}Cf spontaneous fission source were performed. Since such sources are very spare, the whole setup was taken to GSI, which is permitted to handle such sources. The complete detector was mounted in a tube shaped vacuum chamber in the X-7 cave of the UNILAC experimental hall.

As an additional trigger, a **D**ouble **S**ided **S**ilicon **S**trip **D**etector (DSSSD) with ultra fast timing electronics was used as absolute calorimeter [Gre11]. Unfortunately the ^{252}Cf had an activity of only circa 300 Bq. The source was mounted directly in front of the conversion foil of the single unit. The distance to the DSSSD with an active area of $10 \cdot 10\,\mathrm{cm}^2$ was roughly 155 cm. All positions were fixed and could not be changed.

If one takes the ratio of a spherical area with its radius being the distance between the single unit and the active surface of the DSSSD one can estimate the detectors count-rate. For these parameters one gets roughly 0.1 Bq of activity for the active DSSSD surface, which corresponds to the observed countrate for the whole setup. Thus, the whole tuning and measurement took several days before having appropriate statistics. On the other hand one can set quite high thresholds with the measurement of heavy fission products, which leads to excellent, nearly noise free statistics. In addition, the vacuum of down to $3 \cdot 10^{-7}$ mbar tremendously favours the MCP performance when it comes to ion feedback effects, as described in section 3.4.1. Picture 4.9 shows the vacuum chamber situated in the X7 laboratory at GSI.

4.3.3. New integrated testbed

For the second prototype a complete new testbed was built, which consists basically of two directly connected ISO-K 200 five-way beam tube crosses. Each cross holds one detector unit and is equipped with a turbo-molecular pump model TurboVac 361 by

Oerlikon Leybold. A single unit is mounted on an ISO-F 200 stainless steel flange, as seen in pictures 4.4 and 4.10. The feed-throughs are fixed with ISO-CF copper sealing for a good electrical connection, since the flange is used as ground. The exact distance between both detector units of the second prototype (see section 4.2) mounted inside this chamber is 36 cm. Note that the detector units are turned by 90° in comparison to the earlier testbeds.

The third port on the side of the chamber is equipped with an adaptor to a KF25 flange. Thereby commonly used vacuum gauge meters, other auxiliary devices or vacuum components can be easily attached. For an easy commissioning the complete chamber is held by a stable aluminium plate, which has different degrees of freedom for spatial adjustment. Thus one only needs four threaded bars as seating for the whole setup. At the front and back side of the chamber one can attach various adaptors to integrate the testbed in the given beamline structure. Picture 4.10 shows the integrated, new testbed in a beamline.

4.3.4. Dedicated beamline for detector tests and the simulation of wide beams

For final testing under realistic conditions, a dedicated beamline was set up at the in house accelerator laboratory. It is situated under 0° behind the 90° analysing magnet, as seen in figure 4.11. The accelerator itself delivers a large variety of beams (except noble gases) at energies of up to 10 qMeV with a maximal ionic charge of $q = 8-9$ e. Beam currents vary between few pA and several hundred μA. Even though very little beam currents are hard to achieve, the beam can be pulsed, which can reduce the current at target position tremendously without influencing stable operation parameters of the accelerator.

The beamline itself is equipped with special ion optical elements. Figure 4.12 gives a schematical overview over the beamline. As one can see, the beam can be further focused with the help of an additional quadrupole magnetic lens, framed by two slits. At the very end of the beamline, the large vacuum chamber mentioned in section 4.3.1 can be placed to mount miscellaneous detectors. Before this chamber the BPM/TOF detector is placed, framed by two pneumatic movable cups for focusing purposes.

The beam itself can be deflected over the whole focal plane by an electrostatic sweeper. A specialised software was written within a bachelor thesis, which allows a comfortable programming of any user-defined or random deflection pattern of the beam. Furthermore an automatic sweeping mode can be set with a saw tooth voltage generator [Die12].

Thereby this beamline can be used in order to test auxiliary detectors for future slowed down beam experiments under realistic conditions, as mentioned in section 1.3. A huge advantage is the flexibility and low cost possibility to test such detector systems before their final usage at the future FAIR.

First tests have already been performed by a group from GSI testing ultra-fast DSSSD stopping detectors. Since the specialised kind of detector used is very sensitive to radiation damages, the testbed had to be modified. Right after the BPM/TOF

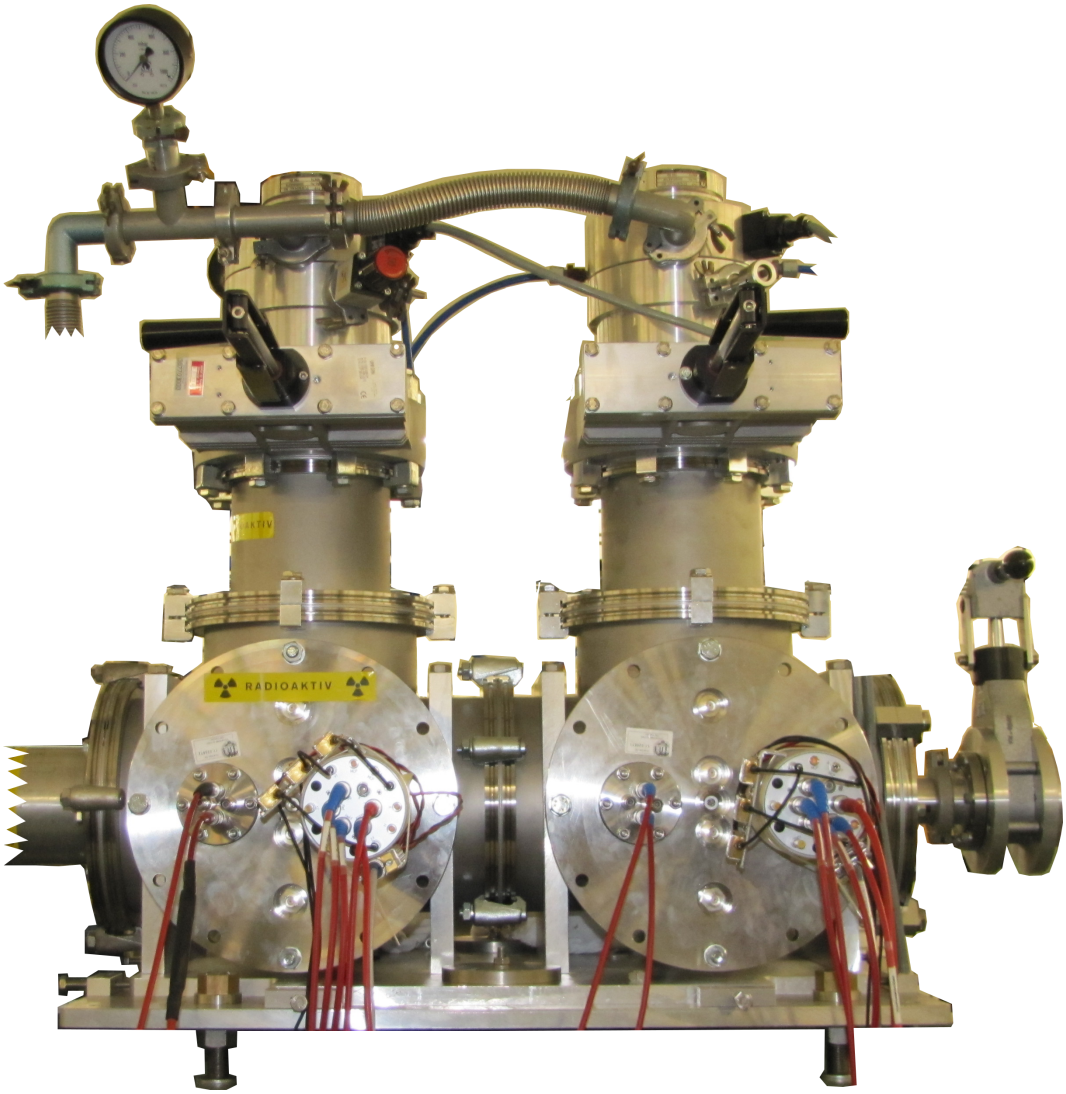

Figure 4.10.: This picture shows the new testbed for the second prototype, integrated in a beamline. One can figure out the two directly connected beam tube crosses, fixed on an aluminium plate. On top there are two turbo molecular pumps, while at the front one can see the two flanges which hold one of the units each. The cylindrical structure on the right side of each flange is the FT12 feed-through, as mentioned in section 4.2. To the left and right of the chamber one partly sees the beamline. On the not visible side adaptors to KF25 flanges are mounted.

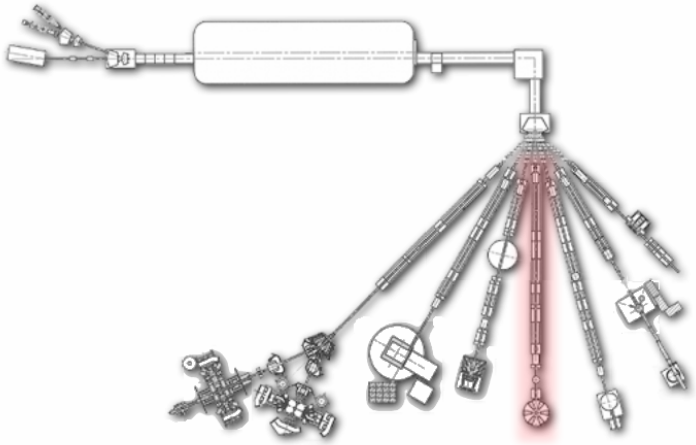

Figure 4.11.: This figure gives an overview over the Cologne FN Tandem accelerator and its beam-lines. The new dedicated beamline for detector tests and the simulation of wide beams is marked in red and situated under 0° behind the 90° analysing magnet.

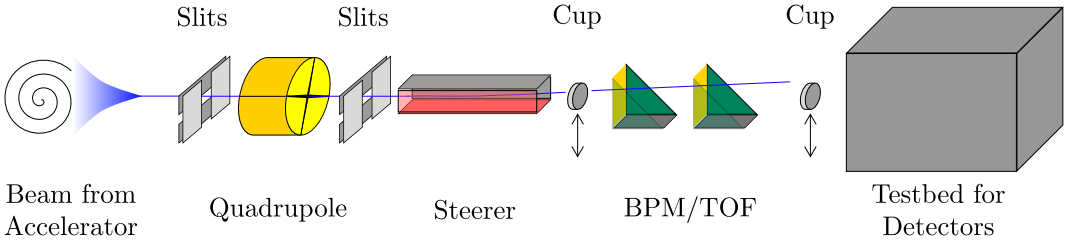

Figure 4.12.: Schematics of the new, dedicated beamline for detector tests and the simulation of wide beams. The beam being delivered by the accelerator is already focused.

detector a scattering target was placed and the X-7 chamber, as described in section 4.3.2, was attached under 20° [Bou13].

5. Measurements and analysis

During the research and development phase of the detector, an enormous amount of measurements and experiments have been performed. Most of them were performed with the first prototype and the scientific findings from these experiments were directly applied to the development of the second prototype. Tests with the second prototype have mostly been performed at the newly developed beamline, as mentioned in section 4.3.4.

Since some experiments and tests overlap and were performed more than once, for verification or commissioning purposes without advancing the development directly, this chapter will only present a selected set of experiments to not go beyond the scope of this thesis.

5.1. General remarks concerning the start-up of the detector and analysing the data

Before discussing selected experiments, a short summary of commonly used approaches and operation methods is given. In order to achieve best possible results, one has to provide good working conditions to operate the detector. Moreover, there are proven methods to filter and clean the data on the software site during analysis. A standard calibration procedure is discussed shortly.

5.1.1. Working conditions and operation of the detector

Even though the MCP signals for true events have a signal to noise ratio of about $10:1$, a lot of pulse shot noises occur, i.e. a huge increase in count rate occurs for circa half a second, resulting in false signals. The source of this effect are ion feedback effects, as described in section 3.4.1. To reduce this inconvenience as much as possible, the pressure should under no circumstances be higher than $1.3 \cdot 10^{-6}$ mbar. Much more advisable is a pressure in the lower 10^{-7} mbar regime or lower. Before operation, the MCP must be degassed at this pressure for at least 24 hours. For storage purposes the MCP can be kept under an oil free vacuum of maximum 0.13 mbar pressure. Another, but more complex option is the storage under a gentle and constant nitrogen flow with a humidity of below 20 % [Ham09].

Another important factor is the ramping or conditioning of the detector. Similar to a high purity germanium detector, the operation voltage should not be increased and decreased, i.e. switched on or off immediately. Instead the voltage should be ramped in smaller increments, interrupted by waiting times to let the MCP normalise. The

higher the potential gets, the smaller the increments and longer the waiting times get. If the MCP has been under atmospheric pressure or the vacuum has been collapsed in between, one should be even more careful. The DDL and reflecting plate on the other hand can be switched on nearly immediately. The same is legal for the reflecting module, i.e. the reflecting mesh. Using the conversion module with thick, metallised plastic foils, one can ramp at similar increments and waiting times. Furthermore, no special care is necessary when pumping vacuum.

When using a very thin carbon foil, which is very sensitive and easy to destroy, special attendance is needed for both, ramping up the voltage as well as pumping vacuum. Concerning the voltage, experience showed that it is reasonable to ramp very slowly at 50 V increments with 2 minutes waiting time when being below −1.5 kV. Until then, i.e. down to −1.5 kV, one can double the increment and halve the waiting time. Especially for the very first operation of the foil this is very crucial, since somehow the foil surface seems to condition itself. The more often a foil has been set under voltage and bombarded with ions, the more stable it seems to get and it can be ramped a bit faster.

Pumping vacuum from atmospheric pressure is always a very critical phase for the integrity of the foil and should thus be avoided as much as possible. If one has to do so, the pumping gradient should not exceed 20 mbar/min, i.e. reducing the chamber's inner pressure from 1000 mbar down to 1 mbar takes nearly an hour. Afterwards it can be pumped at maximum speed available. It makes sense to check the integrity of the foil with a multimeter from time to time. One can easily measure if there is a connection between the foil and the adjacent ground meshes. Table A.1 summarises all important parameters for setting up the detector to an operational state.

Once the detector is operational, the vacuum sensor should be secluded with a small valve, if using a ionivac type gauge meter. These kind of sensors produce quite a lot of ions, disturbing the MCP and thereby producing false signals.

When the detector is shot on with ions, one should firstly check all signals with a fast, i.e. at least 200 MHz, oscilloscope. An exemplary screen shot of raw, non-delayed signals taken after the first generation front-end electronics can be seen in picture 5.1. One can nicely see that the MCP signals come before the DDL signals and thus function as start signal, while the DDL signals function as stop signal for the DAQ, as described in section 3.4.2.

If all signals are present and of acceptable shape, one should tune the amplifier gains and constant fraction discriminator thresholds. For the former one simply needs to check that the signal does not saturate or that its amplitude exceeds the allowed input voltage of the following electronics. The latter should be set to a value that for each MCP signal one signal per DDL output occurs. Thereby it is very helpful to have an auxiliary trigger for the passing ions, either from the accelerator beam diagnostics or from a calorimeter behind the detector. Without a beam or sources, there should be no signals at all. If the threshold is too low, multiple signals will occur per passed ion, i.e. one measures a lot of noise coming from the MCP. If the threshold is too high on the other side, one discards a lot of true events. The delay of the constant fraction discriminator is normally set to a very low value of roughly 2 ns

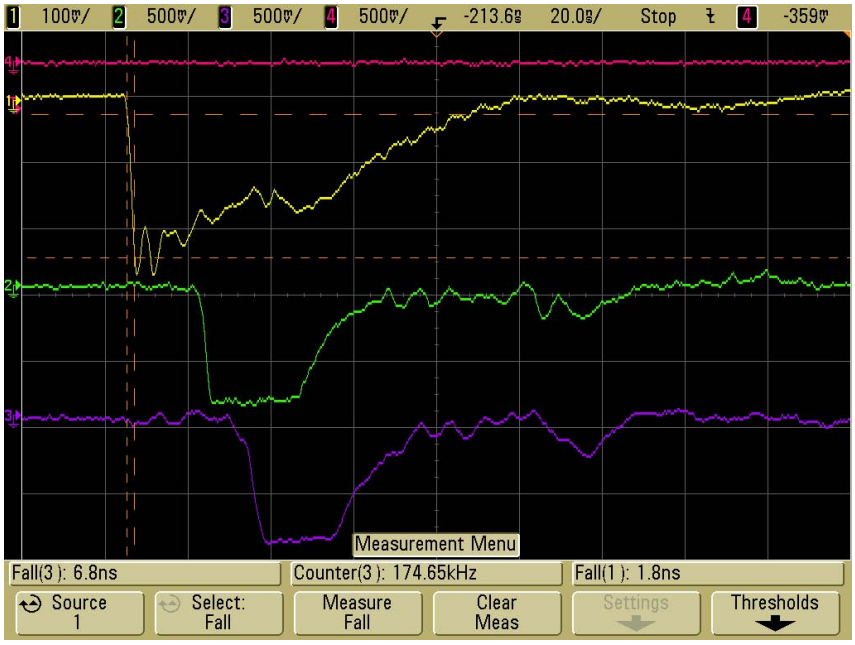

Figure 5.1.: Exemplary oscilloscope screen shot of raw signals as being delivered by one detector head after the first generation front end electronics. The yellow signal corresponds to the MCP, while the green and purple ones correspond the X and Y axis of the DDL, respectively. One can clearly see, that the MCP signals comes first while the DDL signals come afterwards. The red one can be neglected.

resulting in good signals for the most cases. It might still be useful to increase the delay in certain cases.

Once the detector is set up completely, one can start the DAQ. Since all data is taken in list mode format, one can apply software-based filtering and cleaning of the events afterwards.

5.1.2. Software based corrections

Even after the data is taken, the list mode format allows for certain corrections. To improve the signal to noise ratio offline, several methods can be applied, which will be discussed below. While the first was applied at nearly every and the second at only some measurements, the last two could not be applied, since specialised electronics were missing. Due to a possible future implementation and theoretical completeness, they will be discussed nevertheless.

Same axis events A very effective yet easy to apply method is to plot the first and second unit events of the same axis against each other, i.e. once for the X axis and once for the Y axis, respectively. Figure 5.2 shows these plots. As one can see in both plots, the events of both axes correlate strongly in their central distribution. Another detail is that in both plots the first unit events are plotted

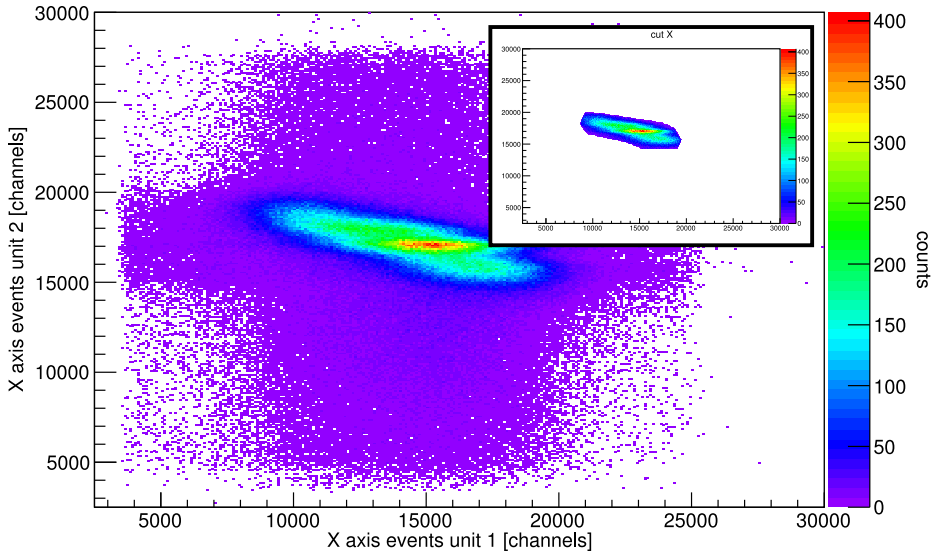

(a) X axis of units 1 and 2.

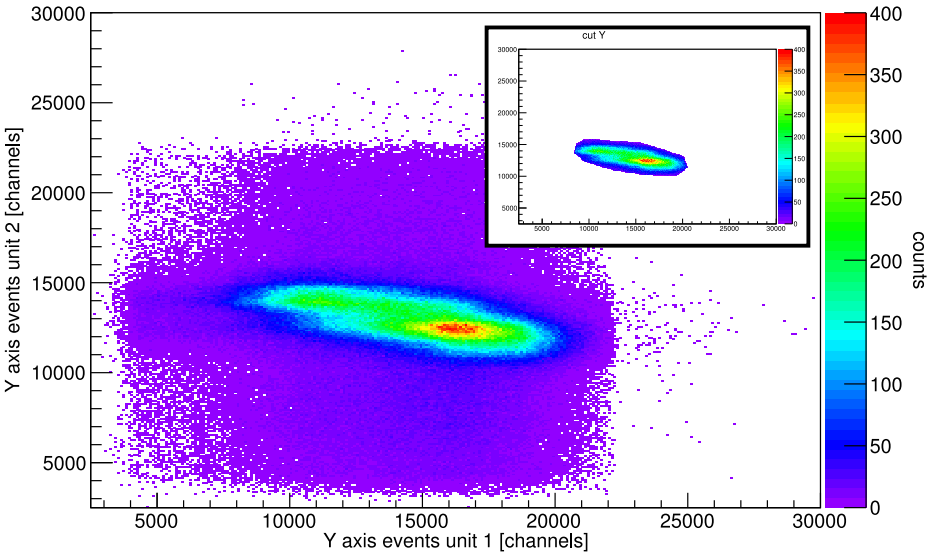

(b) Y axis of units 1 and 2.

Figure 5.2.: Plot 5.2(a) shows the X axis events of both detector units plotted against each other. Plot 5.2(b) shows the same for the Y axis events. Each sub plot shows a cut used for plot 5.3(b). Note that the main distribution does not follow an increasing, but decreasing line. This is due to the fact that for the second unit, the corresponding DDL signals were taken from the opposing end of the delay lines (while the other end is terminated) with respect to the first units signals. The data was taken with a divergent beam and thus the distribution does not exactly follow a straight line.

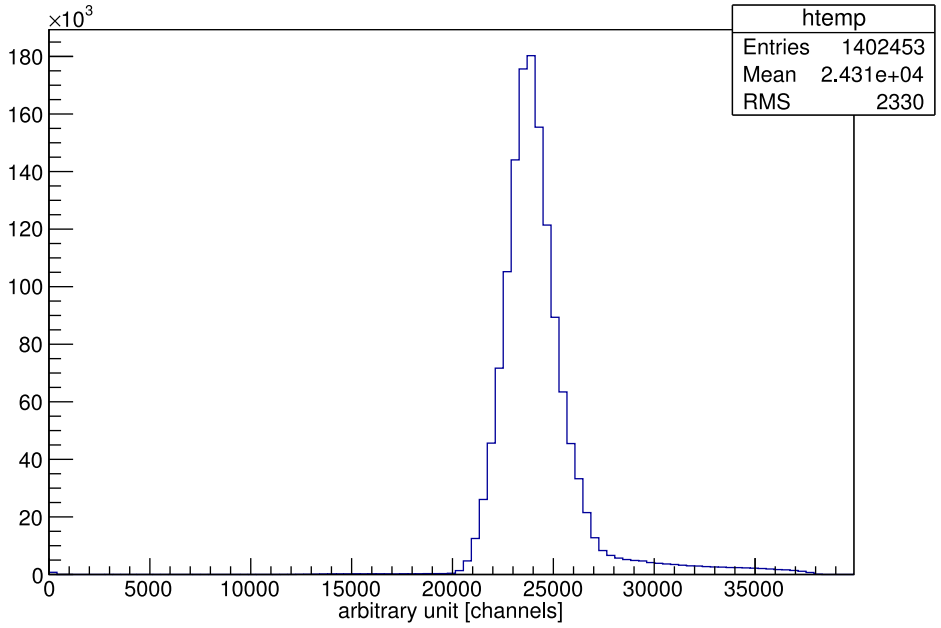

(a) TOF plot without cuts.

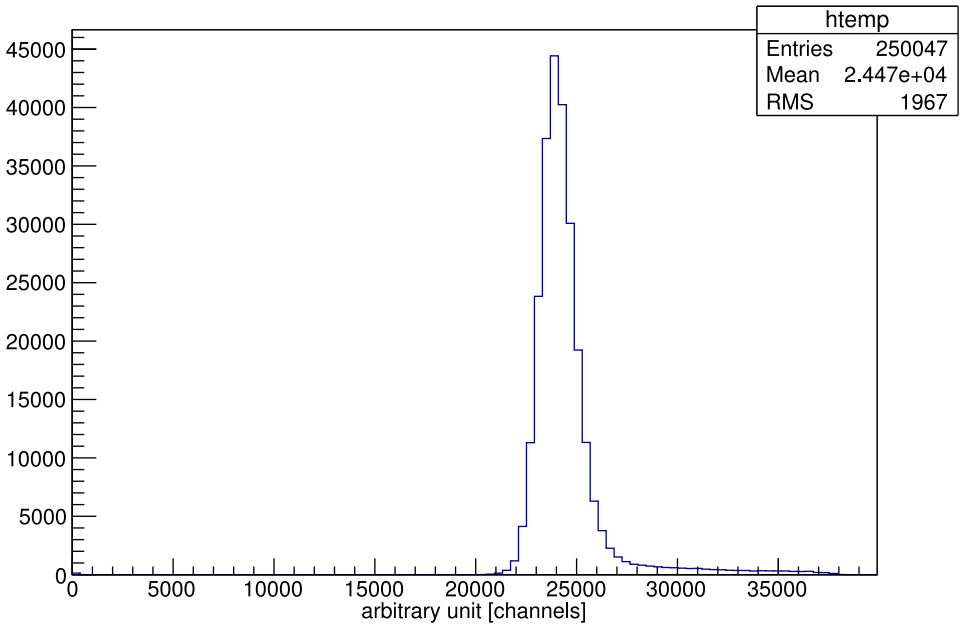

(b) TOF plot with cuts.

Figure 5.3.: Exemplary TOF between unit one and two. Plot 5.3(a) is without cuts and plot 5.3(b) with cuts based on plots 5.2. Note the difference in statistics.

on the horizontal axis, while the second unit events are plotted on the vertical axis. It is obvious that the events of both units should be correlated. Especially when looking at the vertical axis, i.e. first units events, one can distinguish a quite small distribution of roughly 5000 channels width, while the horizontal axis, i.e. the second units events, exhibits a rather large distribution.

Even though the units are in arbitrary channel numbers, the electronics are set to nearly equal values, which legalises the assumption that the primary ion beam is less broadened in the first than in the second unit. Especially since the primary ion beam is broadened from a point-like spot before the first unit and the angular straggling within the first unit is negligible. Hence, all true events in the second unit must correspond to the quite narrow distribution of events in the first unit.

If one applies a cut on both same axis plots, most of the random coincidence events can be filtered out. Cuts for the discussed sample measurement can be seen in the subplots in figure 5.2. As an example for this method, figure 5.3 shows plots of the corresponding TOF with (figure 5.3(b)) and without (figure 5.3(a)) these cuts. One can see an improvement in the root mean square of the distribution and an overall sharper peak. Of course, as it is always the case when applying cuts, the price is a reduction in the absolute statistics, in this case by roughly a factor of 5.

Auxiliary detectors As a matter of fact, one of the most effective methods to clean the data offline is the cut or gate on other, auxiliary detectors with a less noisy behaviour. Most valuable are absolute calorimeters or global triggers. As an example, a target DSSSD or a master trigger from the (pulsed) accelerator could be used. For a future use at GSI this would be the FRS-TOF or the last beam stopping scintillator.

Pulse height distribution If one has the opportunity to measure the pulse height of the MCP signals, one can plot the pulse height distribution, as described in section 3.4.1. Operating the detector with a primary beam of heavier ions, true events will most probably account for a larger amplitude of the signal, given the effect that heavier ions will emit more SE from the conversion foil.

Thus all true events will correspond to the higher value, Gaussian shaped part of the pulse height distribution with a high possibility, as seen exemplarily in figure 3.5. The lower value regime, falling exponential part is dominated by random, coincidence signals originating in noise with a low signal amplitude.

If one cuts on the Gaussian part, the data will be cleaned further. Of course, the price will again be a reduction in statistics.

Pulse height position Being able to measure the MCP pulse amplitudes, one can correlate these with the position information from the DDL anode. Assuming the MCP is illuminated by orthogonal impinging electrons of exactly the same energy and the MCP is completely homogeneous concerning its amplification,

one would expect a constant pulse amplitude over the whole active area. If one plots the pulse amplitude versus the position, once for the X and once for the Y channel of the DDL, one expects a straight line parallel to the x axis.

Unfortunately, this is not given in reality. Neglecting the fact, that the SE impinge at different angles with different energies, the amplification of the MCP is still inhomogeneous over the active area. For such a realistic MCP one would get a random looking curve for an above described plot. Fortunately, this curve is an intrinsic parameter of each MCP. Thus one can correct these curves to homogeneous distributions with polynomial fits for both axes and each unit, giving a correction matrix for the whole MCP active area. One has to be careful with the degrading of the MCP (see section 3.4.1 for details), resulting in a different correction matrix.

5.1.3. Calibration

Since the DAQ is completely based on the measurement of time intervals, a fast pulser and calibrated delays are sufficient in order to achieve a good calibration. The TAC modules as discussed in section 3.5.2 should be set to appropriate ranges. For the DDL the range should be set to 100 ns with respect to the maximum signal propagation time, as described in section 3.4.2. For the TOF measurements the range of the TAC should be set to cover the expectation value. For the given setups with quite short distances between the two detector units, as discussed in this chapter, the range was usually set to 50 ns. The delays should be chosen in a way that the mean timing signal is positioned in the centre of the set TAC range, whereby possible non-linearity in the borders of the range are excluded.

If everything is tuned appropriately, one can use the fast pulser signal for calibration purposes. The DDL are read out only one sided, i.e. with the other end being terminated. Feeding the pulser signal on the terminated end one gets the maximum signal propagation time whereas feeding the pulser signal directly on the read out end of the DDL, one gets the minimum signal propagation time. Given the intrinsic maximum propagation time of 68 ns/100 mm and 60 ns/80 mm of the DDL, the spatial resolution can be calibrated.

A similar method can be applied to the TOF signal. Feeding the timing front-end electronics of both detector units with a split pulser signal, delivered over calibrated cables of equal delay, one gets a zero timing signal. Afterwards one can apply a known and calibrated delay to feed the second unit of the detector. Thus one gets a precise calibration for the TOF signal.

5.2. Very first measurements

In the very beginning of the development phase first measurements aimed at a more detailed understanding and classification of the detector's capability. Even though the general design of the first prototype was fixed, parts of the mechanical structure

were still under manufacturing and thus substituted by provisional solutions. This section discusses a few out of nearly 40 measurements, whose aim was to get a rough idea about the spatial and timing resolution as well as the tracking capabilities.

5.2.1. Solar cell array as calorimetric stopper and a first tracking test

As mentioned before, the MCP suffers from a high pulse shot noise, especially in the early beginnings with the first testbed, which only reached an absolute pressure of roughly $3 \cdot 10^{-6}$ mbar. To compensate for this, a solar cell array was placed behind the two detector units as an additional trigger. Besides, it could be used as a calorimeter. 32 single solar cells type PDB-C609 by API[1] were used, where two neighbouring cells were connected in *OR*-logic, resulting in 16 channels. Those were fed to additional ADC modules, after being amplified and shaped by a CFD. Figure A.14 shows a raw, uncalibrated energy spectrum for each channel of the solar cell array, taken with a triple alpha source. One can clearly see huge differences. A calibration and offset matrix was built in order to correct for these differences as much as possible.

Figure 5.4(a) shows a schematic sketch of the array including the cell pairing and picture 5.4(b) shows the array mounted on the optical bench of the first testbed, as described in section 4.3.1. Its whole active area is $50 \cdot 70\,\mathrm{mm}^2$, being 30 mm smaller per axis than the active area of the detector. It was mounted in a way that the long and short axis of both active areas, i.e. the ones of the detectors and the array, were parallel and the centre spots were aligned. Thus, if an ion is detected in the array, it must have passed both detectors. Advantageous, the solar cells exhibit very little noise, if electrically isolated from the rest of the electronics of the setup. Therefore, the array was used as global gate for the DAQ. The DAQ itself was only triggered, if the MCP of both units fired, i.e. a TOF signal was measured.

Given this setup, a very first test of the tracking capabilities was performed. A mask of 32 mm outer radius with a 12 mm diameter centre hole, surrounded by four 3 mm and four 6 mm diameter holes was built. The distances of the source, the units and the solar cell array were chosen in a way that the complete mask was illuminated and projected completely on the conversion foil of the first unit. Though only an inner rectangular part of the mask was projected on or rather seen by the solar cells. Taking the above mentioned DAQ conditions, only those parts of the mask seen by the solar cell array should be measured by the first unit, even though it sees the whole mask.

A result of such a measurement can be seen in figure 5.5, which shows the expected pattern. In the lower right corner of the plot one can see a sketch of the mask, including the part seen by the solar cell array marked by a red frame. Thus a very first showcase of the tracking capabilities is given.

[1] Advanced Photonix, Inc. 2925 Boardwalk Ann Arbor, MI 48104, USA

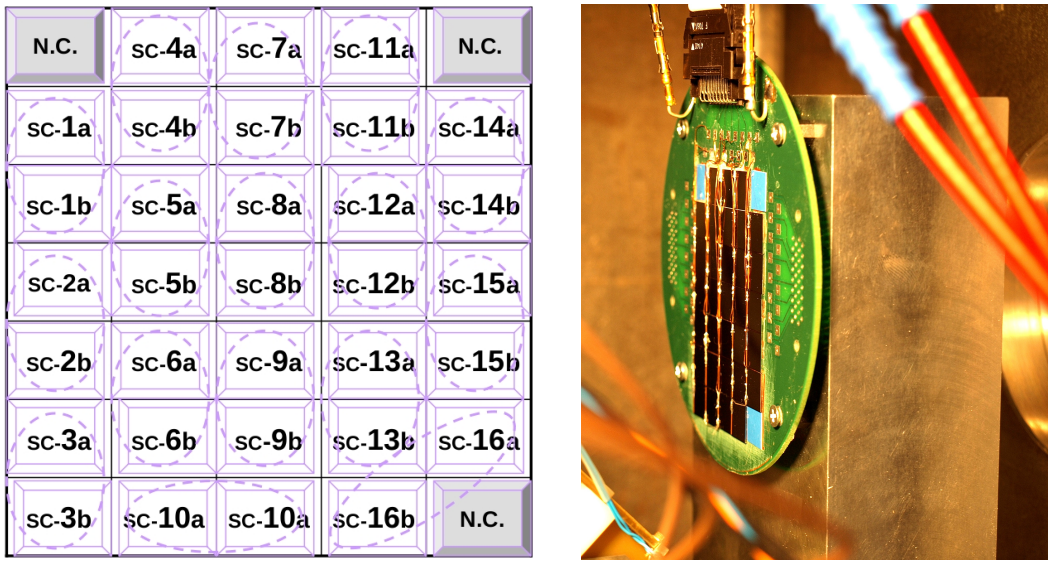

(a) Schematic sketch.

(b) Picture of mounted array.

Figure 5.4.: Schematic sketch and a picture of the mounted solar cell array. Every two neighbouring cells were combined to one channel, wired in *OR*-logic.

5.2.2. Strongly collimated ^{241}Am source for spatial and timing resolution tests

After a first proof of principle had been provided, tests with a strongly collimated 4 MBq ^{241}Am source were performed. Thus a pencil beam could be simulated, which was used to determine more precisely the spatial and timing resolution of the detector. The collimator itself consisted of a hollow needle of 6 mm diameter and a length of 8 cm. The exit of the collimator was placed 1.3 cm in front of the conversion foil of the first detector unit. As conversion foils aluminium coated polycarbonate was used, as described in section 3.2.2. The distance between the conversion foils of the two units was 20 cm. Afterwards, the solar cell array was placed as close as possible behind the second unit.

A simulation of the projection of the collimated ion beam upon each conversion foil was conducted with the program package SIMION 8 [Ser12] by SIS[2]. Results of this simulation can be seen in figure A.11, which shows the raw simulation output. Afterwards it has been registered with the measurement in terms of sizes and absolute counts.

One has to keep in mind that the simulation is the ideal distribution on the conversion foil perpendicular to the ion beam axis and the measured distribution is the one at the detector head, i.e. the distribution of the SE after passing the electrostatic

[2]Scientific Instrument Services, 1027 Old York Rd. Ringoes NJ 08551-1054, USA

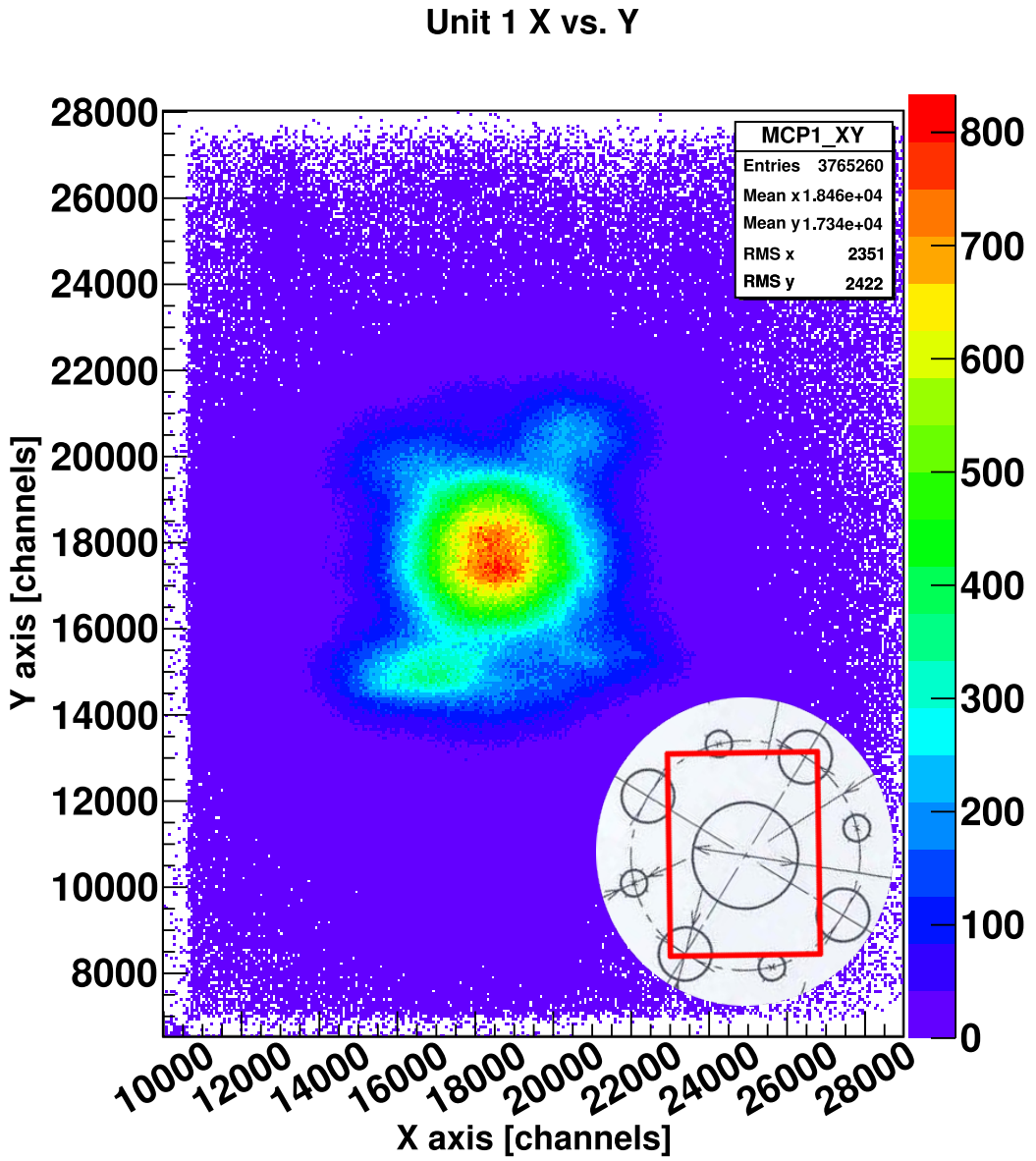

Figure 5.5.: First tracking test with a round mask before and a solar cell array behind the detector. In the lower right corner one can see the mask being used. The red frame marks the part of the mask which is seen by the solar cell array functioning as global gate for the DAQ. Thus only this framed part of the mask is measured by the first unit, even though the mask is completely projected on it.

top-assembly. Thus one gets an idea of the influence of the electrostatic top-assembly on the spatial resolution of the detector.

Figure 5.6 shows the measured hit patterns of both units, while figure 5.7 shows the corresponding axis projections including the ones for the simulation. Table 5.1 summarises the simulated and measured resolutions, expressed as the FWHM of a Gaussian fit. The fits, i.e. the errors, are precise to at least an order of a 1/100 mm. Since the detector should have a precision around one millimetre, the values were rounded up to the first decimal place, making the errors redundant in this case.

Table 5.1.: Measured resolutions (expressed as the FWHM of a Gaussian fit) of the distributions according to figure 5.7. The values were rounded up to the first decimal place.

		X axis resolution [mm]	Y axis resolution [mm]
Unit 1	simulated	8.0	
	experimental	14.7	11.9
Unit 2	simulated	11.5	
	experimental	14.3	13.5

As one can see, the deviation between the simulated reference values and the measured ones is smaller for the second unit than for the first unit. A possible explanation of this effect is a strong variance in the noise of both units during the measurements, which can be assumed from figure 5.6 when comparing the Z scales. Even though the DAQ was gated by the solar cell array and a common timing signal was taken as global trigger, the first unit suffered from a lot more noise. This was probably caused by a weak shielding of the strong source and a thin wall thickness of the collimator needle, which resulted in additional bremsstrahlung. Unfortunately, the MCP is sensitive to this kind of radiation and consequentially, the first unit was exposed to a much larger amount of it.

For both units the deviation between the reference and measured values is larger for the X than for the Y axis. Focusing on the mechanical design of the detector, the only logical origin of this effect is the helical ground winding as the only part not being symmetrical in both axes. Later tests investigated this effect and proved the assumption to be correct, as discussed in section 5.3.2.

Concerning the timing resolution a similar measurement has been performed. A delay was used for the timing signal of the second detector unit, i.e. the stop signal of the TOF. To get an estimate and calibration, the stop signal was once delayed by -4 ns and once by $+4$ ns with respect to an offset measurement. The same was done for the TOF between the first detector unit and the solar cell array, which was connected in *OR* logic. As values for the delays -48 ns and $+48$ ns were chosen with respect to the larger absolute TOF. The FWHM as measure for the timing resolution 1.07 ± 0.2 ns could be achieved for the TOF between the two detector units and 16.8 ± 0.1 ns for

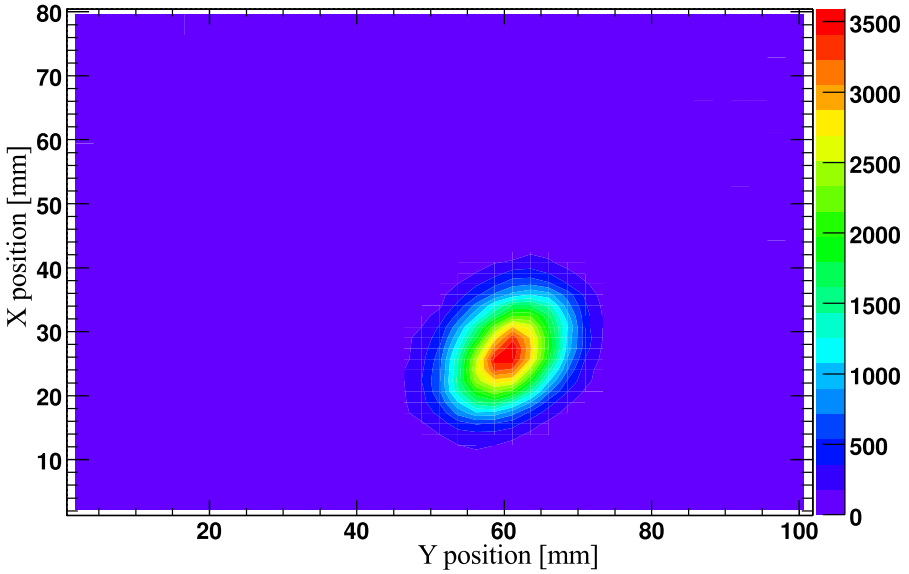

(a) Hit pattern of unit one.

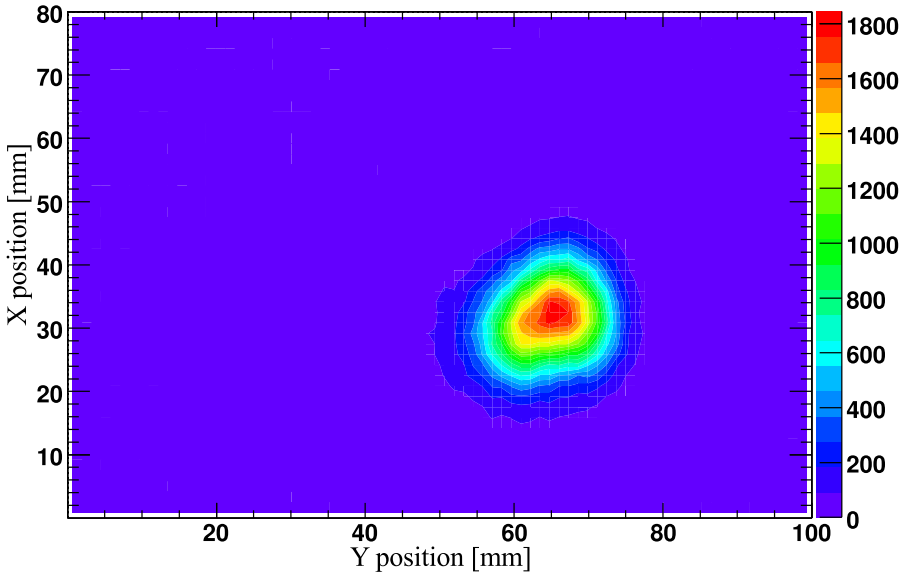

(b) Hit pattern of unit two.

Figure 5.6.: Measured profiles of detector unit one and two of an alpha source, collimated by a 6 mm hollow needle of 8 cm length.

the TOF between the first unit and the solar cell array. Both measurements can be seen in figure 5.8.

Both values do not match the desired specifications. However, for the latter the timing resolution of the solar cells can partly be held liable, which convolves with the timing resolution of the first unit. An overview of the timing resolution of the solar cell array is given in figure A.12. Another issue might be the usage of the first revision timing amplifiers, which had worse specifications compared to the ones later used, as discussed in section 4.1. Afterwards tests have been focused on a better timing resolution, which could be proven to fulfil the desired specifications, as discussed in section 5.3.1.

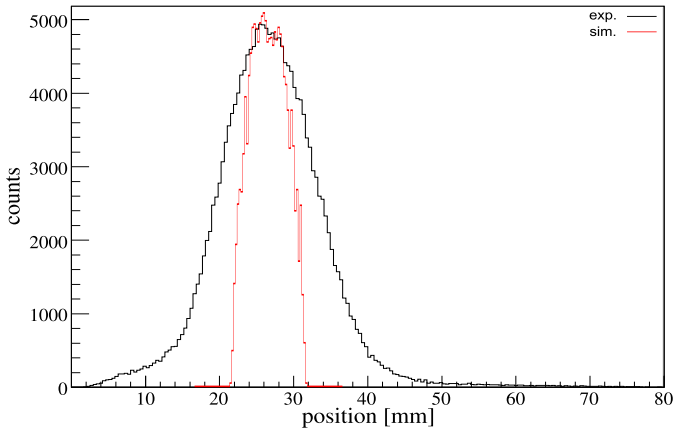

(a) X axis distribution of unit one.

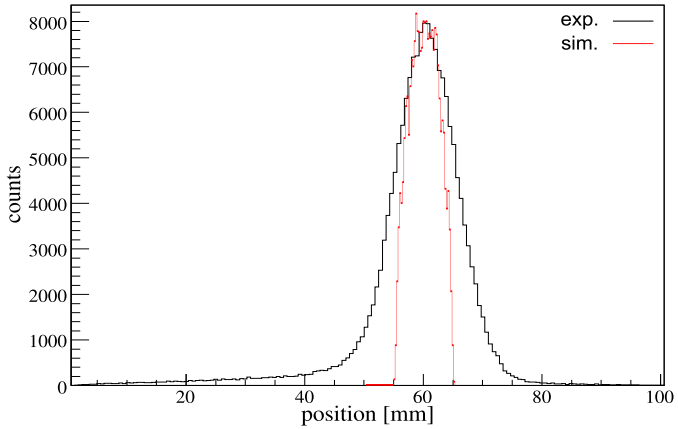

(b) Y axis distribution of unit one.

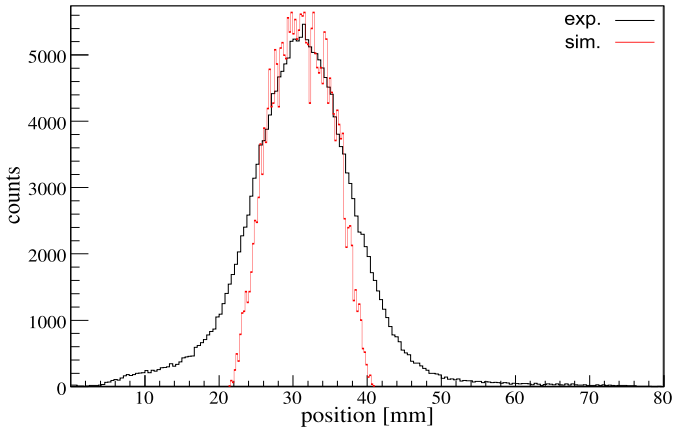

(c) X axis distribution of unit two.

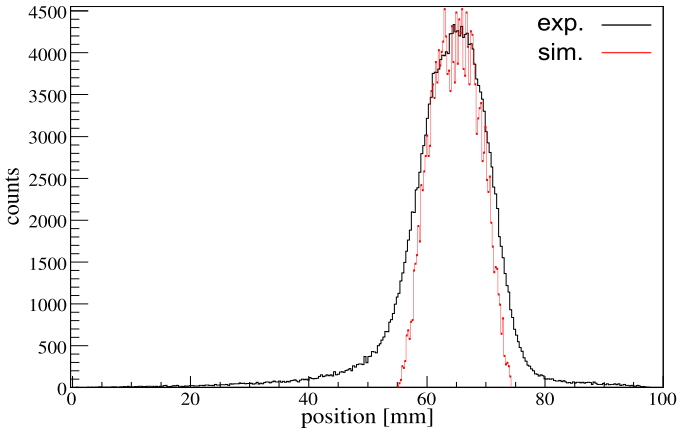

(d) Y axis distribution of unit two.

Figure 5.7.: Measured (marked black) and simulated (marked red) axis projections of both units, corresponding to figure 5.6.

5.2.3. Non-symmetrical masks to investigate the mapping of the electrostatic top-assembly

For a better understanding of the mapping characteristics of the electrostatic top-assembly, non-symmetrical masks were used in later tests. The most used and most flexible was shortly introduced in section 3.4.2 (see figure 3.11).

A very first mask functioned primarily as a showcase and was designed in the abbreviation of the institute, namely *IKP*. Picture A.13 shows this mask, made of tungsten, mounted on a frame, which could be fixed to a sledge for the optical bench used in the first test chamber. The bottom line of the writing is parallel to the vertical, right edge of the conversion foil in direction of beam, i.e. it is parallel to the Y axis. Its centre is aligned with the centre of the conversion foil. The width of the cuts of the letters is 5 mm, as well as the distance between the letters.

Due to the asymmetry of the mask, the orientation of the readout channels could be checked and corrected, when necessary. The mask itself was placed as near as possible in front of the first unit. The uncollimated source was mounted in the source-pod, as described in section 4.3.1. The measured projections can be seen in figure 5.9. Of course, unit one shows a more compact projection than unit two. Beside this, it is striking that the writing is deformed from the letter I to P. This becomes especially obvious when calculating the projection in between both detector units. Since the DAQ functions on an event-by-event basis, each two corresponding hit points measured by the detector units can be combined by a straight line. Now one can calculate offline the projection of every desired position along these combinations. Figure 5.10 shows a result of such a calculation for the position midway between the two detector units.

Analysing this projection, one can make a difference in the deformation between both axes. For the Y axis fractions, there seems to be no noteworthy deformation. Looking at the X axis fractions on the other hand, the deformation seems to become stronger, the larger the distance from the detector head gets, i.e. it is stronger for the letter P than for I. This behaviour is another hint to the helical ground winding being the origin of this effect. In section 5.3.2 this effect is investigated more thoroughly.

5.3. Specification measurements with the first prototype

After the first prototype was developed to the final revision, a series of different tests have been performed in order to characterise the detector more precisely. This section will discuss three particular measurements out of nearly 30 performed, namely a test with a triple alpha source to determine and improve the timing resolution, a test with a multi hole mask to understand the spatial resolution issue more clearly and a test with a spontaneous fission source to estimate the efficiency of the detector.

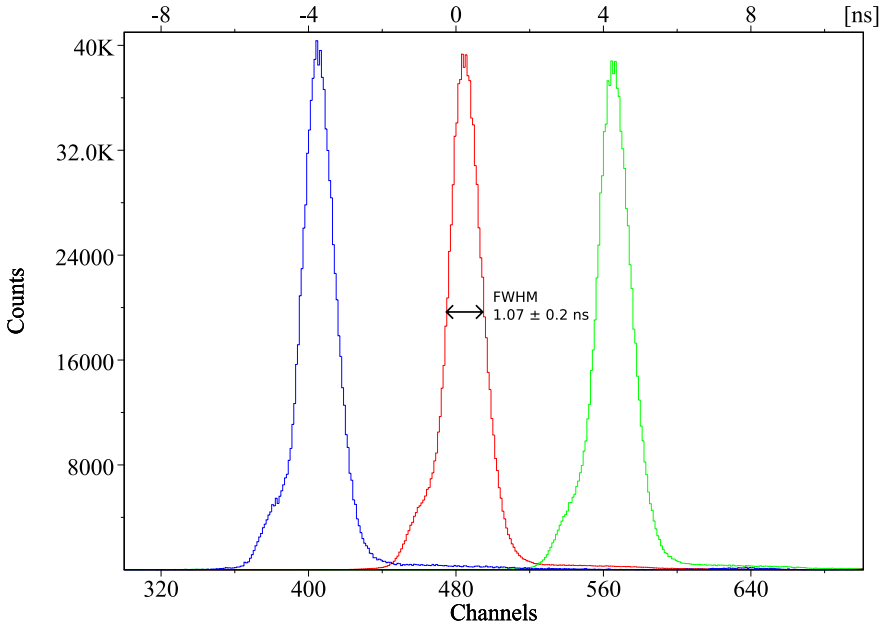

(a) Timing resolution for the TOF between unit one and two for delays of −4 ns, 0 ns and +4 ns.

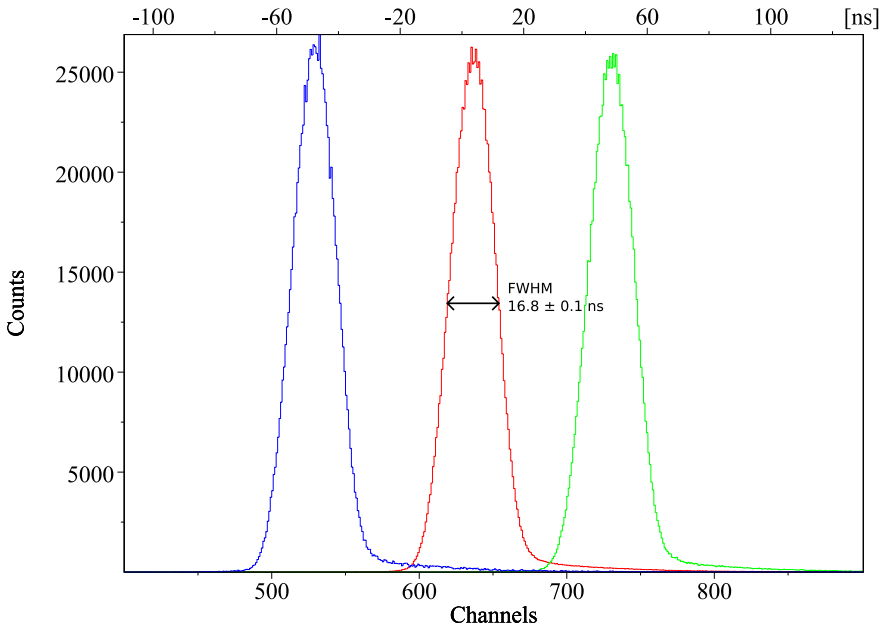

(b) Timing resolution for the TOF between unit one and the solar cell array for delays of −48 ns, 0 ns and +48 ns.

Figure 5.8.: Timing resolution for the TOF once between unit one and two and once between unit one and the solar cell array. In both cases, a delay was used for the stop signal.

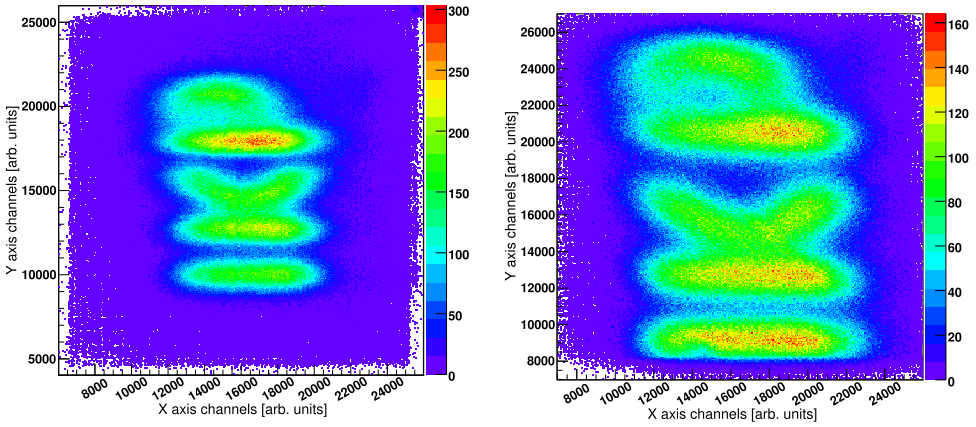

(a) Hit pattern of unit one.

(b) Hit pattern of unit two.

Figure 5.9.: Hit patterns measured by both units of a *IKP* mask. Of course, figure 5.9(a) shows a more compact hit pattern than figure 5.9(b), due to the divergence of the beam.

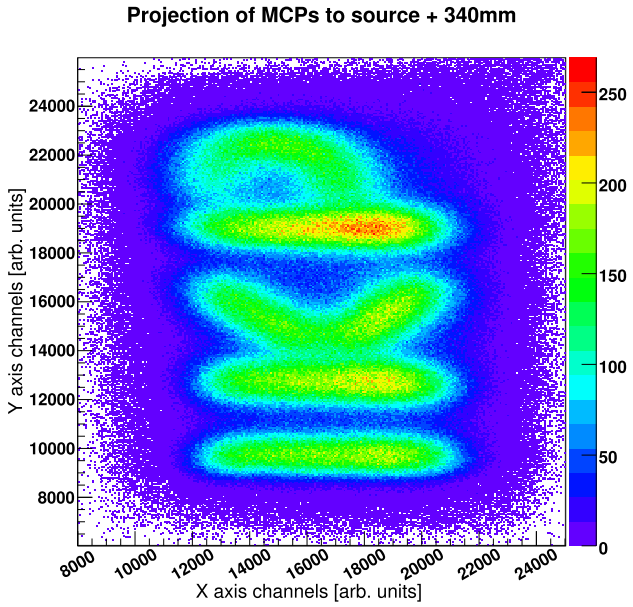

Figure 5.10.: Calculated projection of a mask showing the institute abbreviation, midway between the two detector units. The middle position was situated 340 mm downbeams of the source.

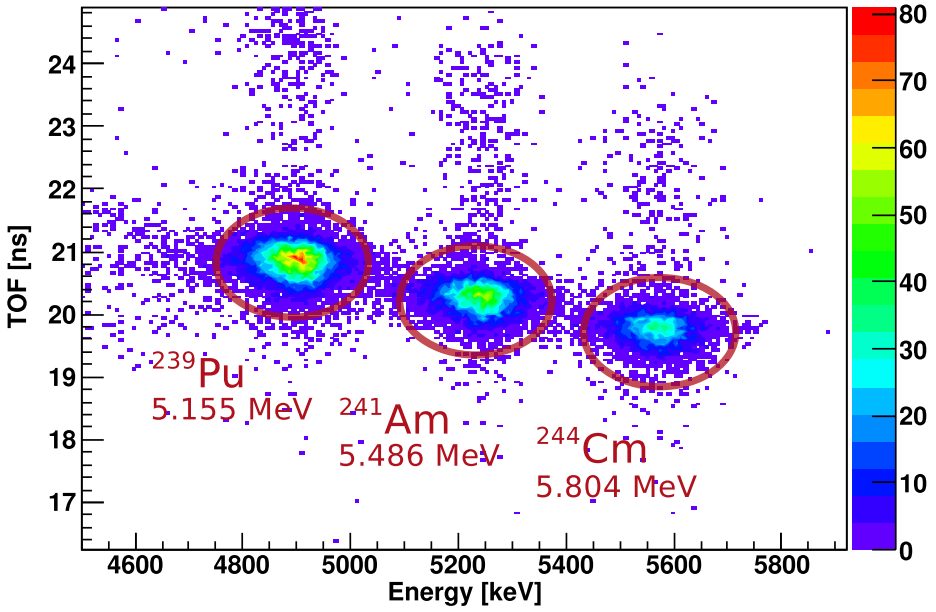

Figure 5.11.: Plot of the TOF versus TKE for a triple alpha source. The individual emitters are marked in red. Note that the measured energies differ roughly around 200 – 300 keV from the literature values. This is due to the two relatively thick, gold coated Mylar conversion foils of the detector units.

5.3.1. Tagging of a triple alpha source and improvement of the timing resolution

For most of the tests performed during this characterisation phase, a triple alpha source was used. It consists of ^{239}Pu, ^{241}Am and ^{244}Cm, each emitting a major part of its alpha radiation at different energies and thus providing a cocktail beam, ideally suited to test the detector. Together with the solar cell array as stopping calorimeter, one can completely tag the individual emitters very precisely via a plot of the TOF versus the TKE. Such a plot can be seen in figure 5.11.

One can clearly see a difference between the literature values given with the red markers in figure 5.11 and the measured values. The calibration of the solar cells was performed without the detector units obstructing the ions. Hence, this effect must be caused by the two relatively thick, gold coated Mylar conversion foils being passed by the ions (see 3.2.2). Table 5.2 summarises the theoretical energies after an alpha particle with an energy given by the literature values passed the two conversion foils and the measured ones. The measured values are consistently about 20 keV below the theoretical ones.

One explanation might be the absence of the meshes in the theoretical calculation. Since the meshes are of a thickness which stops the alphas completely an alpha particle either passes a mesh or not. Neglecting edge effects in the wires of the meshes

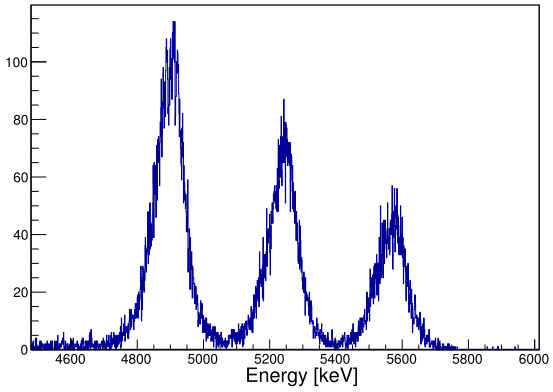

Figure 5.12.: Plot of the summarised TKE of a triple alpha source, as projected from figure 5.11. All channels of the solar cells array are summarised.

justifies their absence in the theoretical calculation. Thus a more credible explanation is the divergence of the ion beam from the point like source to the finite solar cells array, resulting in relatively larger foil thicknesses, the more divergent a particle passed it. The theoretical calculation instead assumes every ion passing the foil perpendicularly.

Table 5.2.: Theoretical and measured energies of a triple alpha source after passing the two gold coated Mylar conversion foils of the detector. The measured values are consistently below the theoretical ones, which is caused by the divergence of the beam and therewith a non perpendicular penetration of the foils, as assumed for the theoretical calculation.

Isotope	Theoretical Value [keV]	Measured Value [keV]
^{239}Pu	4916.4	4895.0(5)
^{241}Am	5256.1	5239.0(6)
^{244}Cm	5584.6	5564.8(7)

Since the solar cell array only functions as gate and coarse calorimetric stopper, this short discussion of the divergence between literature and measured values of the energies is sufficient in this case. The resolution is still sufficient to separate the different emitters, as seen in figure 5.12.

The data structure allows to set certain cuts and use these as coincidence condition, as described in section 5.1.2. Figure 5.13(a) shows the projected TOF of figure 5.11. It is obvious that the timing resolution is not sufficient to separate the single emitters. If one cuts polynomials similar to the red spheres in figure 5.11, marking the emitters, one can separately project the TOF for each single emitter. Such a plot is seen in figure 5.13(b), which shows all cut projections in one plot. Logically, the emitter with

the lowest energy possesses the longest TOF and vice versa. The red lines mark Gaussian fits to the single distributions.

Table 5.3.: Timing resolution for individual emitters of a triple source, expressed as FWHM of a Gaussian fit. The values correspond to the fits in figure 5.13(b).

Isotope	FWHM of Gauss. fit [ps]
^{239}Pu	539.4(49)
^{241}Am	507.9(56)
^{244}Cm	495.9(69)

Table 5.3 sums up the timing resolutions of the detector for each emitter, expressed as FWHM of the Gaussian fit. Unfortunately, the values miss the desired specifications shortly by circa 100 ps. At that time, all front end electronics were developed to their final revision. However, the electronic modules from the DAQ were still to be replaced. Especially the old fixed gain fast timing amplifiers model *Ortec A3G12* had to be replaced with models *Ortec 9309-4* and the constant fraction discriminators model *Ortec 584* had to be replaced with faster models *Ortec 935*.

After these modules had been replaced, another measurement series with the triple alpha source was performed. The old fast timing amplifiers were replaced on an interim basis by 4 GHz ones with a typical fixed gain of factor 11.2 from Surface Concept [Sur13]. Furthermore one speculation aimed at the XiA based ADCs of the back-end DAQ. It was observed that these modules are sensitive to an equal arrival time of the TAC signals, as described in section 3.5.2. Thus an in-house developed multi channel analyser has been used instead.

Given this combination and the same experimental setup, the timing resolutions improved a lot. Picture 5.14 shows a screen shot of a TOF measurement with these replaced back-end electronics. The according measurement forced a high resolution by setting highest possible thresholds to reduce the noise as much as possible and placing the detector units at a maximum distance of 31 cm to maximise the time resolving power. The drawback of such a setup is the very low count-rate of roughly 1 Hz. However, for the ^{241}Am TOF a FWHM of 209(61) ps could be reached, which fulfils the specifications by more than a factor of 2. It is even sufficient to clearly separate the emitters just by their TOF without consulting the energy information from the solar cell array.

Given these findings, several standard measurements with realistic thresholds were performed. As expected, the measured values differ clearly from the above mentioned ones. Figure 5.15 shows one exemplary measurement. The measured resolutions of all measurements are given in table 5.4, so that mean values for the TOF resolution for each emitter could be specified. Even with realistic settings the timing resolution is within the specifications and still sufficient to separate the emitters from the triple alpha source without the energy information. Moreover, the data was taken for a fully divergent beam, which indicates that for a centralised or spatially

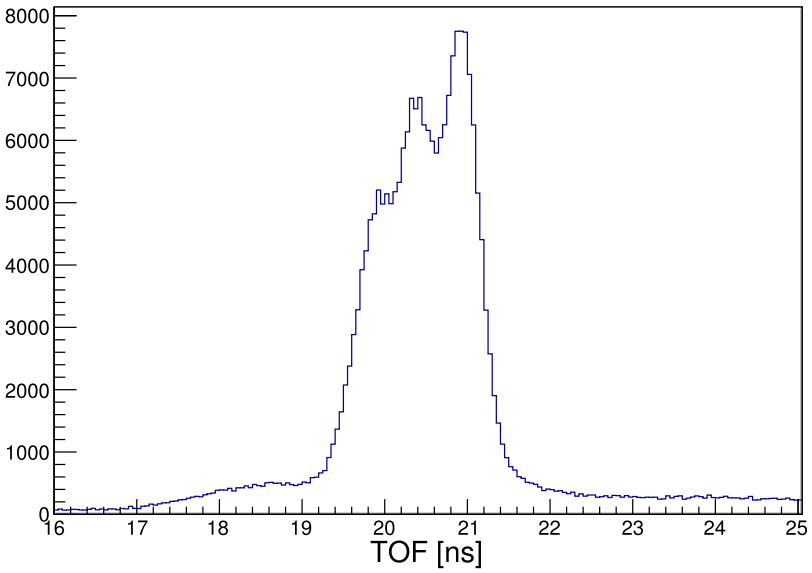

(a) TOF without cuts.

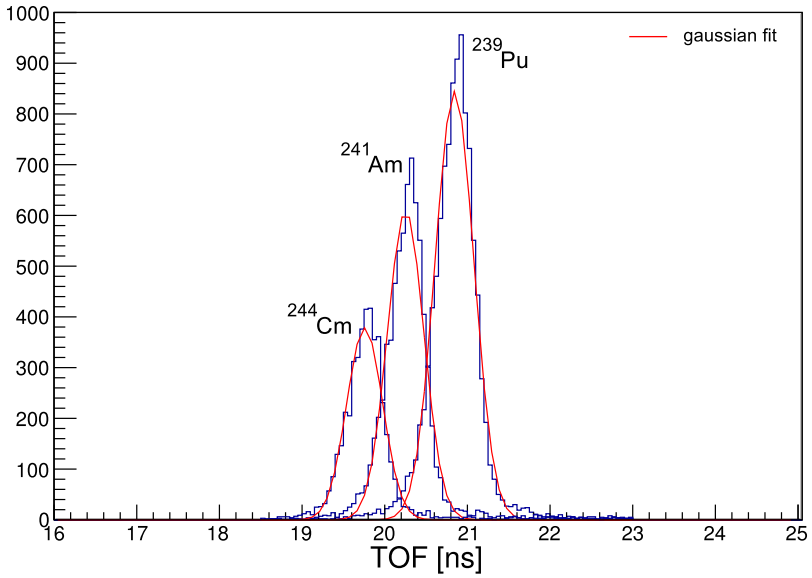

(b) TOF with cuts on the individual emitters.

Figure 5.13.: TOF of a triple alpha source without cuts (as projected from figure 5.11) and with cuts on each individual emitter.

corrected hit pattern the resolution can only become better. Unfortunately, this was not possible with the used single channel multi channel analyser, since no list mode data was taken.

A practical consequence of this measurement is an investigation of the internal structure of the source. Normally these kind of sources are produced in a way, that a solution with the radioactive isotope is evaporated on a source holder. Thereby the layers of the different emitters are stacked upon each other. Neglecting a possible energy dependence, the timing resolutions should be of the same order for each emitter. The differences might be caused by the layered structure of the source. Looking on the surface of the source, the alpha particles of the emitter in the first layer should have the best resolution, while the alpha particles of the emitter in the last layer should have the worst resolution.

Thereby the resolution is a measure for the energy and thus velocity straggling the alpha particles undergo when penetrating (or in case of the first layer, not penetrating) the other layers. Hence, the first layer should include the ^{241}Am, the second or middle layer the ^{244}Cm and the last layer the ^{239}Pu.

Table 5.4.: Timing resolutions of a set of measurements with a triple alpha source with new and replaced back-end electronics.

Isotope	FWHM of Gauss. fit [ps]	Mean value [ps]
^{239}Pu	374(28)†	366(27)
	326(21)	
	353(16)	
	390(54)	
	389(14)	
^{241}Am	306(35)†	280(31)
	266(15)	
	249(66)	
	284(10)	
	297(28)	
^{244}Cm	321(47)†	303(32)
	215(26)	
	327(12)	
	336(37)	
	314(37)	

†Values corresponding to figure 5.15.

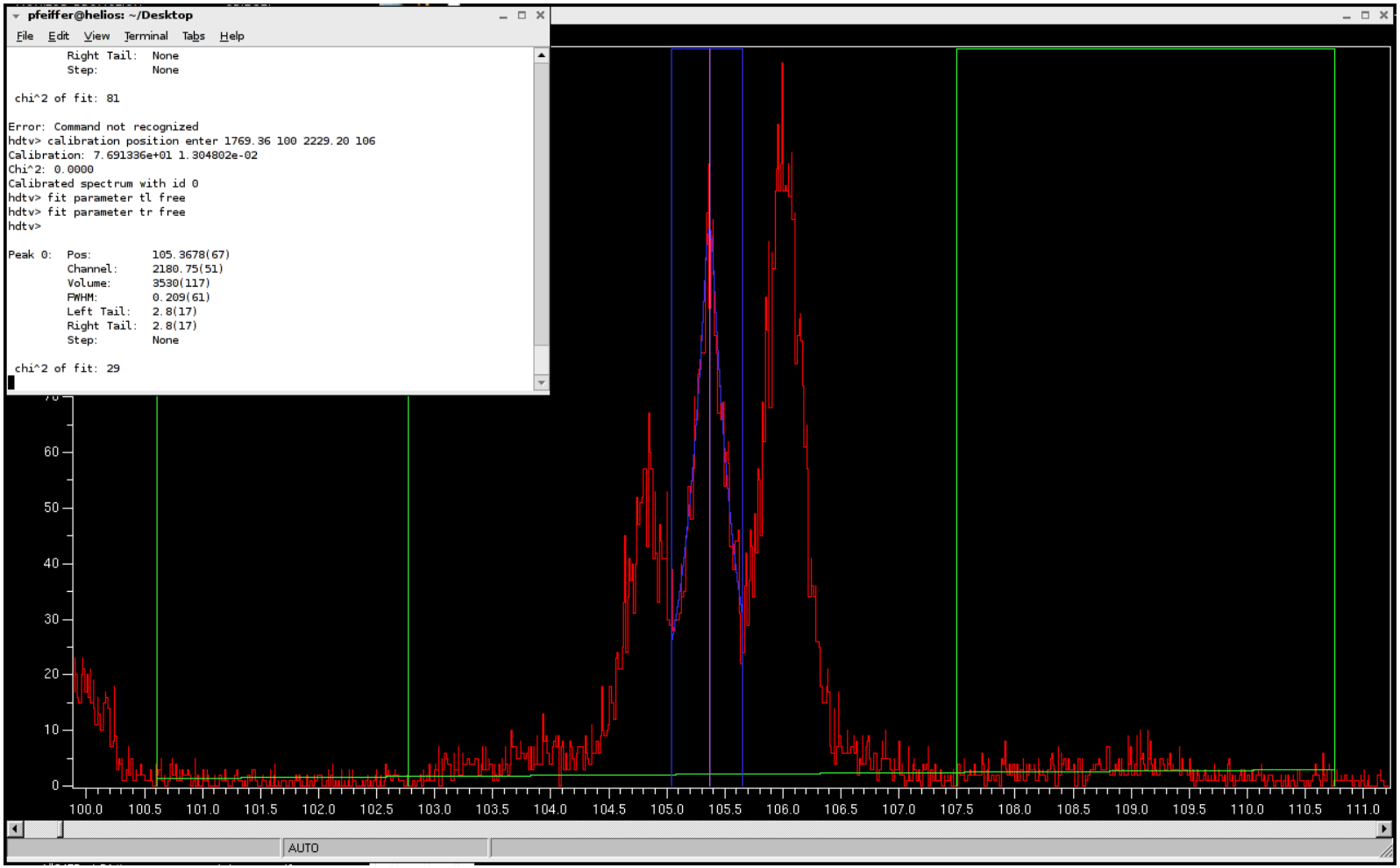

Figure 5.14.: Screen shot of the ungated TOF for a triple alpha source with new back-end electronics, especially new or replaced fast timing amplifiers, constant fraction discriminators and ADCs.

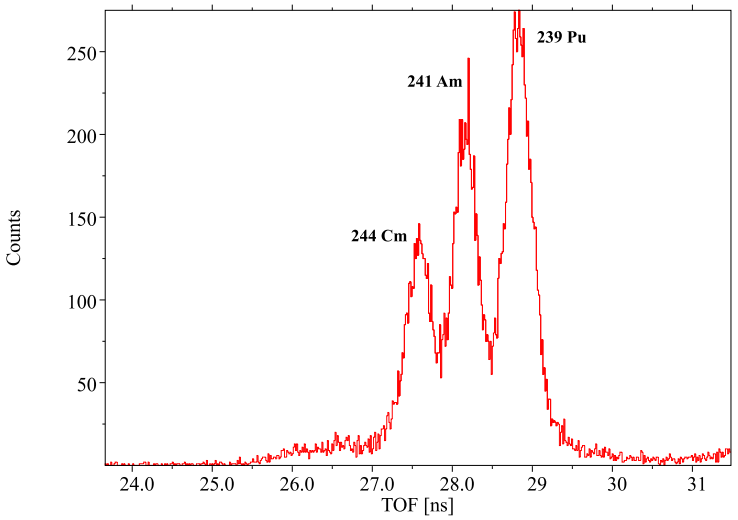

Figure 5.15.: Ungated TOF for a triple alpha source with new and replaced back-end electronics. This measurement is exemplary for a set of similar measurements being performed.

5.3.2. Investigation of the spatial resolution with a multi hole mask

A non uniform spatial resolution became apparent in a very early test (see section 5.2), so this issue was more closely investigated with a dedicated mask. For this purpose, a mask with several holes of equal size and uniform distances was built, as shown in figure 3.11. It was placed in between a 4 MBq ^{241}Am source and the first detector unit. The outer ring of holes was taped to focus on the spatial resolution in the central area of the detector, where most ions will pass in a possible future slowed down beam experiment. Figure 5.16 shows a plot of the measured mask projection of the first unit. One can see the $3x5$ matrix of the mask holes, even though the central $3x3$ matrix exhibits the most statistics. At first glance the plot strengthens the assumption of a worse X axis resolution for higher Y axis positions.

For a systematical investigation of the spatial resolution, one can classify the projected holes in rows and columns. A calculation of the centre positions for each row and column has been done upon the given geometry. As an example, the columns marked in figure 5.16 are at 27 mm (red), 43 mm (green) and 57 mm (blue) with respect to the X axis. After this categorisation, one can project the X and Y axis components of each spot and apply a Gaussian fit on these projections. Thus a measure for the spatial resolution is given for a larger area of the detector. The FWHM of these fits are summarised in table A.2 for unit one and table A.3 for unit 2. For the second unit the lower row had to be refused, since it was cut off by the edge of the conversion foil.

Figures 5.17 plot the resolutions for unit one. As one can clearly see in plot 5.17(b), for the Y axis projections, the resolution is quite stable for the examined area. On

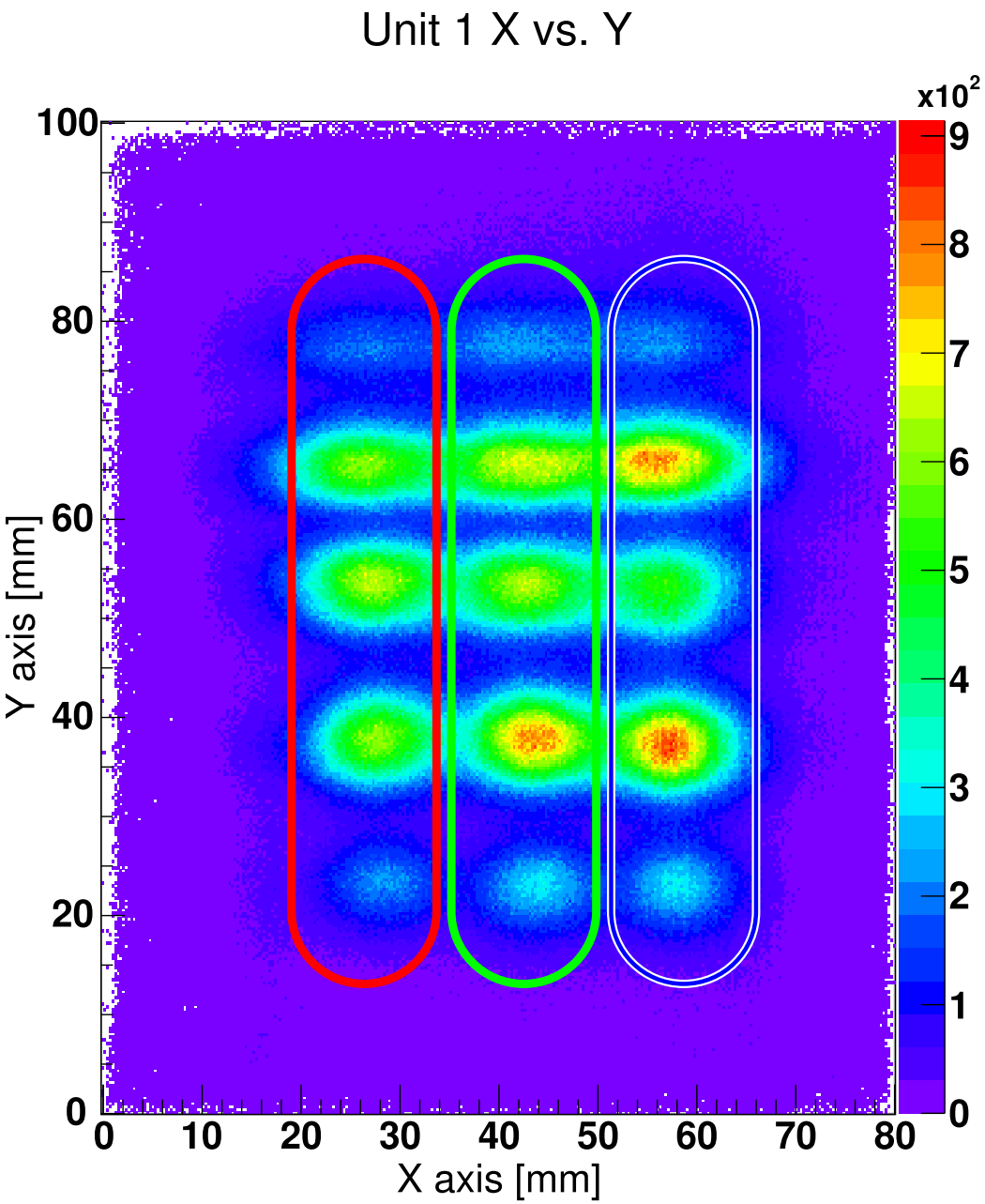

Figure 5.16.: Measured projection of a multi hole mask of the first unit. The markers correspond to figures 5.17.

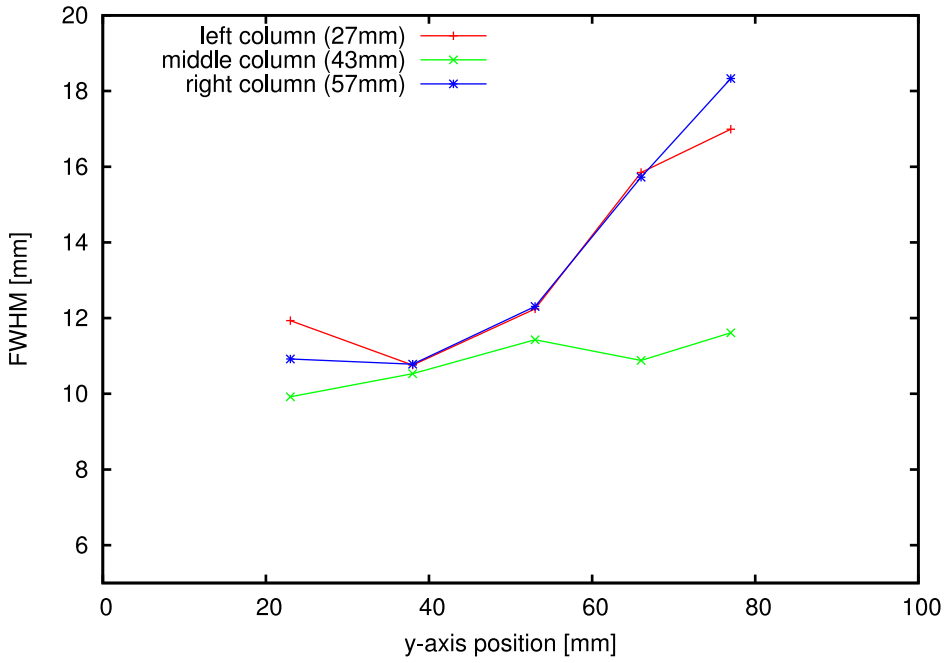

(a) X axis projected resolutions.

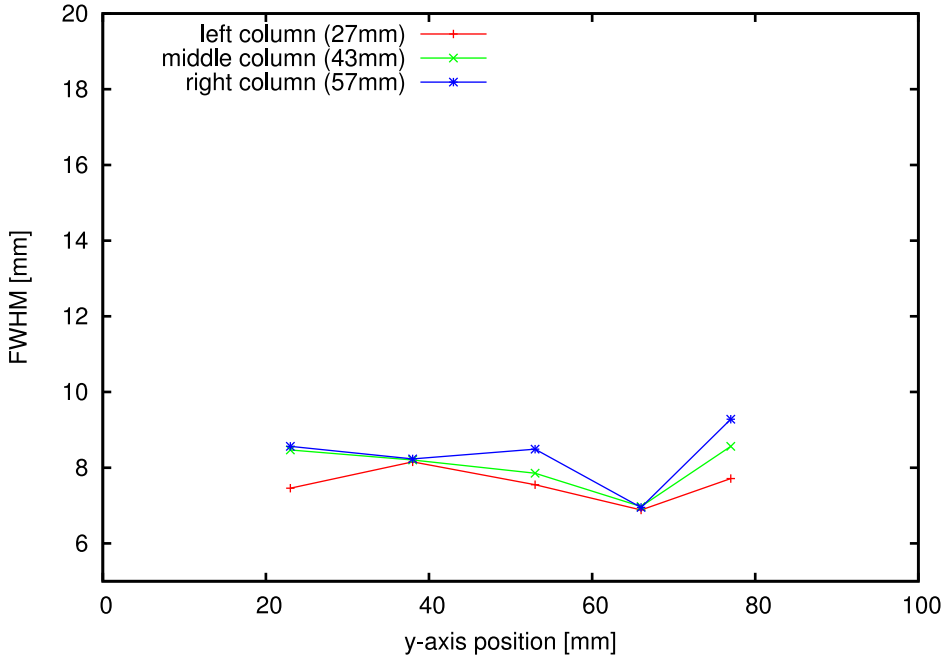

(b) Y axis projected resolutions.

Figure 5.17.: Projected axis resolutions of a multi hole mask for the first unit. The colour pattern of the curves correspond to the markers in figure 5.16, i.e. the X axis position of the spots.

the other hand, the X axis resolution is rather bad and gets worse, the higher the Y axis value gets. This effect can especially be observed at the side areas, i.e. the left and right columns of the projected hole matrix.

Assuming the helical ground winding as cause of this effect, there are two possible explanations emphasising two possible regions where the deflection can take place. One has to keep in mind that the wires are parallel to the Y axis. Thus the SE gets deflected in the X axis, while not being deflected in the Y axis in a first order. Scenario A is a stronger deflection during the acceleration of the SE between the conversion foil and the ground winding. Scenario B is a stronger deflection during the reflection of the SE at the reflecting module.

For scenario A the X axis resolution should be worse for lower Y axis values, as the flight path between conversion and reflecting module is larger than for higher Y axis values and therewith the absolute deflection. The situation for scenario B is contrary and agrees with the observations. Thus it is more likely that the major deflection from the ideal path of the SE is caused at the reflecting module. For a closer understanding of this phenomenon, a simulation of the deflection of SE at the grid wire structure of the reflecting module was performed. For the simulation the SIMION code was used [Ser12]. Figure 5.18 shows the corresponding result, where the white diamonds correspond to the left axis and the black diamonds to the right axis. The deflection is given in degrees with respect to an ideal 90° reflection of the SE, i.e. the lead from reflecting module to detector head. The penetration clearance on the other hand is a measure for the closest reachable distance between the reflecting grid and the SE for a given electron energy.

As one can see, the closer the electrons get to the grid wires, the higher their energy gets. As a side effect, the SE are to be affected by the microscopic, cushion shaped field disturbances of the grid stitches. The deflection becomes stronger in this case. Instead, up to an energy of roughly 3200 – 3300 eV of the SE and a fixed 4 kV negative potential at the grid, the SE seem not to be affected by a macroscopic, homogeneous field induced by the grid. Thereby the deflection seems to be roughly stable. Thus one should not exceed a certain potential difference between accelerating and reflecting voltage.

A similar simulation for the influence of the helical ground winding was performed by KOSEV ET AL [Kos08b]. Figure 5.19 shows a copy from the original publication. It is shown that for a varying pitch distance of a helical ground winding the Y axis resolution is quite constant, whether the SE are deflected at the edge or the middle of the reflecting module. The X axis resolution on the other hand gets worse with an increasing pitch distance. This is especially the case for SE deflected at the edge or non-centrally of the reflecting module. This simulated behaviour is reproduced by the measurement presented before, which becomes especially visible in figures 5.17.

The options left are to minimise the pitch distance or to substitute the helical ground winding by a mesh. Both options result in more material obstructing the beam. While the first option is not apt to reach X resolutions comparable to those of the Y axis projections, this might be possible with the latter one. Thus the latter option was chosen for the design of the second prototype, as described in section 4.2.

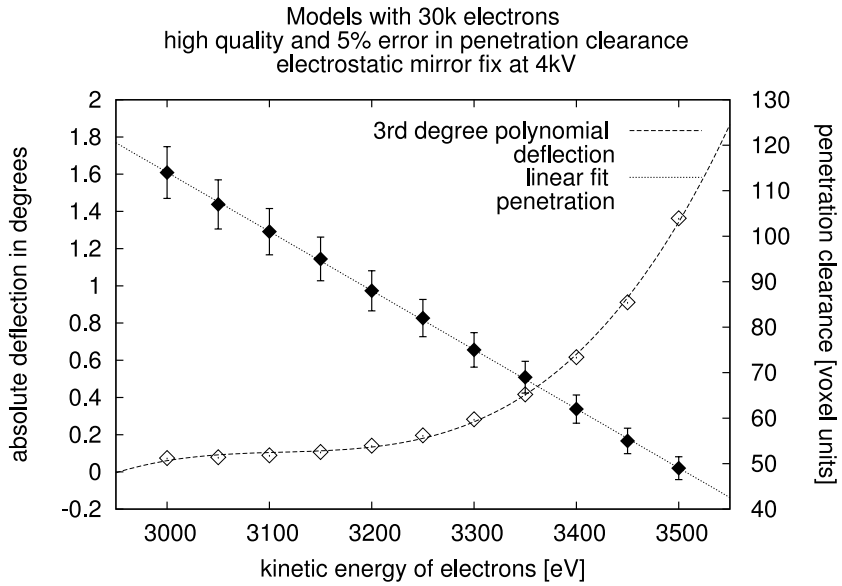

Figure 5.18.: Simulation of the SE deflection at the reflecting mesh. The left axis deflection (white diamonds) states the deflection in degrees with respect to an ideal 90° reflection of the SE . The right axis (black diamonds) is a measure for the closest reachable distance between the grid wires and the SE .

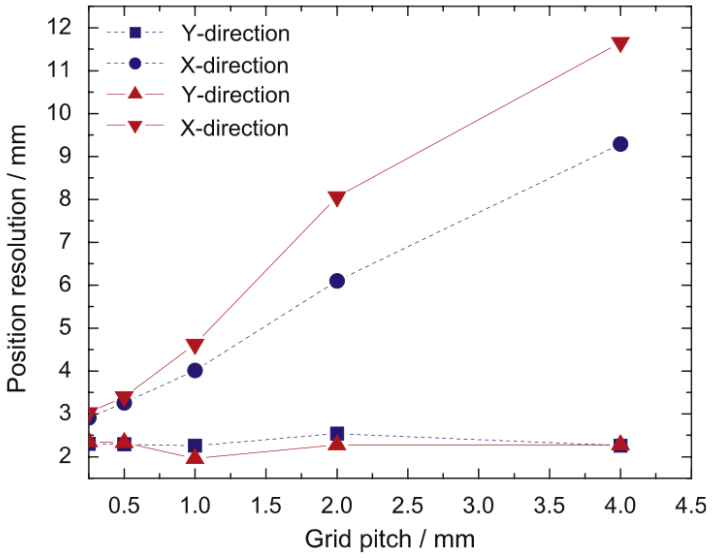

Fig. 5. Calculated position resolution as a function of the grid wires pitch. The dashed line is for particles deflected in the middle of the electrostatic mirror. The solid line is for particles deflected at the edge of the electrostatic mirror. The orientations of *x*- and *y*- axes are indicated in Fig. 2.

Figure 5.19.: Simulation of the SE deflection influence of the helical ground winding, original by [Kos08b]. The description of the original publication has been copied.

5.3.3. Determination of the efficiency with a reference detector and integration in the GSI framework

For a determination of the detector efficiency, the complete setup was moved to GSI. The testbed itself is described in section 4.3.2. Figure A.9 shows a detector unit for this experiment, remounted on a ISO200-CF flange. As reference, a 1 mm thick, 16 + 16 strip DSSSD detector was used as calorimetric stopper. It has a very low intrinsic noise and its amplifier thresholds were well set. Thus this detector is assumed to be 100% efficient. Hence, the ratio between the measured events in the DSSSD and the TOF/BPM detector can be taken as measure for the efficiency of the latter.

Using a triple alpha source in combination with a ^{252}Cf spontaneous fission (SF) source, the efficiency could be determined once for light alpha particles in an energy range of roughly 4.5 – 6.5 MeV and SF products with an energy above 6.5 MeV. Of course, parts of the SF products have energies within the range of the alpha particles, though their portion is statistically insignificant. Especially since the triple alpha source is much stronger with roughly 2.5 kBq in comparison with only about 300 Bq of ^{252}Cf.

For the DAQ, the whole detector including front-end electronics was connected to GSI based back-end electronics. The signals were directly fed to a VME[3] bus multi hit TDC model VX1290A-2eSST by Caen. The DSSSD signals were fed to an VME bus ADC type V785 by the same company. A common DAQ software, the GSI developed GO4 framework was used. Thus this test functioned as a showcase for a smooth integration of the whole system into the given structures at GSI.

Given this setup, several measurements were performed. Due to the low activity of the ^{252}Cf source, the whole test series took several weeks. For the determination of the efficiency, two different scenarios are chosen. If the detector only functions as TOF monitor, conditions for a good event are that both MCP timing signals must occur. If the detector functions both as TOF and BPM, signals must additionally occur in all four DDL spatial channels. The first case will be called soft, while the latter one will be called hard conditions. With the calorimetric information of the DSSSD, these conditions could be applied to both energy ranges, i.e. the efficiency could be determined for low energetic alpha particles and high energetic SF products. Table 5.5 summarises the results of these measurements.

Figure A.15 shows the calibrated DSSSD energy spectrum for the low energetic alpha range (4.5 – 6.5 MeV) and the corresponding TOF spectrum, both for soft conditions. Figure A.16 shows the same for the high energetic FS products range (6.5 MeV). The difference in statistics of both sources is obvious, even though the fourth, highest energetic alpha peak originates from the ^{252}Cf, which decays nearly 97% via the α channel and only just under 3% by SF.

Even though the errors of the efficiencies (given as standard deviation from the mean) are quite high, one can clearly see that the efficiency is much higher for high energetic SF products than for low energetic alpha particles. Especially when applying hard conditions, the efficiency for alphas decreases by nearly a factor of two, while

[3] **V**ERSA**M**odule **E**urocard

Table 5.5.: Measured efficiencies of the detector, both for low energetic alpha particles (4.5 – 6.5 MeV) and high energetic spontaneous fission products (6.5 MeV). For each case the efficiency is given for plain TOF (soft) and combined TOF/BPM (hard) conditions. The errors are given as standard deviation from the mean.

	α particles # of events	SF products # of events
DSSSD	73483(12180)	226(34)
Soft conditions	16688(4851)	166(39)
Efficiency	22.7(76)%	73(21)%
Hard conditions	9730(2596)	160(37)
Efficiency	13.2(42)%	71(20)%

for SF products it does not really differ. Since the detector should be used for heavy ion, slowed down beams, the efficiency is of acceptable order.

5.4. In-beam measurements with the second prototype

After the first prototype was tested and specified, the second prototype was built with the gained knowledge and experience, as described in section 4.2. It has been designed and constructed not only to improve the characteristics of the first prototype, but to specially suit in beam measurements, as well. One major improvement was the completely new testbed, which is discussed in section 4.3.3. This testbed was integrated in a dedicated beamline (see section 4.3.4).

Simultaneously, the Cologne Tandem Van-de-Graaf accelerator was running again for the first time after a long shutdown and maintenance period. Thus very first in beam tests could be performed in order to study the detector response and behaviour under real conditions. This chapter will discuss two sets of measurements within this campaign and will give some general remarks beforehand.

5.4.1. General remarks on the in-beam experiments

Unfortunately, at the beam time period of the detector testing, the dedicated beamline was not fully equipped and operational. Firstly, the distance between the electrostatic sweeper and the BPM/TOF detector was too short. The first unit could not be illuminated fully, while this was the case for the second unit. Secondly and more crucial, the Faraday cups before and after the BPM/TOF detector were not installed (see figure 4.12). Thus a provisional cup was placed behind the testbed and used as

Table 5.6.: Maximum manageable beam intensities of the detector. The values are calculated for a beam current of 1 pA.

Ion	Charge State	TKE [MeV]	Ion Rate [pps]
^{12}C	3+	16.9	$2.08 \cdot 10^6$
	4+	30.0	$1.56 \cdot 10^6$
^{16}O	5+	35.2	$1.25 \cdot 10^6$
^{32}S	6+	25.4	$1.04 \cdot 10^6$

beam stopper. Due to the primarily unfocused beam, the scattering and angular divergence of the beam resulted in a quite high offset of the cup signal. Furthermore the cup had no counter-voltage, resulting in false measurements. Nevertheless with this workaround one could at least centre the beam roughly. Meanwhile, the beamline was finished so that future measurements can be performed with a clearly focused beam.

Although some insecurity concerning the focus quality of the beam remained, a first in beam behaviour of the detector could be observed. Obviously, the detector is very sensitive to the beam current. If the current is too high, the detector saturates fast, resulting in 100% dead time of the DAQ. In reality, this was the case with currents of more than 1 pA. Since this value corresponds with the lowest measurable value of the used current integrators, one cannot clearly specify the real currents of the different ion beams. If taking 1 pA as maximum value, one can still estimate an upper value for the manageable amount of particles per second. Table 5.6 summarises these intensities for the used ion beams.

According to this assumption, the maximum manageable ion rate is limited to roughly 10^6 pps. Yet the beam was probably not as focused as it would have been possible with a real cup in front of the detector. Additionally, the missing counter-voltage of the provisional cup influences the measured signal to lower values, since the emitted electrons will not be collected and thus cannot correspond to the measurement. To conclude, the real ion rate had to be higher than the assumed one. For current possible slowed down beam experiments at the GSI based FRS, an ion rate of round about 10^5 pps is expected, so that this issue should be of no concern for the intended purpose of the detector [Bou07]. Yet it is an issue for measurements at the current beamline at the tandem accelerator. To limit the beam to such small currents, one needs to partly cut it off by slits. This in turn adds a certain amount of straggling and scattering ions to the beam, which is hard to suppress.

It has been observed that the MCP degrades fast in real beam measurements. Especially during the focusing at higher beam intensities with open slits, the high voltage supply of the detector heads and the reflecting modules should be shut down. The carbon foils exhibit a dark spot at the higher irradiated centre after some time of stable beam operation, which does not seem to influence the performance very much.

Table 5.7.: Measured and theoretical TOF values corresponding to figure 5.22. The measured values are once given for the raw, uncut data and once for cuts on the primary beam spots in both units.

Beam Ion	TKE [MeV]	Without Cut		With Cut		Theoretical TOF [ns]
		Measured TOF [ns]	Timing Resolution [ns]	Measured TOF [ns]	Timing Resolution [ns]	
^{12}C	16.9	22.552(8)	1.107(8)	22.53(3)	1.39(3)	21.862
^{12}C	30.0	16.806(2)	0.926(2)	16.8(4)	1.0(5)	16.423
^{16}O	32.5	17.992(2)	1.030(2)	17.93(7)	1.3(1)	17.5003
^{32}S	25.4	29.79(2)	1.02(2)	29.77(1)	0.62(3)	29.09

However, the lifetime of the MCP degrades very fast, especially for the centre spot. At the end of the in beam campaign, the second unit MCP showed a dead, spherical area in its centre. A timing signal could still be observed, but spatial information could no longer be obtained. Thus the gain must have decreased in a way that the amount of electrons in each spill was not exceeding the minimum needed amount in order to collect a DDL signal.

Two effects being observed in both detector units could not be explained. Firstly, the MCP timing signal is much sharper if being collected from the back side of a Chevron stack than from the front side. This behaviour was confirmed by JAGUTZKI, who notices the same effect in several MCP based detector heads without a valid explanation [Jag]. A second effect is a better spatial signal from one of the two DDL ends, while the other one is terminated, as described in section 3.4.2. Since there is no real physical explanation, the only logical one to be left seems to be a worse soldering or connection in one of the endings. Though a real explanation is missing for both effects, they do have an impact on the quality of the data and should thus be accepted.

5.4.2. Different time of flight measurements

A very first series of measurements was performed with different ion beams at different energies to test the timing resolution. The distance of the two detector units was fixed to 36 cm. The calibration was performed with a model *Ortec 462 Time Calibrator* [Ort13]. The corresponding plot can be seen in figure A.17.

In table 5.7 one can see the different TOF and resolution results in contrast to the theoretical value. The measured TOF and resolution is once given for the raw, uncut data and once with a cut on the primary beam spot in both units. Figure 5.21 shows exemplarily the hit patterns of the detector units for the ^{16}O beam, including the cuts on both beam spots.

Obviously, each measured TOF including its error does not match the theoretical value for the uncut as well as the cut data. Still, both values overlap the theoretical

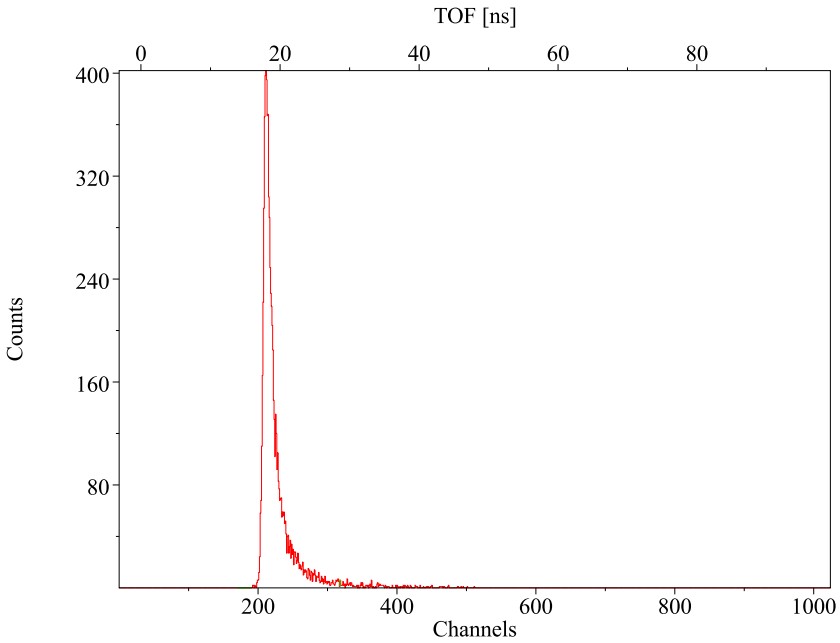

Figure 5.20.: Measured TOF for a ^{16}O beam at 32.5 MeV TKE after cuts on the primary beam spots, as seen in figure 5.21. The values are given in table 5.7. The corresponding raw, uncut data is shown in figure 5.22(c).

value within the timing resolution. It seems to be a systematical effect that all measured times are circa half a nanosecond too long. Looking at the corresponding uncut peaks in figure 5.22, all peaks exhibit a strong tail towards longer times. This might be a hint to a bad beam quality, probably due to poor focusing. Especially at the first unit, the beam spot seems to be somehow distorted (figure 5.21(a)), whereas the spot for the second unit seems to be more uniform, as expected (figure 5.21(b)). However, cutting on the major beam spot of both units, the measured TOF values and resolutions get even worse due to the high decrease in statistics. The corresponding TOF plot can be seen in figure 5.20.

One conclusion of this effect might be that the main beam is somehow scattered or losing a part of its energy. This would most probably happen at the slits, which are nearly closed. The slits themselves are shoes made of a tungsten rod. Thus the beam cutting part of the slit is a convex bending, which probably strengthens the assumed scattering or straggling. To exclude this possibility, new slits were built after this campaign. They consist of a razor blade like, sharp piece of tungsten, which will probably cut the beam off more precisely, reducing the amount of straggled or scattered ions.

Another possibility is an intrinsic offset of roughly half a nanosecond in the directly attached front end electronics in the FT12 connector, as discussed in section 4.2. Still these have been tested with a pulse generator and their jitter is in the range of a cou-

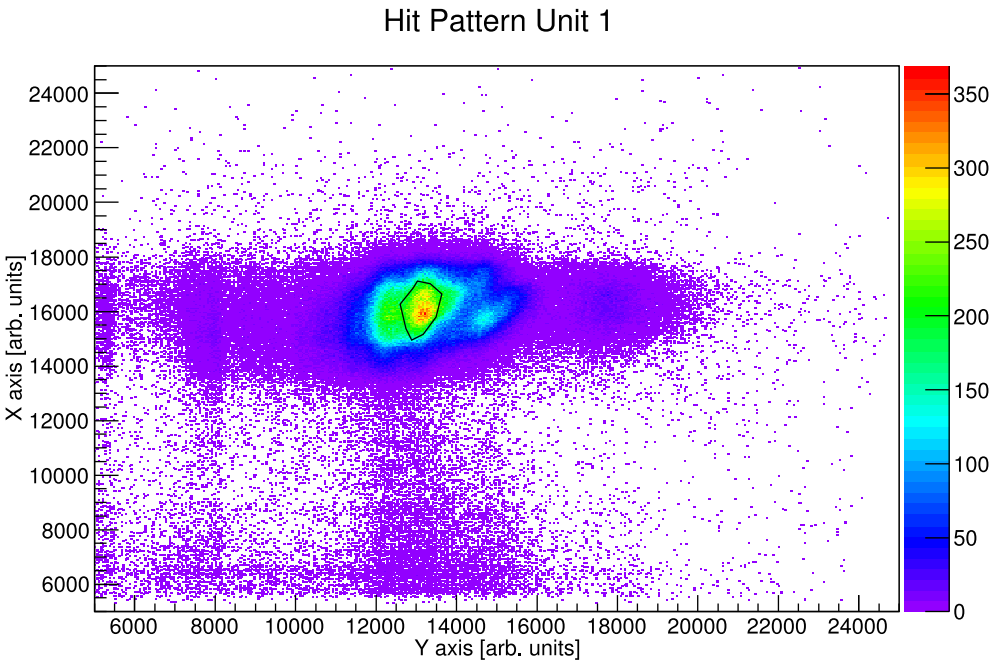

(a) Hit pattern of unit one.

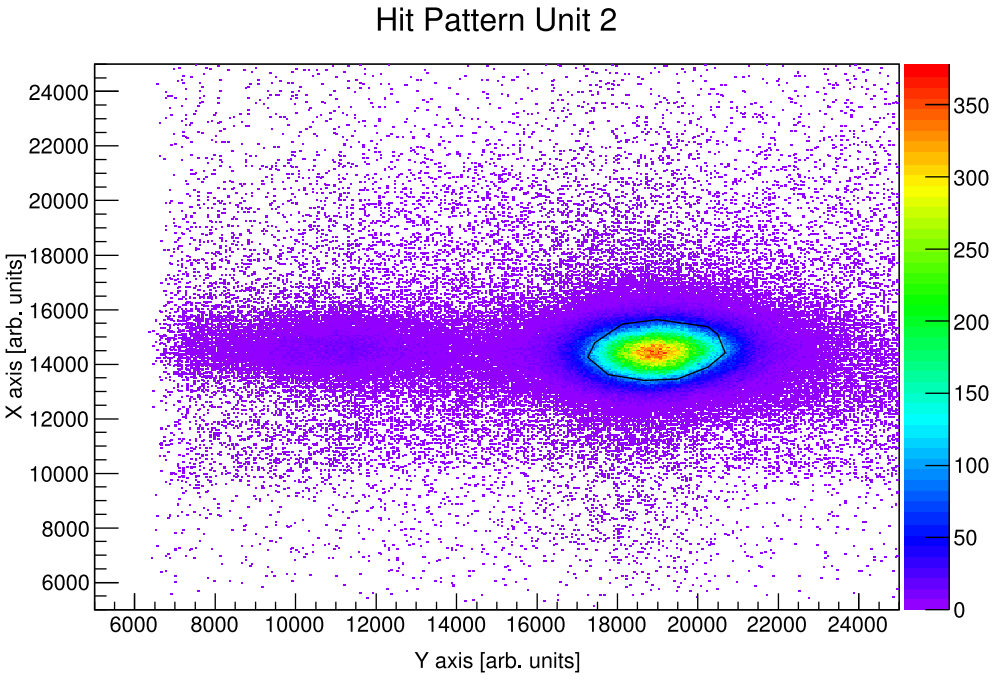

(b) Hit pattern of unit two.

Figure 5.21.: Exemplary in beam hit patterns of both detector units for a ^{16}O beam at 32.5 MeV TKE. The other hit patterns of this campaign looked very similar. The black polygons mark the cuts being applied for the determination of the TOF values, as given in table 5.7.

ple of picoseconds. Another fact speaking against this possibility is the non uniform offset of the different measurements. If the FT12 connector was the source of the measured, too high TOF value, it should be the same, regardless of the beam.

A second measurement with a quite well focused ^{12}C beam at 50 MeV TKE was performed nearly half a year later in March 2013 to test the discussed assumptions. Unfortunately, the MCP of both units were degraded in such a way, that no real measurement could be performed any more. Figure A.18 shows the centrally zoomed in hit pattern, taken with the first unit. One can clearly see a nearly dead spot in the direct centre of the beam spot. It is obvious that the MCP has degraded very much. The second unit, on the other hand, showed a quite sharp beam spot. Cutting on this beam spot and taking the TOF still leads to a very bad value of 21.8(1) ns with a resolution of 3.944(2) ns. The TOF for the raw, uncut TOF is 22.05(1) ns with a resolution of 4.92(1) ns. However, the theoretical TOF is 12.738 ns, which is nearly a factor of two smaller than the measured one. Additional tests at different MCP potentials gave similar results. Later on, the second unit MCP showed the same effect, resulting in even worse values. Thus both MCPs were degraded so far that they were no longer usable even for timing measurements.

Even though a final proof of the exact cause of the too long measured TOF cannot be given, the values are in the correct dimensions and do agree with the expected value within the resolution of the detector for this measurement. Future measurements with new MCPs and a well focused, thin beam have to show if the desired specification can be obtained with the second prototype at in beam experiments.

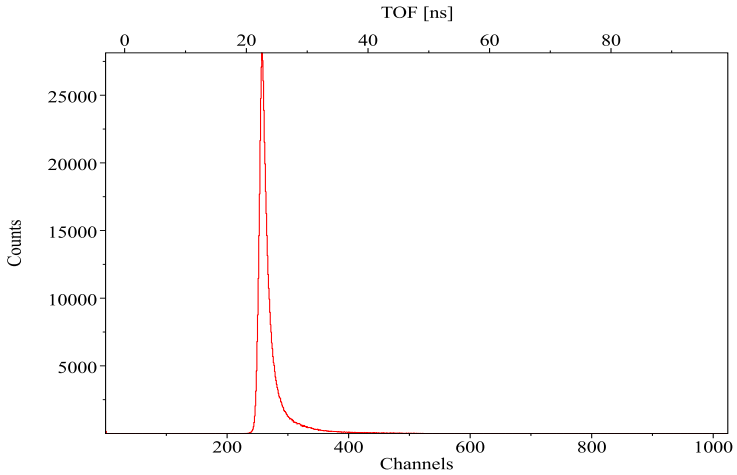

(a) ^{12}C at 16.9 MeV.

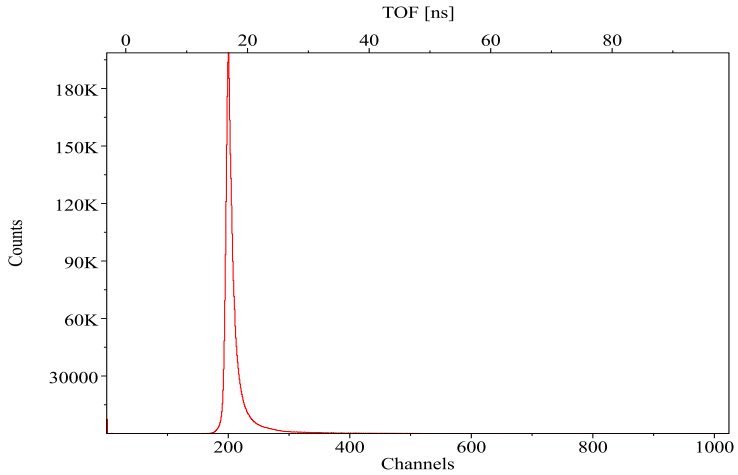

(b) ^{12}C at 30.0 MeV.

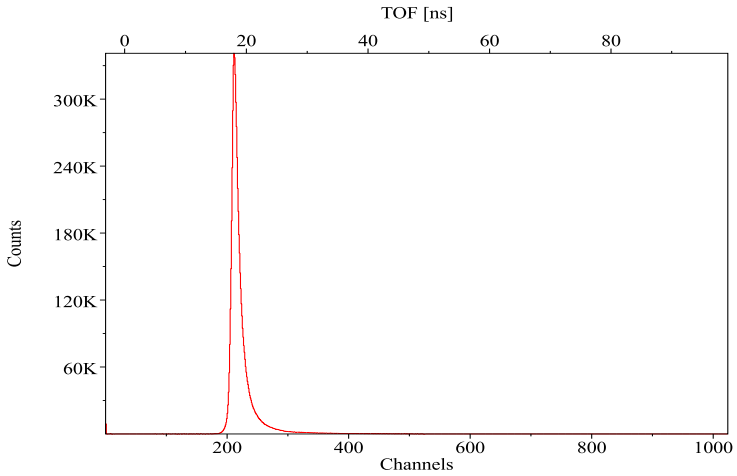

(c) ^{16}O at 32.5 MeV

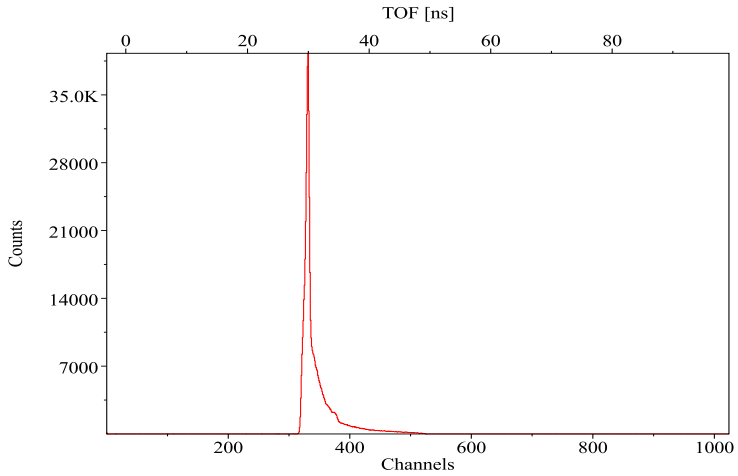

(d) ^{32}S at 25.4 MeV.

Figure 5.22.: Measured TOF for different kinds of ions at different TKE . Note that all peaks exhibit a strong tail towards longer times.

5.4.3. Mapping characteristics for different potential settings

A test with the known multi hole mask was performed, similar to the discussed test with the first prototype in section 5.3.2. This time a ^{12}C beam with a TKE of 30 MeV was used. In order to illuminate the whole active area, the electrostatic sweeper was used in combination with the integrated saw tooth voltage generator. Especially since the mesh distance of the reflecting module does not match the desired dimension (see section 4.2), it is important to understand the mapping characteristics more precisely. Therefore the potentials were changed systematically. While the accelerating potential V_{foil} were changed from $-2.8\,\text{kV}$ to $-3.2\,\text{kV}$ in $0.2\,\text{kV}$ steps, the reflecting potential V_{mirror} were changed from $-2\,\text{kV}$ to $-4\,\text{kV}$ in $0.2\,\text{kV}$ steps. Thus 33 different combinations emerge, which were measured for 15 min each. For each of the 15 projected holes, the position and the resolution in the X and Y axis projections were extracted.

For an easier discussion, a nomenclature for the single hole projections is given, as seen in figure 5.23. The mean positions are given as well: in this figure for a fixed $V_{\text{foil}} = -3\,\text{kV}$. Figure 5.24 additionally shows the plots for fixed $V_{\text{foil}} = -2.8\,\text{kV}$ and $-3.2\,\text{kV}$. One has to note that for this measurement the zero point of the coordinate is chosen differently. In contrast to the measurement discussed in section 5.3.2, the Y axis is mirrored. Thus projection S11 corresponds to the most distant row from the detector head. The X axis is kept the same, which means S11 corresponds to the left side of the detector head, if seen in direction of the beam. For a better understanding, a red dot in figure A.10 marks the corner of the zero point coordinate. All potential combinations show the same characteristics.

For the following discussion it is assumed, that the SE are emitted perpendicular from the conversion module and enter the reflecting module at parallel flight paths.

- Firstly, the centre of each projection moves further to lower Y axis values with increasing V_{mirror} potential. This is to be expected, since the deflection of the SE at the reflecting module becomes stronger.

- Secondly, the S1 to S5 and S11 to S15 (i.e. the upper and lower row of the mask, if seen as a table) projections bend towards the centre with increasing V_{mirror} potential. One explanation might be an accompanying electrostatic charging of the isolating mounting frame, placed at the sides and made of acrylic glass.

- Thirdly, the S1, S6 and S11 (i.e. the first column of the mask, if seen as a table) projections describe a curvature with respect to the Y axis position for an increasing V_{mirror} potential. In the beginning, they move to lower Y axis values, but move back to higher Y axis values after the V_{mirror} potential gets roughly larger than $-3\,\text{kV}$. Hence, the flight path of the reflected SE seems to somehow interact with the conversion module. The only logical effect causing this behaviour can be a penetration of the conversion module by the SE. Thereby, the conversion module functions as another electrostatic mirror, reflecting the SE to higher Y axis values. For fixed $V_{\text{foil}} = -3.2\,\text{kV}$, this effect influences projections with even higher Y axis values. The first column projections vanish

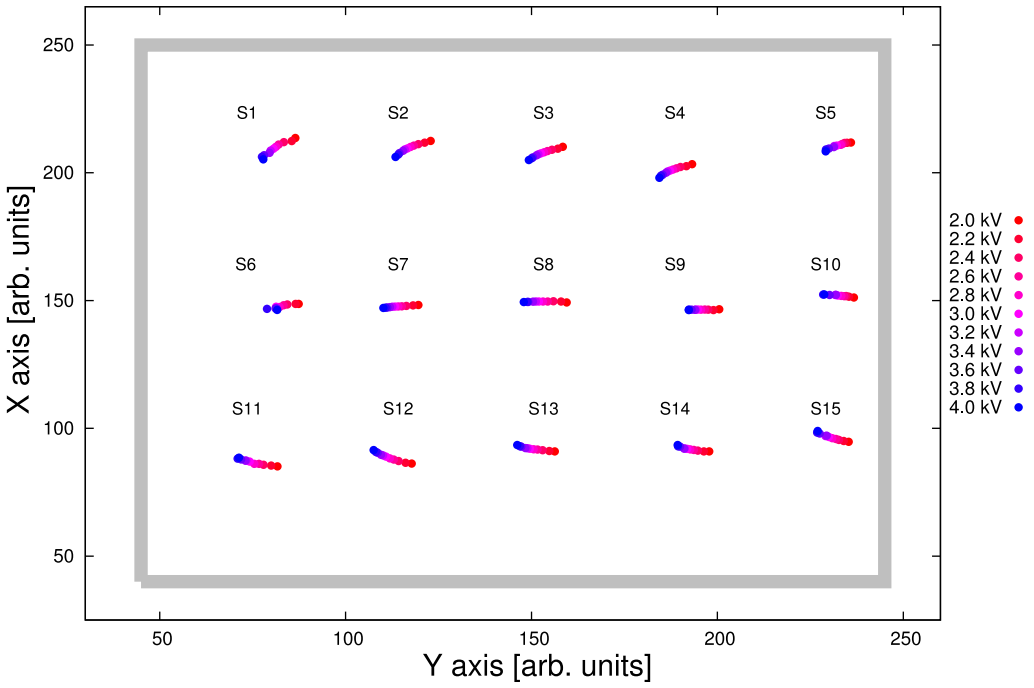

Figure 5.23.: Positions of multi hole mask projections at fixed $V_{\text{foil}} = -3\,\text{kV}$ and varying V_{mirror}. The latter values are given in the right key and are read to be negative. The grey frame roughly marks the active area of the MCP . Note the given nomenclature for the projected holes.

nearly completely for this case. It is interesting that this effect occurs at the lowest absolute difference between the V_{foil} and V_{mirror} potentials, where one would expect these effects to be least distinctive.

Another investigated measure is the resolution of the projections. Figure 5.25 shows the X axis resolutions and figure 5.26 the Y axis resolutions, both for all potential combinations. A very first observation is a nearly equal resolution over the whole active area for both axes. Thus the issue of worse X axis resolutions of the first prototype (see section 5.3.2) could be solved. Yet a certain behaviour of the resolutions can still be observed.

- The Y axis resolutions for $V_{\text{foil}} = -3.2\,\text{kV}$ are very bad for the middle row (S6 to S10), while being much better for the upper and lower row. For the X axis resolutions generally worse values can be observed.
- For $V_{\text{foil}} = -2.8\,\text{kV}$ and $-3\,\text{kV}$ the Y axis resolutions do not differ much and are quite stable for different V_{mirror}. For the X axis resolutions this is only the case for the middle columns. The resolutions of the right column projections become equally worse with a rising V_{mirror} potential for both V_{foil} potentials. The same

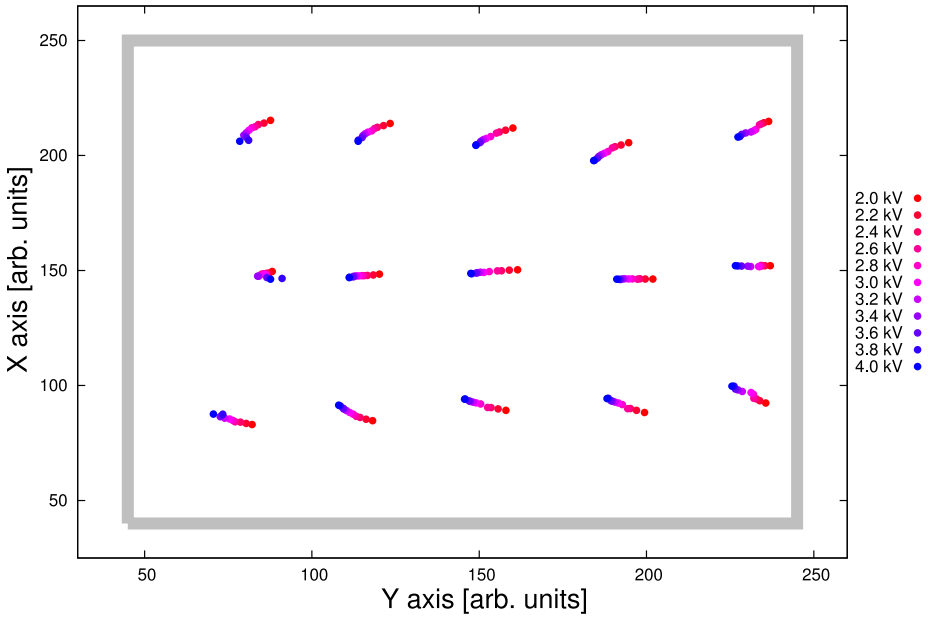

(a) Positions for $V_{\text{foil}} = -2.8\,\text{kV}$

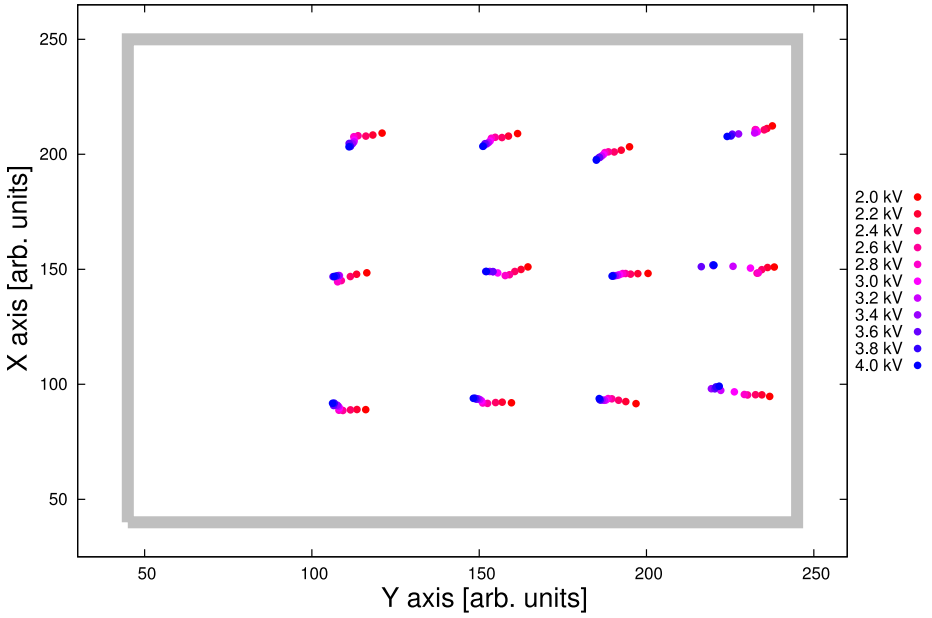

(b) Positions for $V_{\text{foil}} = -3.2\,\text{kV}$.

Figure 5.24.: Positions of multi hole mask projections at fixed $V_{\text{foil}} = -2.8\,\text{kV}$ and $-3.2\,\text{kV}$ at varying V_{mirror}. The latter values are given in the right key and are read to be negative. The grey frames roughly mark the active areas. Note that for $V_{\text{foil}} = -3.2\,\text{kV}$ the projections for S1, S6 and S11 are missing.

can be observed for the resolutions of the left column projections, although the values are generally better for $V_{\text{foil}} = -3\,\text{kV}$.

The effect of a poorly focused beam is hard to estimate, since the beam was swept over the whole active area. If the beam was focused poorly, the sweeping might have introduced an even stronger divergence behind the holes of the mask. This should only lead to a worse absolute resolution, but not influence the general trend of the behaviour, which is the justification for working with raw channel data. The key to a better understanding of the mapping characteristics is probably a better (thinner) beam quality and a better physical understanding of the electrostatic fields of the electrostatic top-assembly.

Concerning the latter, a software for the simulation of the field gradients and the SE flight paths was developed within a master thesis by CAPPELLAZZO, which can help to better understand this issue [Cap13]. As for now, an operation with potentials $V_{\text{foil}} = -3\,\text{kV}$ and below $V_{\text{mirror}} = -3\,\text{kV}$ seems to deliver the best results.

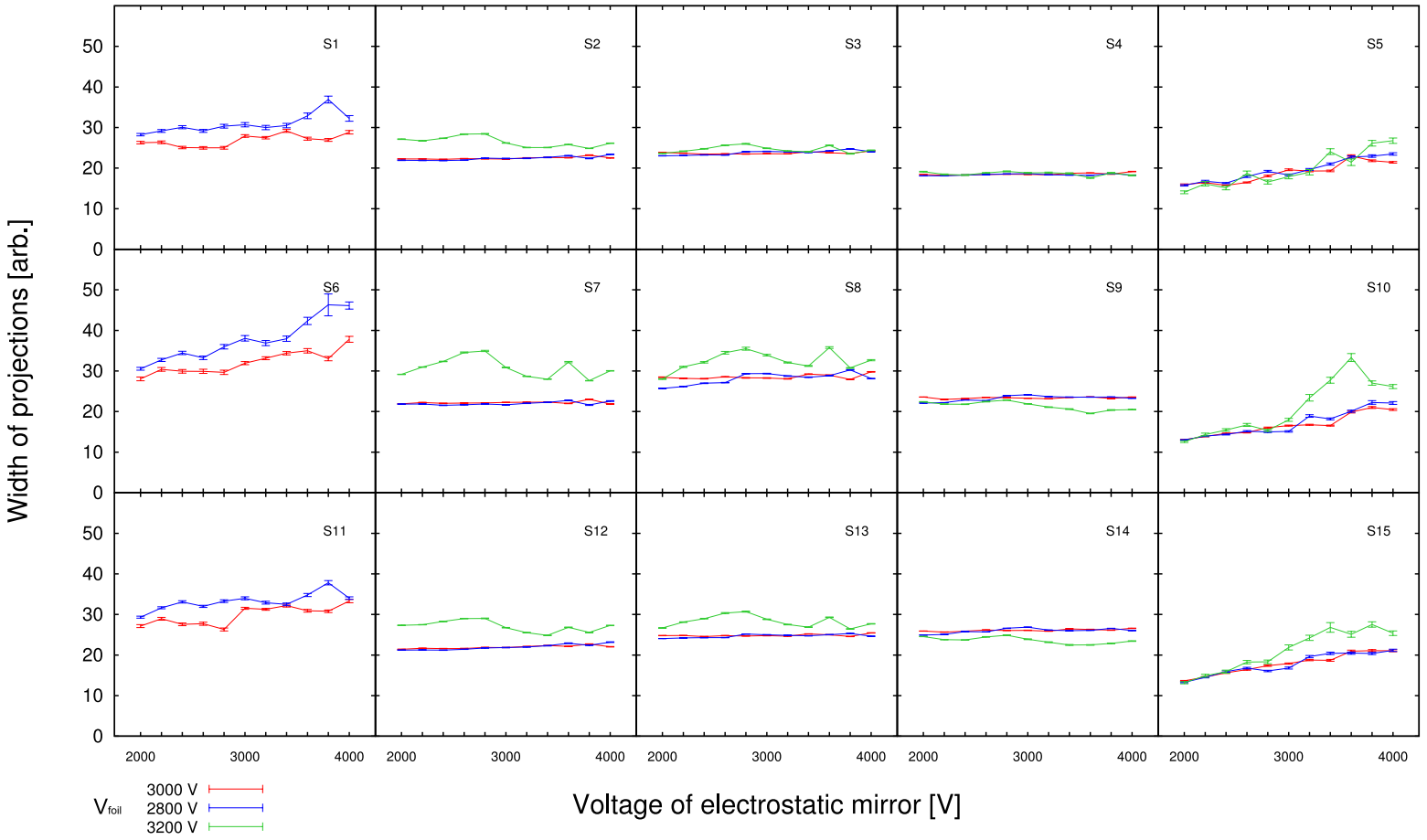

Figure 5.25.: X axis resolutions of multi hole mask projections at different potential combinations. Note that combinations with fixed $V_{\text{foil}} = -3.2\,\text{kV}$ will result in missing projections for S1, S6 and S11. All voltages are assumed to be negative.

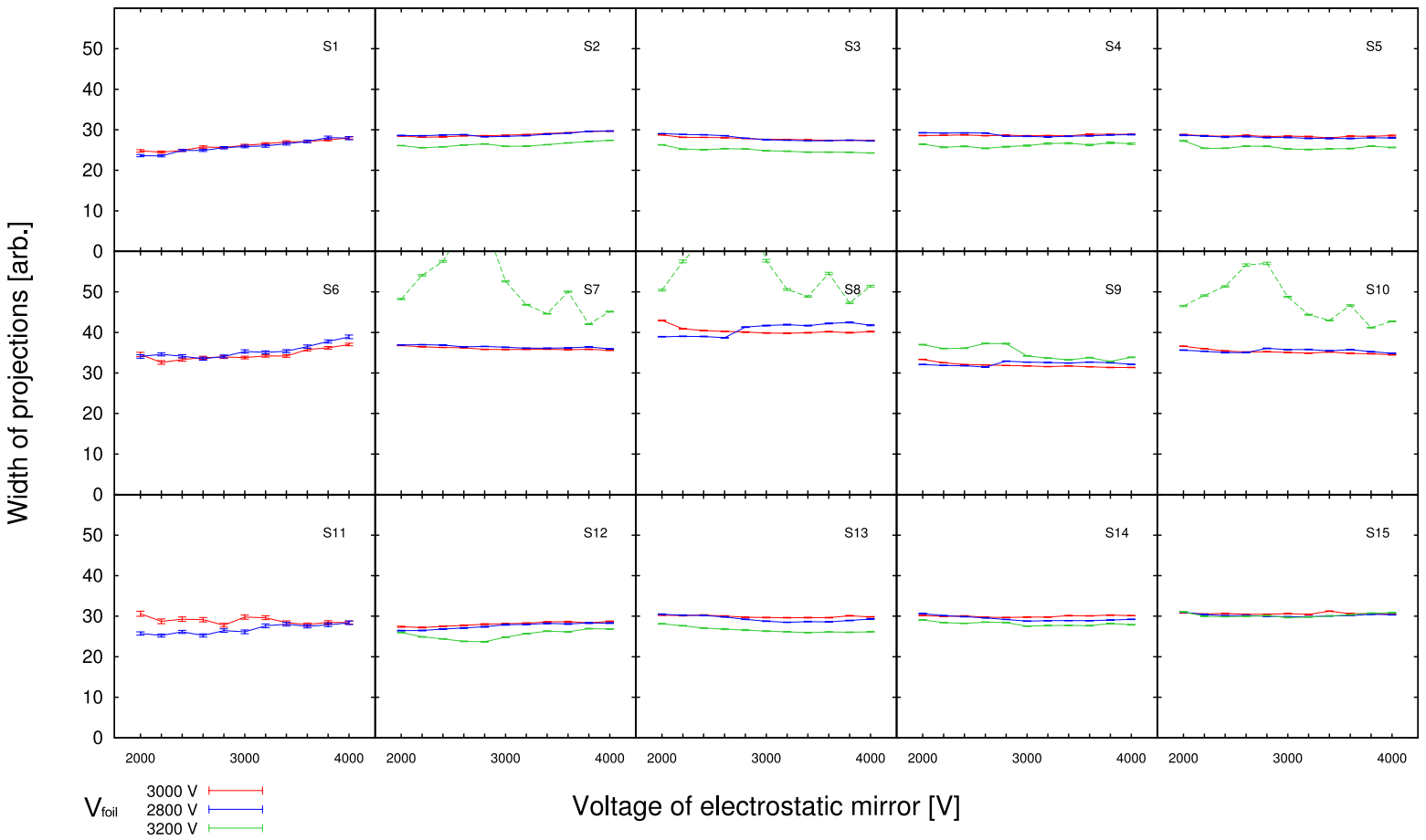

Figure 5.26.: Y axis resolutions of multi hole mask projections at different potential combinations. Note that combinations with fixed $V_{\text{foil}} = -3.2\,\text{kV}$ are not necessarily useful. All voltages are assumed to be negative.

6. Conclusions and outlook

This thesis presented the development of an integrated beam tracking and TOF detector for future slowed down beam experiments at GSI and FAIR. To estimate the desired specifications of the timing and spatial resolutions, a simulation of a slowed down beam for a typical nucleus of interest was performed. Therefore, the underlying physical processes have been summarised. Furthermore, the detector should obstruct the major ion beam with as little material as possible at a large active area. To fulfil these demands, an emissive foil design in combination with a MCP based detector head was chosen. After discussing basic physics of the emission of secondary electrons, the basic design of the detector was presented. Though it was originally developed by STARZECKI ET AL [Sta82], it has been expanded to a larger active area and extended by a position sensitive MCP read out anode.

The crucial point is to achieve a high timing and spatial resolution comparable to detectors with smaller active areas, despite the intrinsic transfer time spread of the MCP and the larger influence of the electrostatic top-assembly. Respecting the physical description of the time zero conditions for such a setup by KOSEV ET AL [Kos08b], the construction of the electrostatic top-assembly was introduced. Basic MCP physics and properties are given, as well as short description of the chosen, at that time largest available, MCP by Hamamatsu. Out of a variety of position sensitive read out anodes, a helical dual delay line was chosen.

Based on these decisions and components, two different prototypes were built. The first prototype was based on an inner, helical ground winding. Its negative influence on the spatial resolution of the X axis (perpendicular to the winding of the wires) was proven in different experiments with a multi hole mask in a specialised testbed. The predicted behaviour by KOSEV ET AL [Kos08b] could thus be experimentally confirmed. While the spatial resolution does not match the desired specifications, a very good timing resolution of down to nearly 200 ps was achieved. To achieve this, the in house developed, charge sensitive, differential preamplifiers were improved to a second revision and an auxiliary solar cell array as calorimetric beam stopper and additional global trigger was implemented. A practical consequence was the determination of the internal layer structure of a triple alpha source.

For the determination of the efficiency and to show the smooth integration in the GSI based DAQ framework, tests with an ^{252}Cf fission source and a reference DSSSD as stopper were performed at the X7 laboratory at GSI. The efficiency for bare TOF measurements could be proven to be around 70% for higher energetic fission products and roughly 20% for alpha particles emitted by standard sources. If asking for additional tracking capabilities, the efficiency for alphas decreases nearly by a factor of two. Since the future purpose is the detection of slowed down, higher Z ions, the

efficiency should easily comply with the given setups.

Drawing the experience gained with the first prototype, a second one was built with a focus on the redesign of the electrostatic top-assembly and an industry grade, compact and very flexible setup. Thereby the front-end electronics were changed from charge sensitive, differential preamplifiers to inductively coupled, current sensitive ones. Thus the complete electronics can be placed outside of the vacuum chamber, which enhances the vacuum a lot, resulting in less noise or dark current of the MCP . The electrostatic top-assembly was redesigned into a sandwich like structure. Even though it does not match the preferable dimensions, if not mounted in larger and more expensive ISO250 beam tube crosses, first investigations of the spatial resolution are promising. For in-beam tests a dedicated beamline has been set up at the Cologne FN Tandem accelerator facility. First in-beam tests after a long shut down showed that the measured TOF fits the theoretical values within the relatively low resolution. Most probably this is not caused by the detector, but by a straggling of the beam. At the time of the campaign, essential components for the beam focusing were still missing. Furthermore, the accelerator has to be run at the least possible beam current to not saturate the detector, which makes it difficult to produce a stable and well focused beam. Both issues resulted in a very poor beam quality, which is probably the explanation for the observed discrepancy with the theoretical values. For a more detailed understanding of the mapping characteristics of the new electrostatic top-assembly, a test with the established multi hole mask was performed. It could be shown that the different axes resolutions known from the first prototype have vanished and that the overall resolution was more equal at comparable values. Unfortunately, the MCP of both units have been degraded too far, so that they can no longer be used effectively.

Meanwhile, a spin-off project for the development of a similar, yet smaller system for the Cologne AMS[1] facility evolved. The aim is to suppress isobaric ions by discriminating the different TOF [Pas13].

To further investigate the second prototype and its in-beam behaviour, the dedicated beamline has to be improved in terms of ion optical instrumentation first. Afterwards, a low current and well focused, thin beam has to be created. An important tool to achieve this is the meanwhile available beam chopper of the accelerator. Improving the slits or working with a movable pinhole mask or alike might help, too. In between, the system could be tested with radioactive sources, if timing resolutions similar to the first prototype can be achieved.

To enhance the active area, a now available, spherical 150 mm diameter MCP by Photonis has been bought. Future work will be to design and construct a corresponding mounting frame. Furthermore it has to be shown that thin conversion foils of this size can be built stable enough to survive normal operation conditions. This unit can function as second detector unit, following the divergence of the primary ion beam.

From a DAQ point of view, the readout software for the TDC module by Surface Concept should be improved, whereas access to the internal, global clock has to be

[1] **A**ccelerator **m**ass **s**pectroscopy

granted. Additionally, the pulse height of the MCP signals should be measured. On the one hand one could correct for a non homogeneous gain of the active area, triggering only on high pulse events and cut off low pulse noise. On the other hand, one could implement a correction for the differing intensity of electron spills of the MCP for similar primary conditions. Therefore the pulse height has to be measured depending on its position.

Another option worth to be investigated is to turn around the detector units. It might prove to increase both the spatial as well as the timing resolutions by measuring the backward emitted SE from the conversion foil. A nice test experiment might be the use of the detector as a trigger for forward emitted protons in $(p, p'\gamma)$ nuclear structure experiments. Normal calorimetric detectors would not survive the harsh beam conditions at those forward angles. Their energy could then be discriminated by their TOF, if the primary ion beam was cut out by a hole in the conversion foil or alike.

Recapitulatory it can be said that the current prototype of the detector is already in an operational state and that it can be used at least as an ion optical instrument to survey beam conditions. If the detector can be used for its original purpose is yet to be shown in a real slowed down beam test experiment at GSI. For this purpose, the NUSTAR collaboration has suggested a so called umbrella proposal, which is the request for a longer beamtime to test auxiliary detectors for the future FAIR.

It is proposed to name the new detector *CIMBI*, short for **C**ologne **I**on **M**onitor for **B**eam **I**maging.

A. Appendix

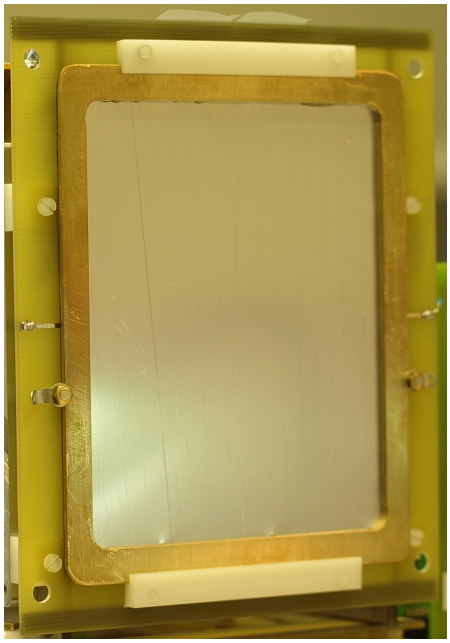

Figure A.1.: Picture of a metallised polycarbonate foil, which is mounted at the front of a detector unit. For details see section 3.2.2.

(a) Back view.

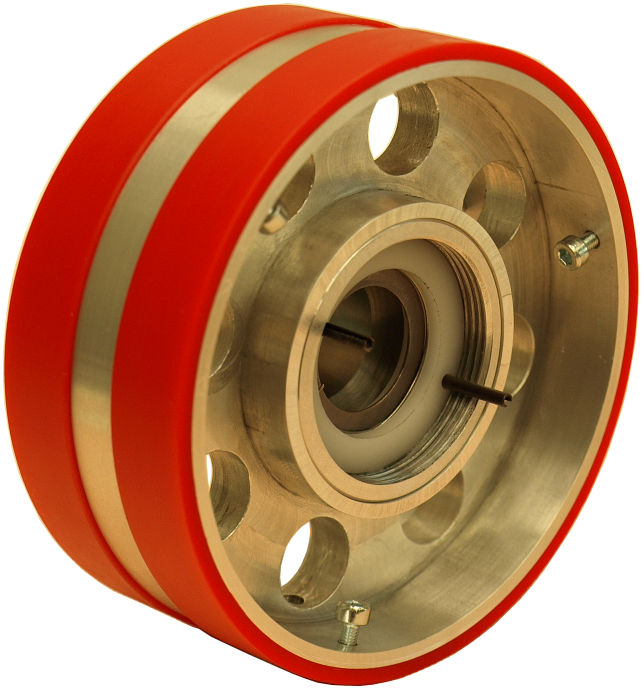

(b) Front view.

Figure A.2.: The source-pod in front and back view. It fits in a $4''$ beam-tube and can be moved like a sledge (see section 4.3.1 for details). The source is mounted from the back, while at the front different collimators can be attached.

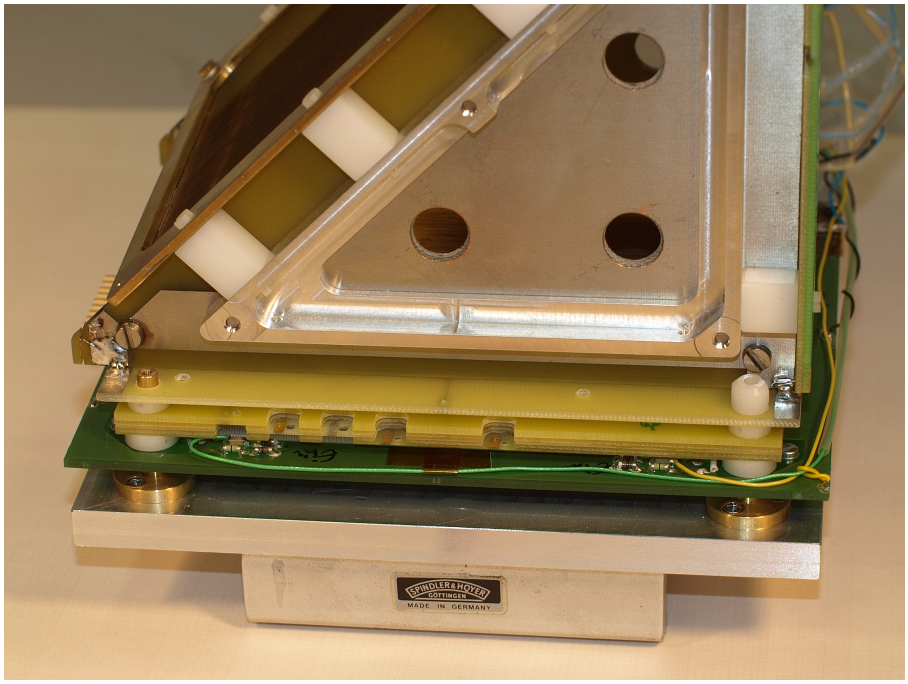

(a) Fully mounted unit.

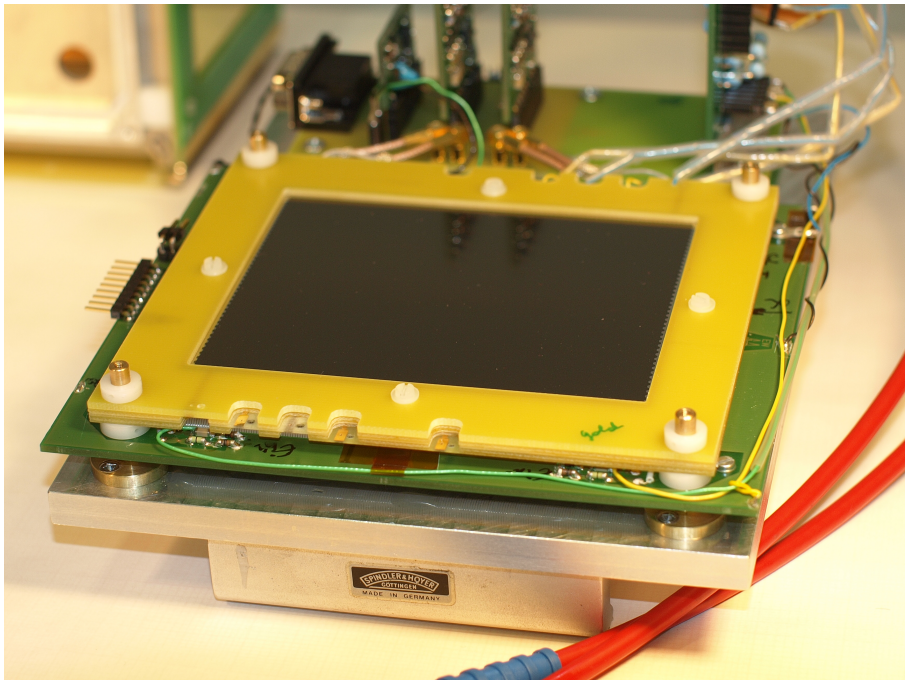

(b) Plain detector head.

Figure A.3.: Side view of fully mounted, single detector unit of the first prototype as described in section 4.1. Figure A.3(b) shows the actual detector head with the bare MCP chevron stack, as discussed in section 3.4. Figure A.4 shows the underlying DDL.

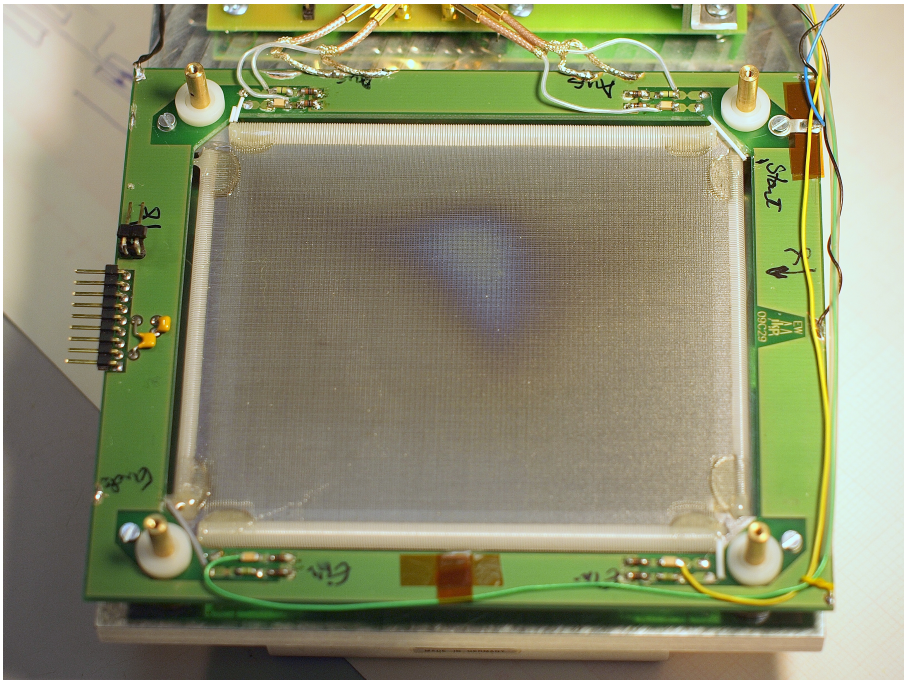

(a) Broken DDL.

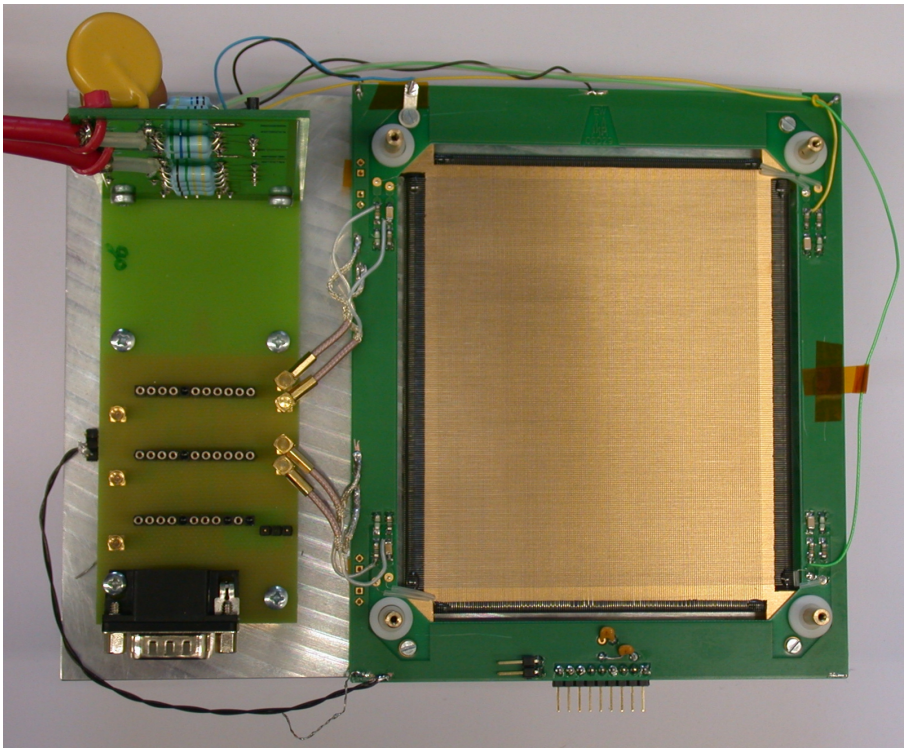

(b) Renewed DDL.

Figure A.4.: Both figures show a single detector unit, dismantled to the plain DDL board. For a detailed description see section 3.4.2.

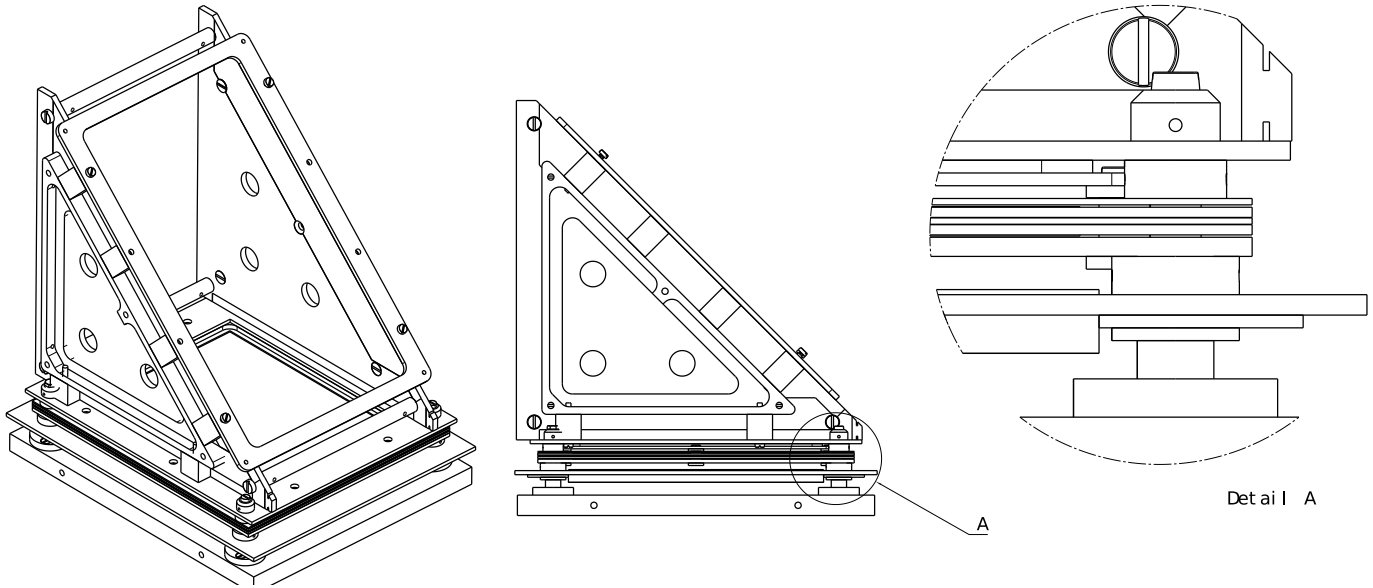

Figure A.5.: Technical drawings of the first prototype, as discussed in section 4.1. The left perspective shows an isometric back view, the middle a side view and the right a detail of the mounting system, as discussed in section 4.1.

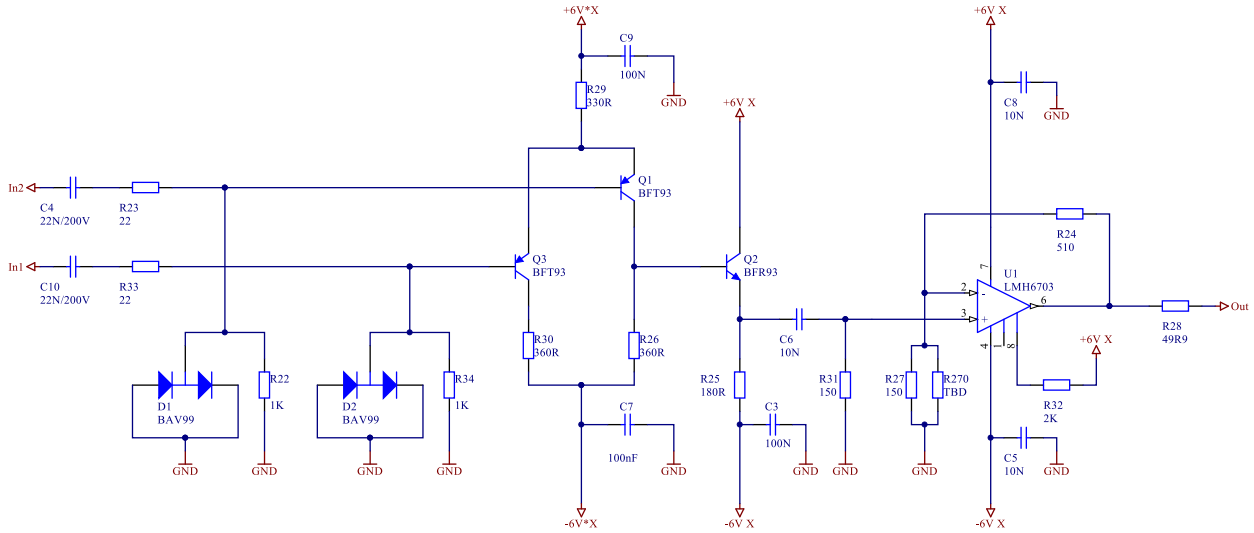

Figure A.6.: Circuit diagram of the second revision, differential preamplifier, as discussed in section 4.1. Courtesy of the in house electronics workshop.

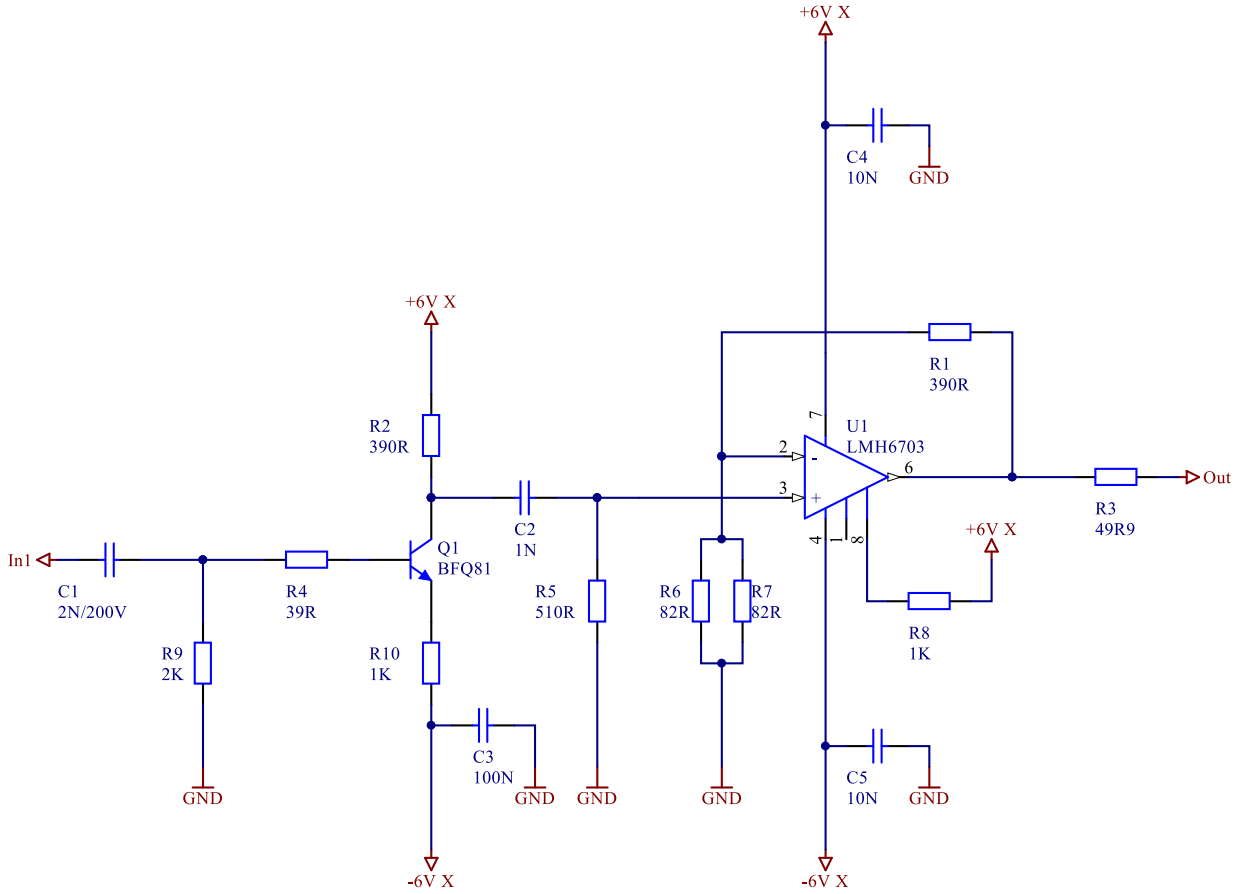

Figure A.7.: Circuit diagram of the timing preamplifier for the MCP, as discussed in section 4.1. Courtesy of the in house electronics workshop.

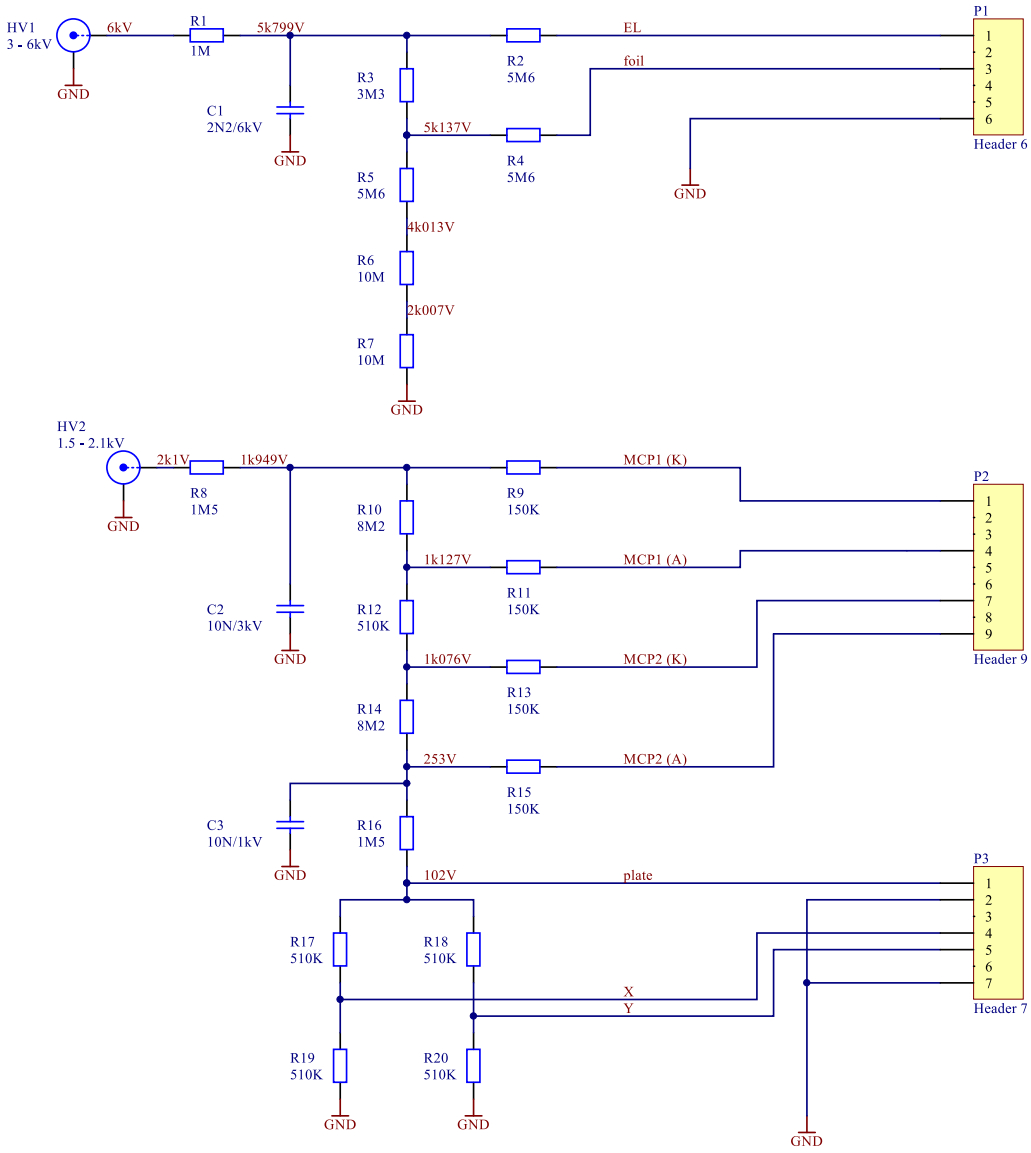

Figure A.8.: Circuit diagram of the second revision high voltage divider, as discussed in section 4.1. Courtesy of the in house electronics workshop.

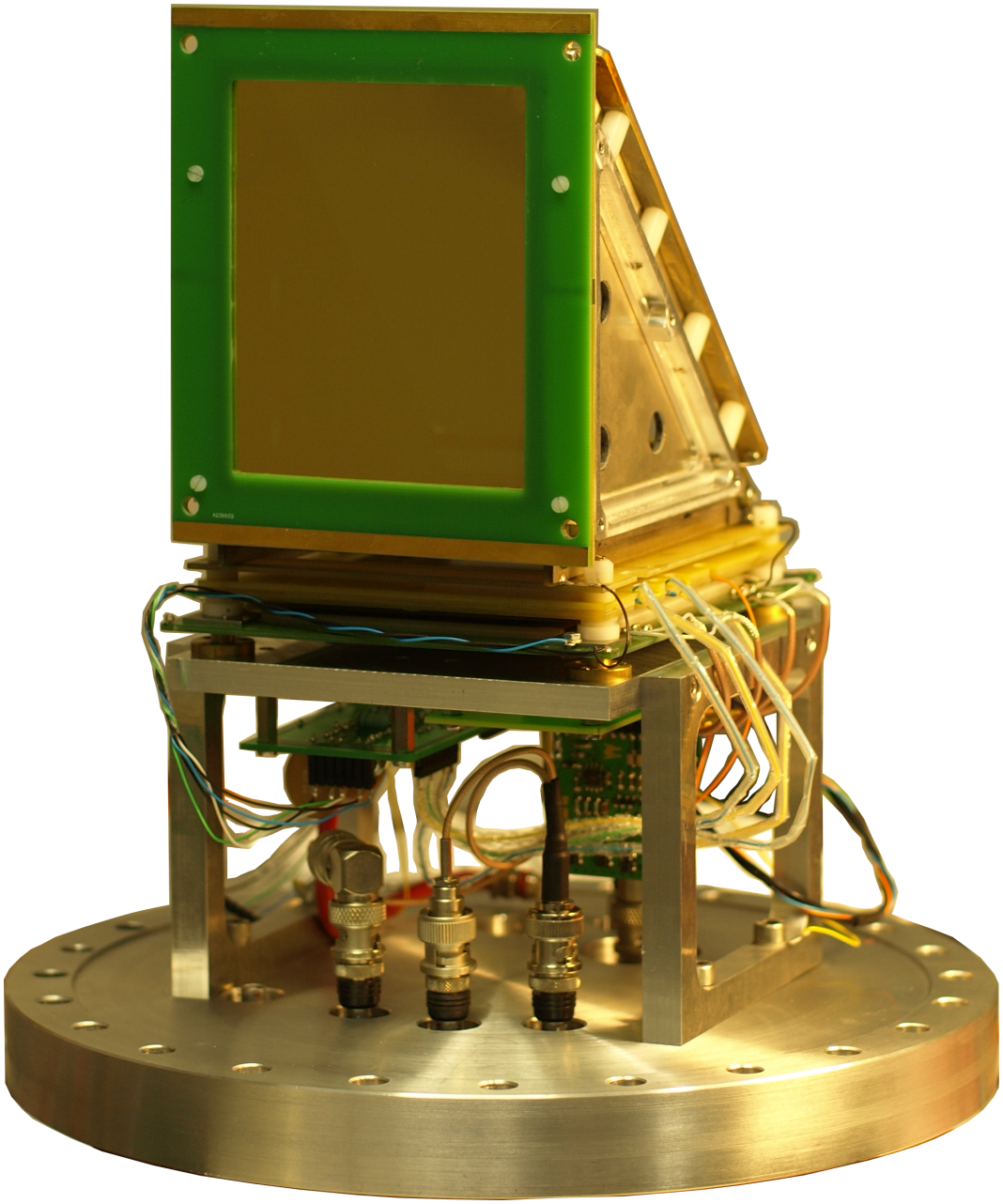

Figure A.9.: Picture of a specially mounted detector unit for measurements at GSI . It shows a first prototype design with second revision front end electronics, as described in section 4.1. The utilised gold coated conversion foil is discussed in section 3.2.2.

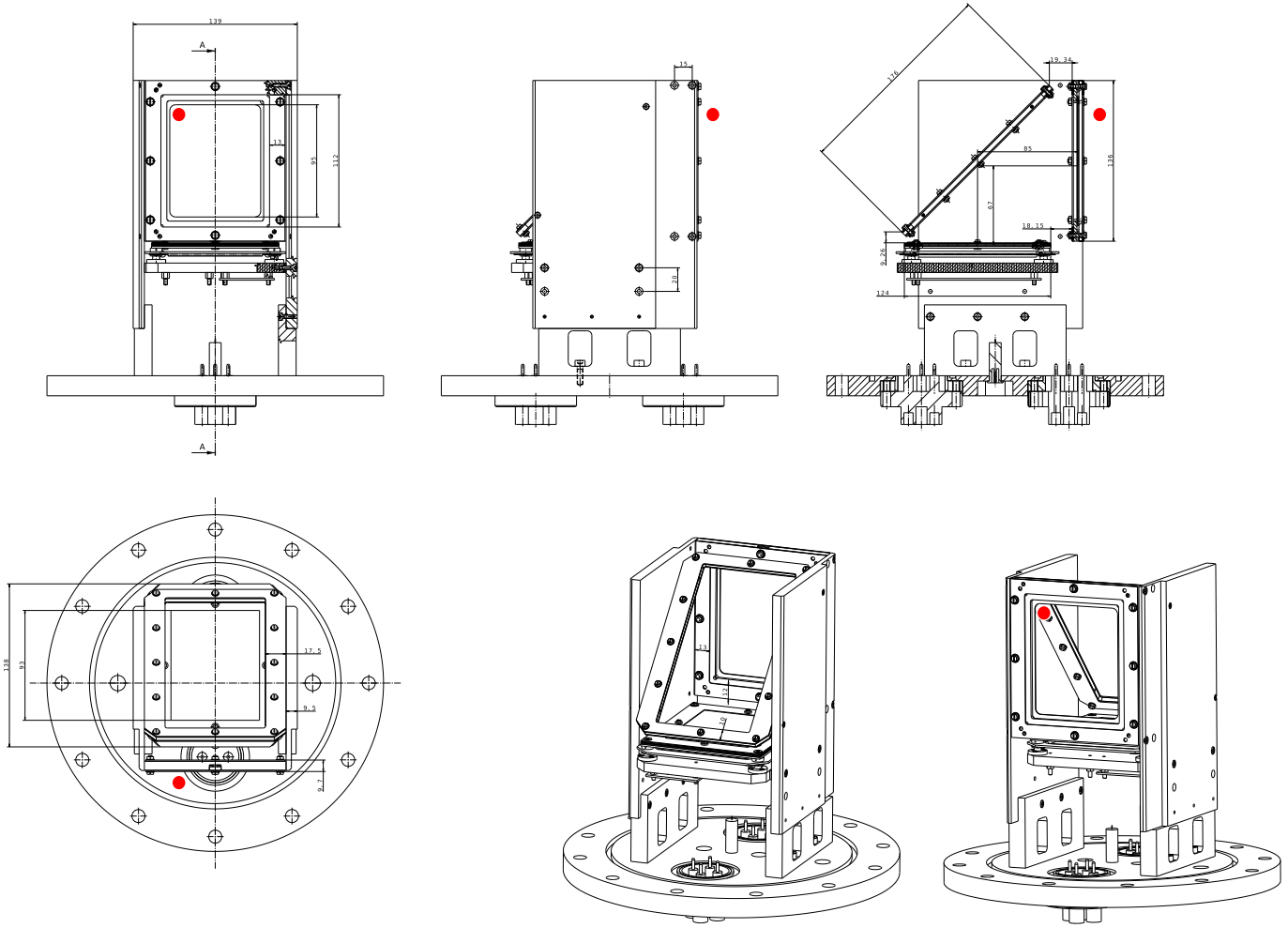

Figure A.10.: Technical drawings of the second prototype, as discussed in section 4.2. The upper left perspective is a front view, the upper middle and right are side views, once with and once without holding structure. The lower left perspective shows a top view, while the last two perspectives show isometric back and front views. The red dots mark the corner of the deviant zero point coordinate according to the measurement discussed in section 5.4.3.

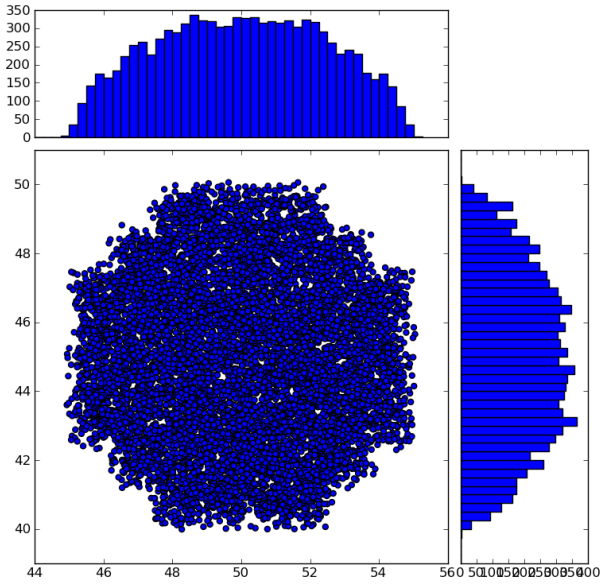

(a) Projection on unit one.

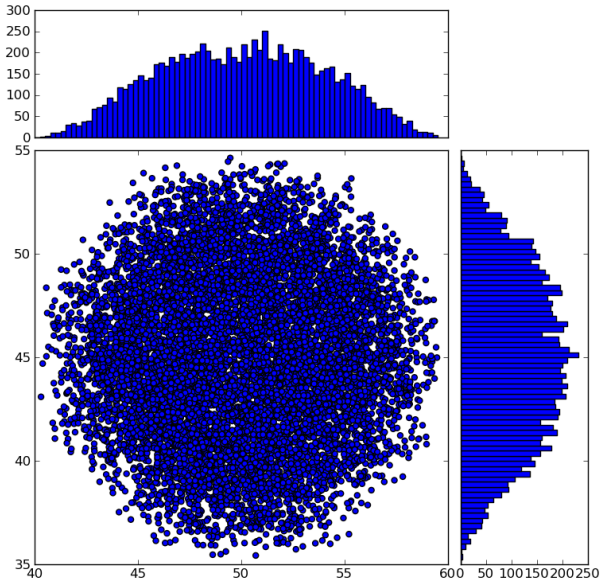

(b) Projection on unit two.

Figure A.11.: Simulated projections of 6 mm collimated source on the conversion foil of unit one and two. The units are arbitrary, since the plot shows the raw simulation data. The simulation was done by the SIMION program package [Ser12] and is discussed in section 5.2.2.

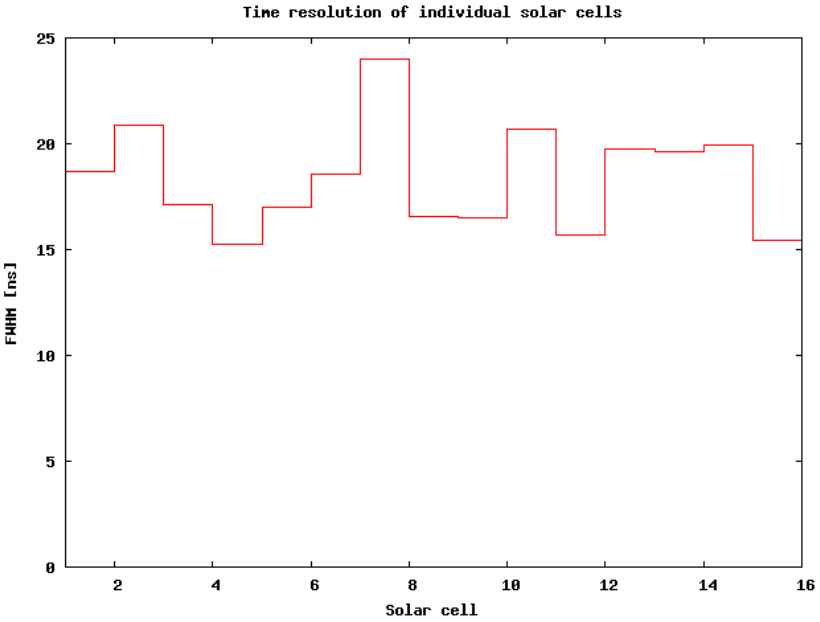

Figure A.12.: Timing resolution of the solar cells discussed in section 5.2.1, where each channel consists of two OR wired cells.

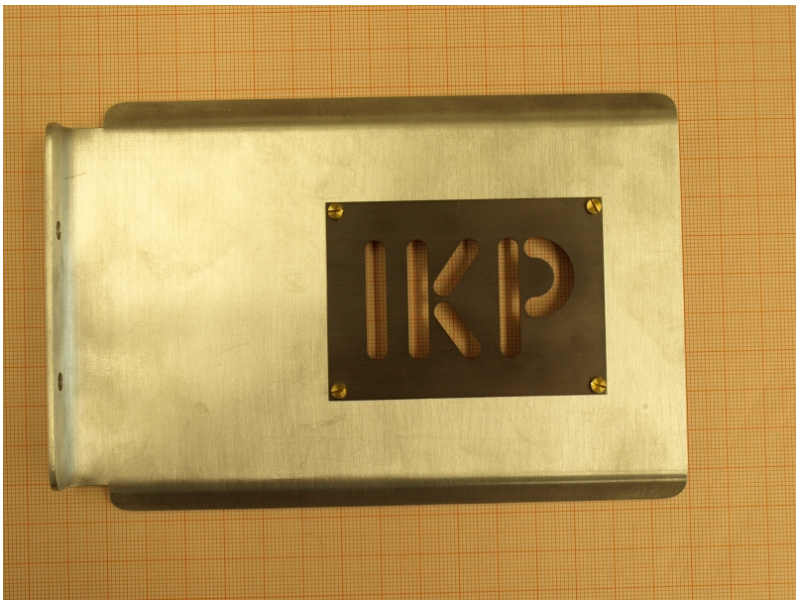

Figure A.13.: Picture of a mask with the abbreviation of the institute, mounted on a holding structure, which can be fixed to a sledge for the optical bench in the first test chamber. The width of the cuts of the letters is 5 mm, so is the distance between the letters. See section 5.2.3 for more details.

Table A.1.: Important parameters to set up the detector to an operational state. Most values are gained from experience, while the ones marked are given in the handling instructions from the MCP manufacturer. Even though Hamamatsu and not Photonis made MCP have been used, the very conservative parameters by Photonis were preferred. Note that the ranges for the potentials are to be taken as negative values. A more detailed description is given in section 5.1.1.

	Pressure		
	Range	Pumping Gradient [mbar/min]	Minimum Pressure [mbar]
Whole Chamber (Carbon Foil)	> 1 mbar < 1 mbar	±20 max. possible	— $1.3 \cdot 10^{-6}$ †
Whole Chamber (Metallised Plastic)	> 1 mbar < 1 mbar	±100 max. possible	— $1.3 \cdot 10^{-6}$ †

	Potential			
	Range (negative)	Increment [V]	Waiting Time [min]	Maximum Voltage [V]
Conversion Module (Carbon Foil)	< 1.5 kV > 1.5 kV	±100 ±50	1 2	— −3500
Conversion Module (Metallised Plastic)	—	±500	< 1	−3500
Reflecting Module	—	±500	< 1	−4000
MCP *	< 1 kV 1 – 1.5 kV > 1.5 kV	±100 ±100 ±50	2 5 10	— — −2000
Input DDL HV splitter	—	±200	< 1	+400

†Values specified by Hamamatsu [Ham09]
MCP *must* be degassed at his pressure for 24 hours

*Values specified by Photonis [Pho09]

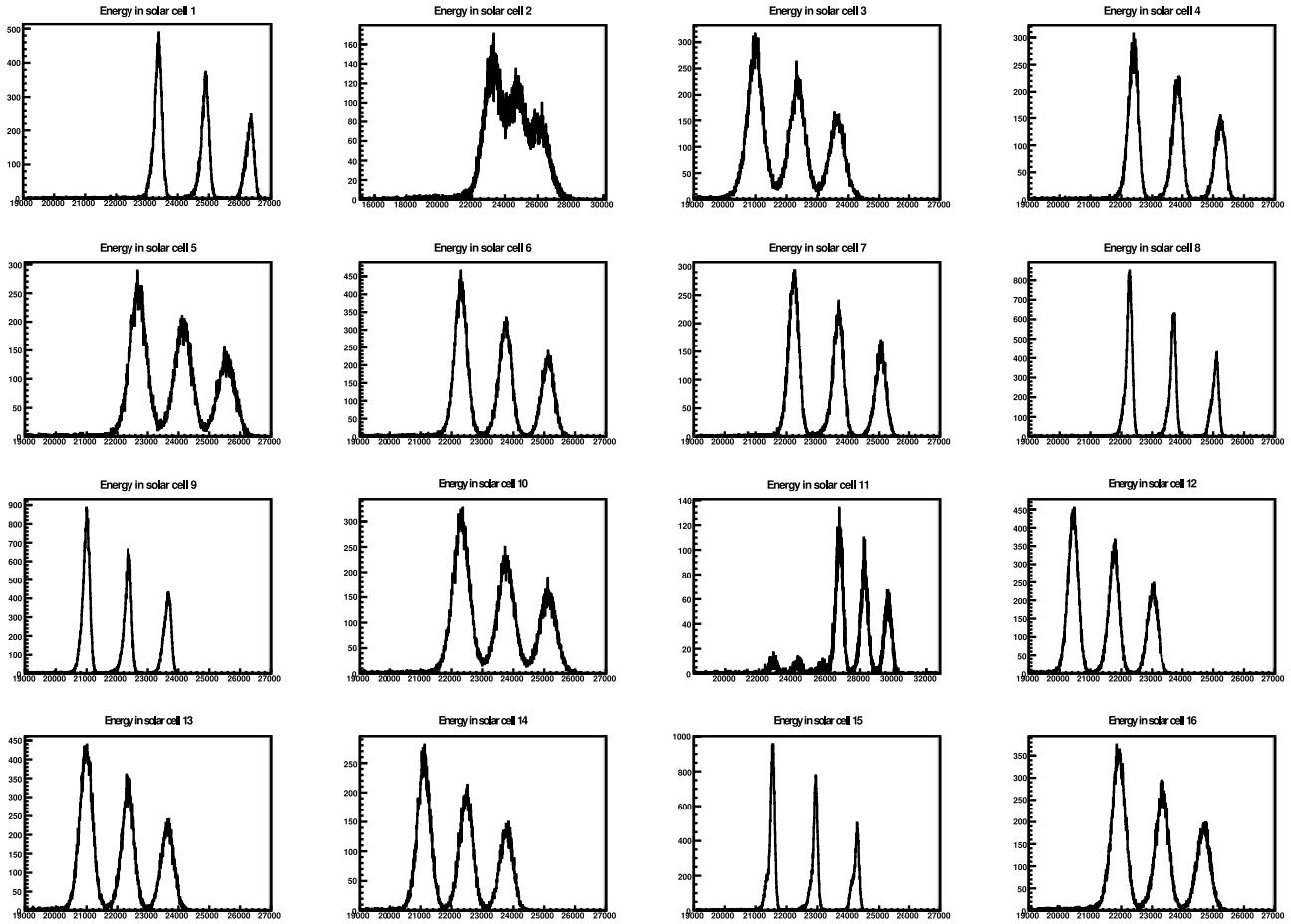

Figure A.14.: Raw, uncalibrated energy spectra of the solar cell array (see section 5.2.1) taken with a triple alpha source. This data was used to build a calibration and offset matrix to compensate for the differences as much as possible.

Table A.2.: Measured spatial resolutions of a projected multi hole mask for the first detector unit, as discussed in section 5.3.2. The calculated position of the projected holes on the conversion foil is given as corresponding axis positions.

X projections		X axis position [mm] 27	43	57
Y axis position [mm]	77	16.99(23)	11.61(19)	18.33(17)
	66	15.848(50)	10.881(60)	15.724(52)
	53	12.245(43)	11.427(61)	12.308(63)
	38	10.758(43)	10.531(33)	10.781(31)
	23	11.932(51)	9.920(46)	10.918(40)
Y projections		**X axis position [mm] 27**	**43**	**57**
Y axis position [mm]	77	7.712(49)	8.564(27)	9.282(33)
	66	6.822(12)	6.975(11)	6.951(11)
	53	7.549(14)	7.854(12)	8.490(15)
	38	8.153(15)	8.203(10)	8.232(10)
	23	7.458(47)	8.467(21)	8.563(22)

Table A.3.: Measured spatial resolutions of a projected multi hole mask for the second detector unit, as discussed in section 5.3.2. The calculated position of the projected holes on the conversion foil is given as corresponding axis positions. The lower row was not fully projected and cut off by the edge of the active area. Those values are refused.

X projections		Y axis position [mm] 23	43	62
X axis position [mm]	88	17.220(98)	17.39(14)	15.720(88)
	70	14.872(41)	17.453(63)	12.841(26)
	49	11.680(22)	16.876(42)	11.402(22)
	26	9.432(13)	14.332(26)	11.559(15)
Y projections		**Y axis position [mm] 23**	**43**	**62**
X axis position [mm]	88	8.893(26)	99.199(27)	9.341(30)
	70	11.463(17)	11.349(15)	1.643(15)
	49	12.111(15)	12.535(16)	14.184(24)
	26	12.385(16)	12.032(14)	12.588(14)

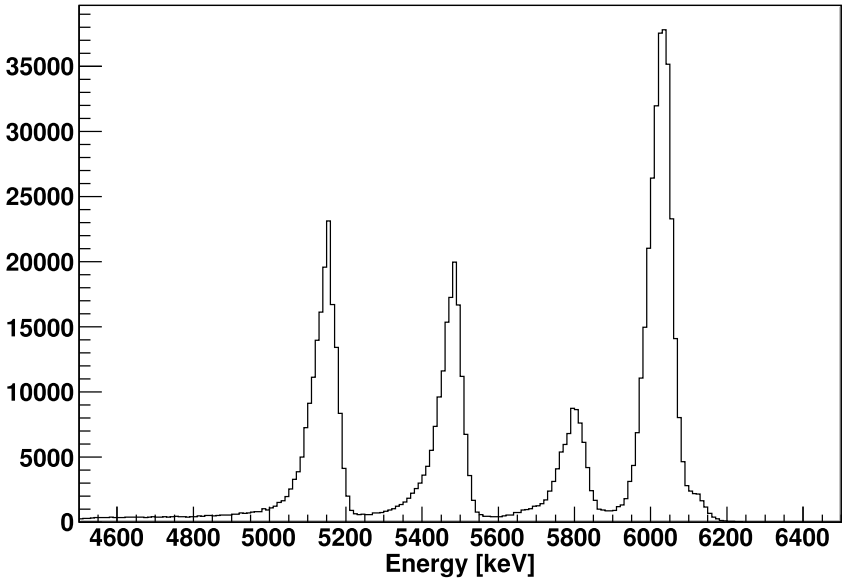

(a) DSSSD energy spectrum.

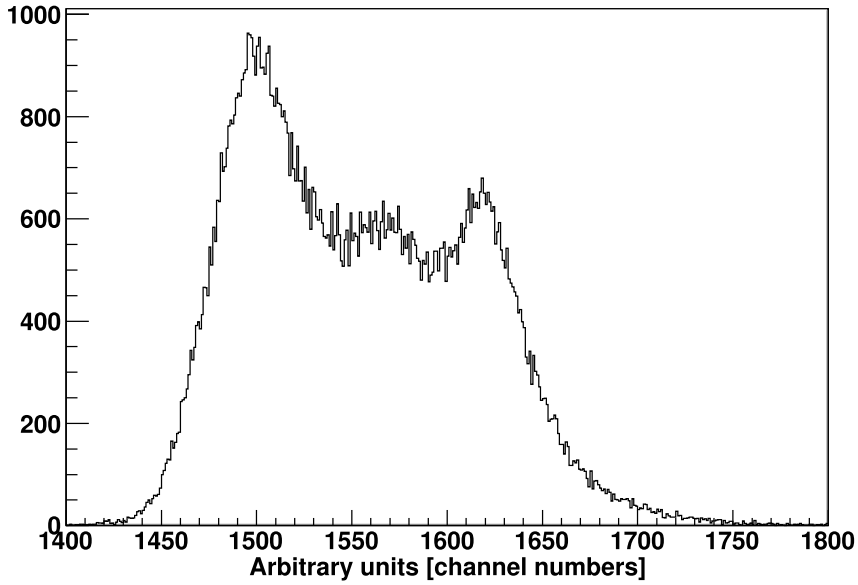

(b) TOF spectrum.

Figure A.15.: Measured energy and corresponding TOF spectra of the efficiency measurement for low energetic alpha particles. Soft conditions were applied, as described in section 5.3.3.

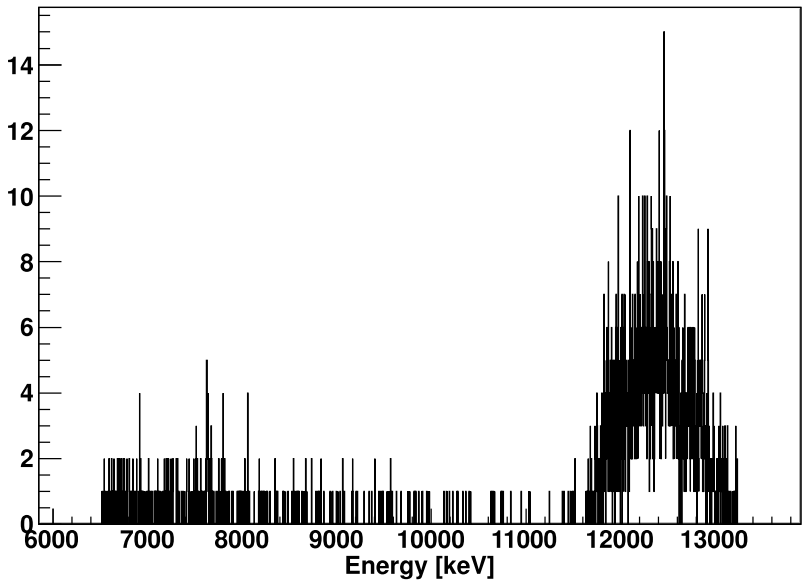

(a) DSSSD energy spectrum.

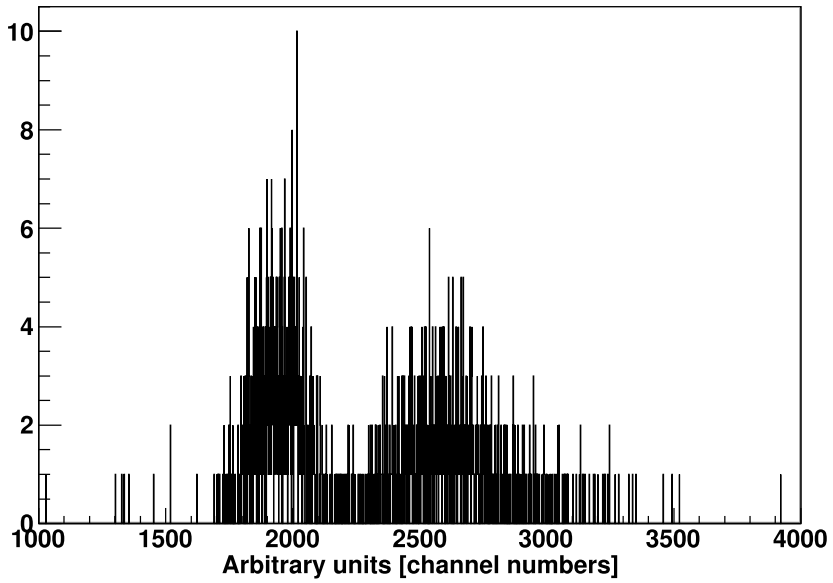

(b) TOF spectrum.

Figure A.16.: Measured energy and corresponding TOF spectra of the efficiency measurement for high energetic SF products. Soft conditions were applied, as described in section 5.3.3.

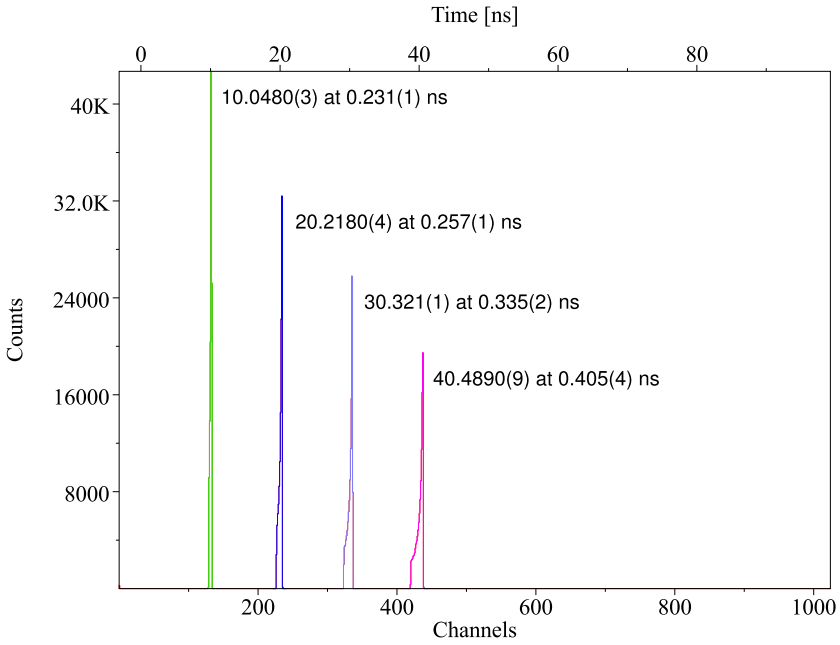

Figure A.17.: Timing resolution of the TOF TAC for the in beam measurements, taken with a Ortec 462 Time Calibrator, as discussed in section 5.4.2. The corresponding time and FWHM values are given aside the corresponding peaks.

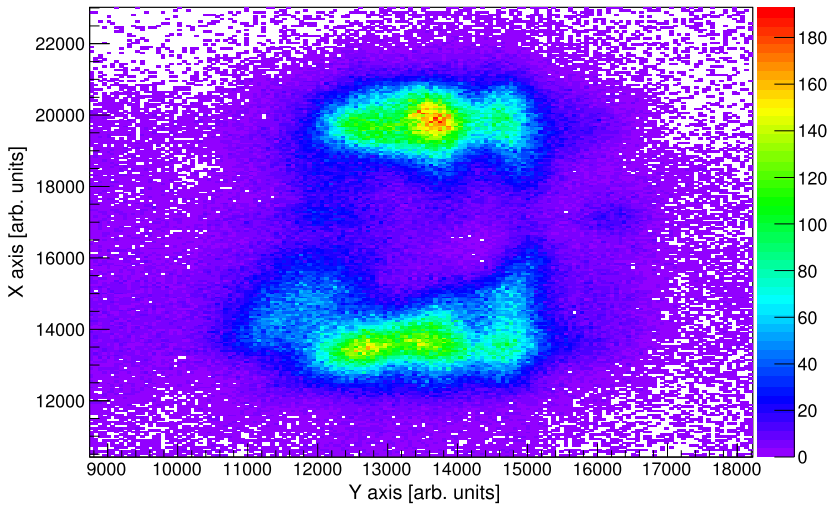

Figure A.18.: Zoomed in hit pattern of a well focused ^{12}C beam at 50 MeV TKE , taken with a centrally degraded MCP . One can clearly see the nearly dead spot in the centre. A discussion of the resulting data is given in section 5.4.2.

B. Glossary

A short summary of frequently used abbreviations.

ADC	Analogue to Digital Converter
BPM	Beam Profile Monitor
CFD	Constant Fraction Discriminator
DAQ	Data Acquisition
DDL	Dual Delay Line
DESPEC	Decay Spectroscopy
DSSSD	Double Sided Silicon Strip Detector
FAIR	Facility for Antiproton and Ion Research
FRS	Fragment Separator
FWHM	Full Width Half Maximum
GSI	Helmholtz Gesellschaft für Schwerionenforschung GmbH
HISPEC	High In-flight Spectroscopy
ISOL	Isotope Separator On-Line
MCP	Micro Channel Plate
RIB	Radioactive Ion Beam
SDB	Slowed Down Beam
SE	Secondary Electron(s)
TAC	Time to Amplitude Converter
TDC	Time to Digital Converter
TKE	Total Kinetic Energy
TOF	Time of Flight

List of Figures

List of Tables

Bibliography

[Alb12] ALBERS, M., N. WARR, K. NOMURA, ET AL.; *Evidence for a Smooth Onset of Deformation in the Neutron-Rich Kr Isotopes*; Physical Review Letters (**2012**); 108, 062701–1–062701–5

[And94] ANDERSEN, J., G. BALL, J. DAVIES, ET AL.; *Energy loss of heavy ions at high velocity*; Nuclear Instruments and Methods in Physics Research Section B: Beam Interactions with Materials and Atoms (**1994**); 90(1–4), 104 – 111; ISSN 0168-583X; doi:10.1016/0168-583X(94)95523-9

[Anh79] ANHOLT, R.; *Calculation of K-vacancy production by relativistic projectiles*; Phys. Rev. A (**1979**); 19, 1004–1010; doi:10.1103/PhysRevA.19.1004

[Arm76] ARMBRUSTER, P., M. ASGHAR, J. BOCQUET, ET AL.; *The recoil separator Lohengrin: Performance and special features for experiments*; Nuclear Instruments and Methods (**1976**); 139, 213–222

[Bet32] BETHE, H.; *Bremsformel für Elektronen relativistischer Geschwindigkeit*; Zeitschrift für Physik (**1932**); 76, 293–299; ISSN 0044-3328; doi:10.1007/BF01342532

[Boh48] BOHR, N.; *The penetration of atomic particles through matter*; vol. 8; chap. 3, pp. 1–144; K. Dan. Videnskab. Selskab. Mat. Fys. Medd. 18 (**1948**)

[Bou07] BOUTACHKOV, P.; *Monte-Carlo Simulations and detector requirements for slowed down beams at GSI*; Presentation; GSI Darmstadt (**2007**); secondary Electron Detection Workshop Cologne

[Bou08] BOUTACHKOV, P., M. GÓRSKA, J. GERL, ET AL.; *Simulations and first tests of slowed down beams project at GSI*; p. 215; GSI Scientific Report 2007; Gesellschaft für Schwerionenforschung mbH (**2008**)
http://www-alt.gsi.de/informationen/wti/library/scientificreport2007/PAPERS/INSTRUMENTS-METHODS-09.pdf

[Bou13] BOUTACHKOV, P., E. GREGOR, N. PIETRALLA, ET AL.; *Fast Timing with DSSSD Detectors*; p. 183; GSI Scientific Report 2012; Gesellschaft für Schwerionenforschung mbH (**2013**)
http://repository.gsi.de/record/52086/files/PHN-ENNA-EXP-53.pdf?version=1

[Bru97] BRUN, R. and F. RADEMAKERS; *ROOT - An object oriented data analysis framework*; Nuclear Instruments and Methods in Physics Research Section A: Accelerators, Spectrometers, Detectors and Associated Equipment (**1997**); 389(1-2), 81–86; ISSN 0168-9002; doi:10.1016/S0168-9002(97)00048-X; new Computing Techniques in Physics Research V

[Bur05] BURLE; *BURLE Long-LifeTM MCP Selection Guide*; Website (**2005**) http://public.wsu.edu/~scudiero/documents/Channel-plates.pdf

[Cap13] CAPPELLAZZO, M.; *Untersuchungen zur Möglichkeit der Modellierung des CIMBI-Detektors und Aufbau eines Datenaufnahmesystems mittels eines Time to Digital Converters*; Master's thesis; Universität zu Köln (**2013**)

[Cha70] CHARPAK, G., D. RAHM, and H. STEINER; *Some developments in the operation of multiwire proportional chambers*; Nuclear Instruments and Methods (**1970**); 80(1), 13 – 34; ISSN 0029-554X; doi:10.1016/0029-554X(70)90293-4

[Col73] COLSON, W. B., J. MCPHERSON, and F. T. KING; *High-gain imaging electron multiplier*; Review of Scientific Instruments (**1973**); 44(12), 1694–1696; doi:10.1063/1.1686034

[Die12] DIEL, F.; *Aufbau einer digitalen Sweepersteuerung für das Null-Grad-Strahlrohr* (**2012**); bachelortesis, University of Cologne

[Dro06] DROBYCHEV, G., A. BARYSEVICH, K. DELENDIK, ET AL.; *Development of micro-channel plates on a basis of aluminum oxide*; Nuclear Instruments and Methods in Physics Research Section A: Accelerators, Spectrometers, Detectors and Associated Equipment (**2006**); 567(1), 290 – 293; ISSN 0168-9002; doi:10.1016/j.nima.2006.05.097; proceedings of the 4th International Conference on New Developments in Photodetection BEAUNE 2005, Fourth International Conference on New Developments in Photodetection

[Edg89] EDGAR, M. L., R. KESSEL, J. S. LAPINGTON, and D. M. WALTON; *Spatial charge cloud distribution of microchannel plates*; Review of Scientific Instruments (**1989**); 60(12), 3673–3680; doi:10.1063/1.1140473

[Eva65] EVANS, D. S.; *Low Energy Charged-Particle Detection Using the Continuous-Channel Electron Multiplier*; Review of Scientific Instruments (**1965**); 36(3), 375–382; doi:10.1063/1.1719576

[FAI12] FAIR; *HISPEC (HIgh-Resolution In-flight SPECtroscopy)/DESPEC (DEcay SPECtroscopy)*; Website (**2012**) http://www.fair-center.eu/en/for-users/experiments/nustar/experiments/hispecdespec.html

[Fio93] FIONI, G., H. FAUST, M. GROSS, ET AL.; *Reduction of energy dispersion on a parabola mass spectrometer*; Nuclear Instruments and Methods in Physics Research A (**1993**); 332, 175–180

[Fri96] FRIEDMAN, P. G., R. A. CUZA, J. R. FLEISCHMAN, ET AL.; *Multilayer anode with crossed serpentine delay lines for high spatial resolution readout of microchannel plate detectors*; Review of Scientific Instruments (**1996**); 67(2), 596–608; doi:10.1063/1.1146623

[Gab75] GABOR, G., W. SCHIMMERLING, D. GREINER, F. BIESER, and P. LINDSTROM; *High resolution spectrometry for relativistic heavy ions*; Nuclear Instruments and Methods (**1975**); 130(1), 65 – 71; ISSN 0029-554X; doi:10.1016/0029-554X(75)90158-5

[Gal03] GALÈS, S.; *Towards the next generation of radioactive ion beam facilities*; Nuclear Physics A (**2003**); 722(0), C148 – C156; ISSN 0375-9474; doi:10.1016/S0375-9474(03)01351-4

[Gal10] GALÈS, S.; *SPIRAL2 at GANIL: Next Generation of ISOL Facility for Intense Secondary Radioactive Ion Beams*; Nuclear Physics A (**2010**); 834(1–4), 717c – 723c; ISSN 0375-9474; doi:10.1016/j.nuclphysa.2010.01.130; the 10th International Conference on Nucleus-Nucleus Collisions (NN2009)

[Gei92] GEISSEL, H., P. ARMBRUSTER, K. BEHR, ET AL.; *The GSI projectile fragment separator (FRS): a versatile magnetic system for relativistic heavy ions*; Nuclear Instruments and Methods in Physics Research Section B: Beam Interactions with Materials and Atoms (**1992**); 70(1–4), 286 – 297; ISSN 0168-583X; doi:10.1016/0168-583X(92)95944-M

[Gei95] GEISSEL, H., G. MÜNZENBERG, and K. RIISAGER; *Secondary Exotic Nuclear Beams*; Annual Review of Nuclear and Particle Science (**1995**); 45, 163–203; doi:10.1146/annurev.ns.45.120195.001115

[Gei03] GEISSEL, H., H. WEICK, M. WINKLER, ET AL.; *The Super-FRS project at GSI*; Nuclear Instruments and Methods in Physics Research Section B: Beam Interactions with Materials and Atoms (**2003**); 204(0), 71 – 85; ISSN 0168-583X; doi:10.1016/S0168-583X(02)01893-1; 14th International Conference on Electromagnetic Isotope Separators and Techniques Related to their Applications

[Gla01] GLASMACHER, T.; *Intermediate-energy Coulomb excitation*; Nuclear Physics A (**2001**); 693(1–2), 90 – 104; ISSN 0375-9474; doi:10.1016/S0375-9474(01)01147-2; radioactive Nuclear Beams

[Goo13] GOODFELLOW; *Goodfellow GmbH Material Catalogue*; Website (**2013**) http://www.goodfellow.com

[Gou75] GOULDING, F. S. and B. G. HARVEY; *Identification of Nuclear Particles*; Annual Review of Nuclear Science (**1975**); 25(1), 167–240; doi:10.1146/annurev.ns.25.120175.001123

[Gre11] GREGOR, E.; *Double-sided silicon strip detectors for position, energy loss and especially time-of-flight measurements in slowed-down beam experiments*; Master's thesis; TU Darmstadt (**2011**)

[Hab98] HABS, D., O. KESTER, T. SIEBER, ET AL.; *The REX-ISOLDE project*; Nuclear Instruments and Methods in Physics Research Section B: Beam Interactions with Materials and Atoms (**1998**); 139(1–4), 128 – 135; ISSN 0168-583X; doi:10.1016/S0168-583X(97)00978-6

[Hai03] HAISCH, C. and H. BECKER-ROSS; *An electron bombardment CCD-camera as detection system for an echelle spectrometer*; Spectrochimica Acta Part B: Atomic Spectroscopy (**2003**); 58(7), 1351 – 1357; ISSN 0584-8547; doi:10.1016/S0584-8547(03)00071-5

[Ham09] HAMAMATSU; *MCP & MCP Assembly - Selection Guide* (**2009**)

[Hig75] HIGHLAND, V. L.; *Some practical remarks on multiple scattering*; Nuclear Instruments and Methods (**1975**); 129(2), 497 – 499; ISSN 0029-554X; doi:10.1016/0029-554X(75)90743-0

[Hoe01] HOENDERKEN, T. H., C. W. HAGEN, J. E. BARTH, P. KRUIT, and G. O. NÜTZEL; *Influence of the microchannel plate and anode gap parameters on the spatial resolution of an image intensifier*; Journal of Vacuum Science & Technology B: Microelectronics and Nanometer Structures (**2001**); 19(3), 843–850; doi:10.1116/1.1364701

[Jag] JAGUTZKI, O.; private communication

[Jag02a] JAGUTZKI, O., A. CEREZO, A. CZASCH, ET AL.; *Multiple hit readout of a microchannel plate detector with a three-layer delay-line anode*; Nuclear Science, IEEE Transactions on (**2002**); 49(5), 2477–2483; ISSN 0018-9499; doi:10.1109/TNS.2002.803889

[Jag02b] JAGUTZKI, O., J. LAPINGTON, L. WORTH, ET AL.; *Position sensitive anodes for {MCP} read-out using induced charge measurement*; Nuclear Instruments and Methods in Physics Research Section A: Accelerators, Spectrometers, Detectors and Associated Equipment (**2002**); 477(1–3), 256 – 261; ISSN 0168-9002; doi:10.1016/S0168-9002(01)01843-5; 5th Int. Conf. on Position-Sensitive Detectors

[Jon93] JONSON, B., H. L. RAVN, and G. WALTER; *Isolde ps booster facility at cern: Experiments with slow radioactive beams*; Nuclear Physics News (**1993**); 3(2), 5–16; doi:10.1080/10506899308210201

[Kav85] KAVALOV, R., Y. MARGARYAN, M. PANYAN, and G. PAPYAN; *A zero-time detector of charged particles based on secondary electron emission from low density dielectrics*; Nuclear Instruments and Methods in Physics Research Section A: Accelerators, Spectrometers, Detectors and Associated Equipment (**1985**); 237(3), 543 – 546; ISSN 0168-9002; doi:10.1016/0168-9002(85)91064-2

[Kel87] KELLER, H., G. KLINGELHÖFER, and E. KANKELEIT; *A position sensitive microchannelplate detector using a delay line readout anode*; Nuclear Instruments and Methods in Physics Research Section A: Accelerators, Spectrometers, Detectors and Associated Equipment (**1987**); 258(2), 221 – 224; ISSN 0168-9002; doi:10.1016/0168-9002(87)90059-3

[Kos89] KOSCHAR, P., K. KRONEBERGER, A. CLOUVAS, ET AL.; *Secondary-electron yield as a probe of preequilibrium stopping power of heavy ions colliding with solids*; Phys. Rev. A (**1989**); 40, 3632–3636; doi:10.1103/PhysRevA.40.3632

[Kos08a] KOSCIELNIAK, S., F. AMES, R. BAARTMAN, ET AL.; *ARIEL and the TRIUMF E-Linac Initiative, a 0.5 MW Electron Linac for Rare Isotope Beam Production*; Proceedings of the XXIV Linear Accelerator Conference (LINAC08) (**2008**); pp. 383–385
http://epaper.kek.jp/LINAC08/papers/tup002.pdf

[Kos08b] KOSEV, K., N. NANKOV, M. FRIEDRICH, ET AL.; *A high-resolution time-of-flight spectrometer with tracking capabilities for fission fragments and beams of exotic nuclei*; Nuclear Instruments and Methods in Physics Research Section A: Accelerators, Spectrometers, Detectors and Associated Equipment (**2008**); 594(2), 178 – 183; ISSN 0168-9002; doi:10.1016/j.nima.2008.06.014

[Koz08] KOZULIN, E., A. BOGACHEV, M. ITKIS, ET AL.; *The CORSET time-of-flight spectrometer for measuring binary products of nuclear reactions*; Instruments and Experimental Techniques (**2008**); 51(1), 44–58; ISSN 0020-4412; doi:10.1134/S0020441208010041

[Kro88] KRONEBERGER, K., A. CLOUVAS, G. SCHLÜSSLER, ET AL.; *Secondary electron yields from the entrance and exit surfaces of thin carbon foils induced by penetration of H^+, H^0 and H^{+2} projectiles (1.2 MeV/u)*; Nuclear Instruments and Methods in Physics Research Section B: Beam Interactions with Materials and Atoms (**1988**); 29(4), 621 – 626; ISSN 0168-583X; doi:10.1016/0168-583X(88)90469-7

[Lam87] LAMPTON, M., O. SIEGMUND, and R. RAFFANTI; *Delay line anodes for microchannel-plate spectrometers*; Review of Scientific Instruments (**1987**); 58(12), 2298–2305; doi:10.1063/1.1139341

[Lax03] LAXDAL, R., G. CLARK, G. DUTTO, ET AL.; *The ISAC-II Upgrade at TRIUMF - Progress and Developments*; Proceedings of the 2003 Particle Accelerator Conference (**2003**); pp. 601–603 http://accelconf.web.cern.ch/accelconf/p03/PAPERS/ROPA010.PDF

[LC13] LAPPD-COLLABORATION; *Lare-Area Picosecond Photo-Detectors Project*; Website (**2013**) http://psec.uchicago.edu/

[Lin96] LINDHARD, J. and A. SÖRENSEN; *Relativistic theory of stopping for heavy ions*; Physical Review A (**1996**); 53, 2443–2456; doi:10.1103/PhysRevA.53.2443

[Lin04] LINDROOS, M.; *Review of ISOL-type Radioactive Beam Facilities*; Proceedings of the 9th European Particle Accelerator Conference (EPAC'04) (**2004**); pp. 45–49

[Lin08] LINDROOS, M., P. BUTLER, M. HUYSE, and K. RIISAGER; *HIE-ISOLDE*; Nuclear Instruments and Methods in Physics Research Section B: Beam Interactions with Materials and Atoms (**2008**); 266(19–20), 4687 – 4691; ISSN 0168-583X; doi:10.1016/j.nimb.2008.05.136; proceedings of the XVth International Conference on Electromagnetic Isotope Separators and Techniques Related to their Applications

[Lyn91] LYNCH, G. R. and O. I. DAHL; *Approximations to multiple Coulomb scattering*; Nuclear Instruments and Methods in Physics Research Section B: Beam Interactions with Materials and Atoms (**1991**); 58(1), 6 – 10; ISSN 0168-583X; doi:10.1016/0168-583X(91)95671-Y

[Mar78] MARX, J. N. and D. R. NYGREN; *The Time Projection Chamber*; Physics Today (**1978**); 31(10), 46–53; doi:10.1063/1.2994775

[Mar81] MARTIN, C., P. JELINSKY, M. LAMPTON, R. F. MALINA, and H. O. ANGER; *Wedge-and-strip anodes for centroid-finding position-sensitive photon and particle detectors*; Review of Scientific Instruments (**1981**); 52(7), 1067–1074; doi:10.1063/1.1136710

[Mat85] MATSUURA, S., S. UMEBAYASHI, C. OKUYAMA, and K. OBA; *Characteristics of the Newly Developed MCP and Its Assembly*; Nuclear Science, IEEE Transactions on (**1985**); 32(1), 350–354; ISSN 0018-9499; doi:10.1109/TNS.1985.4336854

[Mon05] MONTAGNOLI, G., A. STEFANINI, M. TROTTA, ET AL.; *The large-area micro-channel plate entrance detector of the heavy-ion magnetic spectrometer PRISMA*; Nuclear Instruments and Methods in Physics Research Section A: Accelerators, Spectrometers, Detectors and Associated Equipment (**2005**); 547, 455 – 463; ISSN 0168-9002; doi:10.1016/j.nima.2005.03.158

[Mri08] MRIGAKSHI, A.; *Study and Test of Micro-Channel Plates used in the Dual Ion Spectrometer of the MMS mission by NASA*; Master's thesis; Lulea University of Technology (**2008**)

[Mü92] MÜNZENBERG, G.; *The separation techniques for secondary beams*; Nuclear Instruments and Methods in Physics Research Section B: Beam Interactions with Materials and Atoms (**1992**); 70, 265–275

[Nan05] NANKOV, N., K. KOSEV, A. WAGNER, ET AL.; *Calculations for the Optimization of the Time and Space Resolution of an Electrostatic Mirror*; p. 25; Wissenschaftlich-Technische Berichte, Annual Report 2004; Forschungszentrum Rossendorf (**2005**)
http://www.hzdr.de/publications/007448/7448.pdf

[Naq11a] NAQVI, F.; *Probing the collectivity in neutron-rich Cd isotopes via γ-ray spectroscopy*; Ph.D. thesis; University of Cologne (**2011**)

[Naq11b] NAQVI, F., P. BOUTACHKOV, M. GÓRSKA, ET AL.; *Development of Slowed Down Beams at the Fragment Separator for FAIR*; Acta Physica Polonica B (**2011**); 42, 725–728
http://www.actaphys.uj.edu.pl/vol42/pdf/v42p0725.pdf

[Odl96] ODLAND, O., W. MITTIG, A. LÉPINE-SZILY, ET AL.; *A fast position sensitive microchannel plate detector for ray-tracing of charged particles*; Nuclear Instruments and Methods in Physics Research Section A: Accelerators, Spectrometers, Detectors and Associated Equipment (**1996**); 378, 149 – 154; ISSN 0168-9002; doi:10.1016/0168-9002(96)00441-X

[Ort13] ORTEC; *Ortec Modular Electronic Instruments*; Website (**2013**)
http://www.ortec-online.com/Solutions/modular-electronic-instruments.aspx

[Oxf] OXFORDINSTRUMENTS; *Tennelec Time To Amplitude Converter Model TC 862 Manual*

[Pas] PASCOVICI, G.; private communication

[Pas11] PASCOVICI, G.; *A new Time of Flight (TOF) and Beam Profile Monitor (BPM) - "Cerberus" product brochure and user's manual*; Institute of Nuclear Physics; Zülpicher Str. 77, 50937 Köln, Germany (**2011**)

[Pas13] PASCOVICI, G., A. DEWALD, S. HEINZE, ET AL.; *A new beam profile monitor and time of flight system for CologneAMS*; Nuclear Instruments and Methods in Physics Research Section B: Beam Interactions with Materials and Atoms (**2013**); 294(0), 410 – 415; ISSN 0168-583X; doi:10.1016/j.nimb.2012.04.026; proceedings of the Twelfth International Conference on Accelerator Mass Spectrometry, Wellington, New Zealand, 20-25 March 2011

[Pho09] PHOTONIS; *Chevron MCP and Detector Initial Start-up and Electrical Test Procedure* (**2009**)

[Pho13] PHOTEK; *Photek Technical Information*; Website (**2013**) http://www.photek.com/technical-info.html

[Pod06] PODOLYÁK, Z.; *The High-Resolution In-Flight Spectroscopy (HISPEC) project at FAIR*; International Journal of Modern Physics E (**2006**); 15(08), 1967–1977; doi:10.1142/S0218301306005411

[Pod08] PODOLYÁK, Z.; *From RISING to HISPEC/DESPEC*; Nuclear Instruments and Methods in Physics Research Section B: Beam Interactions with Materials and Atoms (**2008**); 266(19–20), 4589 – 4594; ISSN 0168-583X; doi:10.1016/j.nimb.2008.05.106; proceedings of the XVth International Conference on Electromagnetic Isotope Separators and Techniques Related to their Applications

[Pra93] PRAČEK, B. and M. KERN; *AES studies of active intrachannel surface in microchannel plates*; Applied Surface Science (**1993**); 70–71, Part 1(0), 169 – 171; ISSN 0169-4332; doi:10.1016/0169-4332(93)90420-G

[Pri01] PRICE, G. and G. FRASER; *Calculation of the output charge cloud from a microchannel plate*; Nuclear Instruments and Methods in Physics Research Section A: Accelerators, Spectrometers, Detectors and Associated Equipment (**2001**); 474(2), 188 – 196; ISSN 0168-9002; doi:10.1016/S0168-9002(01)00880-4

[Rub06] RUBIO, B.; *Decay Spectroscopy (DESPEC) at the new FAIR-NUSTAR facility*; International Journal of Modern Physics E (**2006**); 15(08), 1979–1988; doi:10.1142/S0218301306005484

[Rug72] RUGGIERI, D. J.; *Microchannel Plate Imaging Detectors*; Nuclear Science, IEEE Transactions on (**1972**); 19(3), 74–84; ISSN 0018-9499; doi:10.1109/TNS.1972.4326705

[Ré11] RÉGIS, J.-M.; *Fast Timing with $LaBr_3$(Ce) Scintillators and the Mirror Symmetric Centroid Difference Method*; Ph.D. thesis; University of Cologne (**2011**)

[Sak08] SAKURAI, H.; *RI Beam Factory Project at RIKEN*; Nuclear Physics A (**2008**); 805(1–4), 526c – 532c; ISSN 0375-9474; doi:10.1016/j.nuclphysa.2008.02.291; iNPC 2007 Proceedings of the 23rd International Nuclear Physics Conference

[Šar96] ŠARO, Š., R. JANIK, S. HOFMANN, ET AL.; *Large size foil-microchannel plate timing detectors*; Nuclear Instruments and Methods in Physics

Research Section A: Accelerators, Spectrometers, Detectors and Associated Equipment (**1996**); 381(2–3), 520 – 526; ISSN 0168-9002; doi:10.1016/S0168-9002(96)00651-1

[Sch66] SCHMIDT, K. C. and C. F. HENDEE; *Continuous Channel Electron Multiplier Operated in the Pulse Saturated Mode*; Nuclear Science, IEEE Transactions on (**1966**); 13(3), 100–111; ISSN 0018-9499; doi:10.1109/TNS.1966.4324085

[Sch98] SCHEIDENBERGER, C. and H. GEISSEL; *Penetration of relativistic heavy ions through matter*; Nuclear Instruments and Methods in Physics Research Section B: Beam Interactions with Materials and Atoms (**1998**); 135(1–4), 25 – 34; ISSN 0168-583X; doi:10.1016/S0168-583X(97)00639-3

[Sel92] SELLIN, P., P. WOODS, D. BRANFORD, ET AL.; *A double-sided silicon strip detector system for proton radioactivity studies*; Nuclear Instruments and Methods in Physics Research Section A: Accelerators, Spectrometers, Detectors and Associated Equipment (**1992**); 311(1–2), 217 – 223; ISSN 0168-9002; doi:10.1016/0168-9002(92)90867-4

[Ser12] SERVICE, S. I.; *SIMION*; Website (**2012**) http://www.fair-center.eu/en/for-users/experiments/nustar/experiments/hispecdespec.html

[Sie91] SIEGMUND, O., M. LAMPTON, R. RAFFANTI, and W. HERRICK; *High resolution delay line readouts for microchannel plates*; Nuclear Instruments and Methods in Physics Research Section A: Accelerators, Spectrometers, Detectors and Associated Equipment (**1991**); 310(1–2), 311 – 316; ISSN 0168-9002; doi:10.1016/0168-9002(91)91049-2

[Sie03] SIEGMUND, O., A. TREMSIN, J. VALLERGA, R. ABIAD, and J. HULL; *High resolution cross strip anodes for photon counting detectors*; Nuclear Instruments and Methods in Physics Research Section A: Accelerators, Spectrometers, Detectors and Associated Equipment (**2003**); 504(1–3), 177 – 181; ISSN 0168-9002; doi:10.1016/S0168-9002(03)00816-7; proceedings of the 3rd International Conference on New Developments in Photodetection

[Sob88] SOBOTTKA, S. and M. WILLIAMS; *Delay line readout of microchannel plates*; Nuclear Science, IEEE Transactions on (**1988**); 35(1), 348–351; ISSN 0018-9499; doi:10.1109/23.12740

[Sta82] STARZECKI, W., A. STEFANINI, S. LUNARDI, and C. SIGNORINI; *A compact time-zero detector for mass identification of heavy ions*; Nuclear Instruments and Methods in Physics Research (**1982**); 193(3), 499 – 505; ISSN 0167-5087; doi:10.1016/0029-554X(82)90242-7

[Ste57] STERNGLASS, E. J.; *Theory of Secondary Electron Emission by High-Speed Ions*; Phys. Rev. (**1957**); 108, 1–12; doi:10.1103/PhysRev.108.1

[Sur13] SURFACECONCEPT; *Surface Concept Fast Electronics Portfolio*; Website (**2013**)
http://www.surface-concept.com/products_electronics.html

[Tar08] TARASOV, O. and D. BAZIN; *LISE++: Radioactive beam production with in-flight separators*; Nuclear Instruments and Methods in Physics Research Section B: Beam Interactions with Materials and Atoms (**2008**); 266(19–20), 4657 – 4664; ISSN 0168-583X; doi:10.1016/j.nimb.2008.05.110; proceedings of the XVth International Conference on Electromagnetic Isotope Separators and Techniques Related to their Applications

[Tay09] TAYLOR, M., M. BENTLEY, D. RUDOLPH, ET AL.; *A new simulation package to model detector systems with fragmentation reactions and ion separators: Application to the LYCCA-0 system*; Nuclear Instruments and Methods in Physics Research Section A: Accelerators, Spectrometers, Detectors and Associated Equipment (**2009**); 606(3), 589 – 597; ISSN 0168-9002; doi:10.1016/j.nima.2009.05.003

[Tre96] TREMSIN, A., J. PEARSON, G. FRASER, W. FELLER, and P. WHITE; *Microchannel plate operation at high count rates: new results*; Nuclear Instruments and Methods in Physics Research Section A: Accelerators, Spectrometers, Detectors and Associated Equipment (**1996**); 379(1), 139 – 151; ISSN 0168-9002; doi:10.1016/0168-9002(96)00482-2

[Val00] VALLERGA, J. and O. SIEGMUND; *2K×2K resolution element photon counting {MCP} sensor with >200 kHz event rate capability*; Nuclear Instruments and Methods in Physics Research Section A: Accelerators, Spectrometers, Detectors and Associated Equipment (**2000**); 442(1–3), 159 – 163; ISSN 0168-9002; doi:10.1016/S0168-9002(99)01215-2

[Vil03] VILLARI, A. C.; *First results at SPIRAL-GANIL*; Nuclear Instruments and Methods in Physics Research Section B: Beam Interactions with Materials and Atoms (**2003**); 204(0), 31 – 41; ISSN 0168-583X; doi:10.1016/S0168-583X(02)01887-6; 14th International Conference on Electromagnetic Isotope Separators and Techniques Related to their Applications

[War] WARR, N.; private communication

[Was71] WASHINGTON, D., V. DUCHENOIS, R. POLAERT, and R. BEASLEY; Acta Electronica (**1971**); 14, 201

[Wei79] WEISSENBERGER, E., W. KAST, and F. GÖNNENWEIN; *Compact time-zero detector for heavy ions*; Nuclear Instruments and Methods (**1979**); 163(2–3), 359 – 362; ISSN 0029-554X; doi:10.1016/0029-554X(79)90119-8

[Wil89] WILLIAMS, M. and S. SOBOTTKA; *High resolution two dimensional readout of microchannel plates with large area delay lines*; Nuclear Science,

IEEE Transactions on (**1989**); 36(1), 227–230; ISSN 0018-9499; doi:10.1109/23.34440

[Wil91] WILLIAMS, M. B., S. E. SOBOTTKA, and J. A. SHEPHERD; *Delay line readout of microchannel plates in a prototype position-sensitive photomultiplier tube*; Nuclear Instruments and Methods in Physics Research Section A: Accelerators, Spectrometers, Detectors and Associated Equipment (**1991**); 302(1), 105 – 112; ISSN 0168-9002; doi:10.1016/0168-9002(91)90498-F

[Win08] WINKLER, M., H. GEISSEL, H. WEICK, ET AL.; *The status of the Super-FRS in-flight facility at FAIR*; Nuclear Instruments and Methods in Physics Research Section B: Beam Interactions with Materials and Atoms (**2008**); 266(19–20), 4183 – 4187; ISSN 0168-583X; doi:10.1016/j.nimb.2008.05.073; proceedings of the XVth International Conference on Electromagnetic Isotope Separators and Techniques Related to their Applications

[Wiz79] WIZA, J. L.; *Microchannel plate detectors*; Nuclear Instruments and Methods (**1979**); 162(1–3), 587 – 601; ISSN 0029-554X; doi:10.1016/0029-554X(79)90734-1

[Wu08] WU, M., C. A. KRUSCHWITZ, D. V. MORGAN, and J. MORGAN; *Monte Carlo simulations of microchannel plate detectors. I. Steady-state voltage bias results*; Review of Scientific Instruments (**2008**); 79(7), 073104; doi:10.1063/1.2949119

[XiA13] XIA; *DGF-4C - Digital Gamma Finder*; Website (**2013**) http://www.xia.com/DGF-4C.html

Acknowledgment - Danksagung

Ohne die Mithilfe vieler Menschen wäre die vorliegende Arbeit nicht möglich gewesen. Ihnen allen gilt mein tiefer Dank, wobei ich einige Menschen hier besonders erwähnen möchte.

Danke an

- ⋆ **Prof. Jan Jolie** für die Betreuung meiner Arbeit und die Möglichkeit, mich schon früh und über all die Jahre hinweg im IKP einzubringen sowie die Möglichkeit, an diesem Projekt teilzuhaben;
- ⋆ **Prof. Peter Reiter** für die Bereitschaft, sich als Zweitprüfer zur Verfügung zu stellen und diese Arbeit zu bewerten;
- ⋆ **Prof. Schadschneider** für den Prüfungsvorsitz meiner Verteidigung;
- ⋆ **Gheorghe Pascovici** für seine Geduld, zahlreiche Erklärungen, viele Diskussionen, Hilfe und Ratschläge wann immer es um elektronische Details ging;
- ⋆ **Nigel Warr** für die Beantwortung sämtlicher Fragen rund um die Datenaufnahme und zahlreiche Diskussionen;
- ⋆ **Mario Cappellazzo** für all die fruchtbaren Diskussionen, immer zuverlässige Arbeit und mir in der Schreibphase dieser Arbeit den Rücken freigehalten zu haben;
- ⋆ **Stefan Thiel, Dirk Diefenbach und der gesamten Feinmechanikwerkstatt** für die stets hervorragend konstruierten und präzise gefertigten Teile, auch wenn es mal wieder schnell gehen musste;
- ⋆ **Christoph Görgen, Gheorghe Pascovici und der gesamten Elektronikwerkstatt** für die Konstruktion und Fertigung zuverlässiger Elektronik;
- ⋆ **Claus Müller-Gatermann** für viele Diskussionen und die kompetente Unterstützung wann immer es um den Beschleuniger und den neuen Messplatz ging;
- ⋆ **die Operateure** für einen zuverlässig arbeitenden Beschleuniger;
- ⋆ **Ralf Schulze** für „hitzige Gefechte“ nach der Mittagspause, seine Unterstützung, das ein oder andere Kölsch und vieles mehr;
- ⋆ **Mario Cappellazzo, Kevin Moschner, Claus Müller-Gatermann und Caro Vossaert** für das Korrekturlesen der Arbeit;

- ⋆ **Ralf Schulze, Benedikt Birkenbach, Nima Saed-Samii, Moritz Dannhoff, Gunnar Frießner und Norbert Braun** für die schöne Zeit und Zusammenarbeit in der SysOp Gruppe;
- ⋆ **Plamen Boutachkov und Nora Gregor** für die Unterstützung bei den Messungen an der GSI ;
- ⋆ **Erika Kroppen-Matenaer** für die zuverlässige Hilfe und Zusammenarbeit wann immer es um Beschaffungen ging;
- ⋆ **allen Mitgliedern des IKP** für die tolle Arbeitsatmosphäre, eine schöne und prägende Zeit.
- ⋆ Mein ganz besonderer Dank gilt **meinen Eltern** für deren bedingunglose Unterstützung während meines gesamten Studiums und all meinen Unternehmungen.
- ⋆ Meiner größter Dank gilt meiner Frau **Caro Vossaert** für Ihre Unterstützung, Liebe und dass Sie immer für mich da ist.

Ich versichere, dass ich die von mir vorgelegte Dissertation selbstständig angefertigt, die benutzten Quellen und Hilfsmittel vollständig angegeben und die Stellen der Arbeit — einschließlich Tabellen, Karten und Abbildungen —, die anderen Werken im Wortlaut oder dem Sinn nach entnommen sind, in jedem Einzelfall als Entlehnung kenntlich gemacht habe; dass diese Dissertation noch keiner anderen Fakultät oder Universität zur Prüfung vorgelegen hat; dass sie — abgesehen von unten angegebenen Teilpublikation — noch nicht veröffentlicht worden ist sowie, dass ich eine solche Veröffentlichung vor Abschluss des Promotionsverfahrens nicht vornehmen werde.

Die Bestimmungen der Promotionsordnung sind mir bekannt. Die von mir vorgelegte Dissertation ist von Prof. Dr. J. Jolie betreut worden.

Köln, 22. August 2013

Michael Pfeiffer

Teilpublikationen

PFEIFFER, M., G. PASCOVICI, N. WARR, F. NAQVI and J. JOLIE; *Beam Profile Monitor, ToF and Tracking Detector Set-up for HISPEC/DESPEC*; GSI Scientific Report 2009 (**2010**); 30

PFEIFFER, M., G. PASCOVICI, S. THIEL, N. WARR and J. JOLIE; *Tagging of alpha particles with a large scale, high timing resolution beam profile monitor*; GSI Scientific Report 2010 (**2011**); 136

PFEIFFER, M., G. PASCOVICI, M. CAPPELLAZZO, S. THIEL, N. WARR and J. JOLIE; *Investigation of the spatial resolution of a large scale, emissive foil detector*; GSI Scientific Report 2011 (**2012**); 136

PFEIFFER, M., M. CAPPELLAZZO, E. GREGOR, P. BOUTACHKOV, G. PASCOVICI, S. THIEL, N. WARR and J. JOLIE; *A new Detector Testbed for future FAIR based Slowed Down Beam Setups at the Cologne FN-Tandem Accelerator Facility*; GSI Scientific Report 2012 (**2013**); 208

PASCOVICI, G., A. DEWALD, S. HEINZE, L. FINK, C. MÜLLER-GATERMANN, M. SCHIFFER, C. FEUERSTEIN, M. PFEIFFER, J. JOLIE, S. THIEL, K.O. ZELL, O. ARNOPOLINA and F. VON BLANCKENBURG; *A new beam profile monitor and time of*

flight system for CologneAMS; Nuclear Instruments and Methods in Physics Research Section B: Beam Interactions with Materials and Atoms (**2013**); 294(0), 410 – 415